

FRONT COVER AND SPINE

ERKARTAL

Mustafa

MODELLING AND INVESTIGATIONS OF AMORPHOUS

MATERIALS

AGU

2019

MODELLING AND INVESTIGATIONS OF AMORPHOUS MATERIALS

A THESIS

SUBMITTED TO THE DEPARTMENT OF MATERIALS SCIENCE
AND MECHANICAL ENGINEERING
AND THE GRADUATE SCHOOL OF ENGINEERING AND SCIENCE
OF ABDULLAH GUL UNIVERSITY
IN PARTIAL FULFILLMENT OF THE REQUIREMENTS
FOR THE DEGREE OF
DOCTOR OF PHILOSOPHY

By

Mustafa ERKARTAL

December, 2019

MODELLING AND INVESTIGATIONS OF AMORPHOUS MATERIALS

A THESIS

SUBMITTED TO THE DEPARTMENT OF MATERIALS SCIENCE AND
MECHANICAL ENGINEERING
AND THE GRADUATE SCHOOL OF ENGINEERING AND SCIENCE OF
ABDULLAH GUL UNIVERSITY

IN PARTIAL FULFILLMENT OF THE REQUIREMENTS
FOR THE DEGREE OF
DOCTOR OF PHILOSOPHY

By

Mustafa ERKARTAL

December, 2019

SCIENTIFIC ETHICS COMPLIANCE

I hereby declare that all information in this document has been obtained in accordance with academic rules and ethical conduct. I also declare that, as required by these rules and conduct, I have fully cited and referenced all materials and results that are not original to this work.

Name-Surname:Mustafa ERKARTAL

Signature :

XXXXXXXXXX

REGULATORY COMPLIANCE

Ph.D. thesis titled Modelling and Investigations of Amorphous Materials has been prepared in accordance with the Thesis Writing Guidelines of the Abdullah Gül University, Graduate School of Engineering & Science.

Prepared By

Mustafa ERKARTAL

Signature

Advisor

Prof. Murat DURANDURDU

Signature

Head of the Materials Science and Mechanical Engineering Program

Prof. Murat DURANDURDU

Signature

ACCEPTANCE AND APPROVAL

Ph.D. thesis titled Modelling and Investigations of Amorphous Materials and prepared by Mustafa ERKARTAL has been accepted by the jury in the Materials Science and Mechanical Engineering Graduate Program at Abdullah Gül University, Graduate School of Engineering & Science.

13/12 / 2019

(Thesis Defense Exam Date)

JURY:

Advisor :Prof. Murat DURANDURDU

Member :Prof. Oğuz GÜLSEREN

Member : Assoc. Prof. M. Serdar ÖNSES

Member : Assoc. Prof. Evren MUTLUGÜN

Member : Asst. Prof. Fahri Alkan

APPROVAL:

The acceptance of this Ph.D. thesis has been approved by the decision of the Abdullah Gül University, Graduate School of Engineering & Science, Executive Board dated /..... / and numbered

..... /..... /

(Date)

Graduate School Dean
Prof. İrfan ALAN

ABSTRACT

MODELLING AND INVESTIGATIONS OF AMORPHOUS MATERIALS

Mustafa Erkartal
Ph.D. in Materials Science and Mechanical Engineering
Supervisor: Prof. Murat Durandurdu

December, 2019

The aim of this PhD dissertation is to investigate the behavior of different MOFs under hydrostatic and uniaxial stresses by using ab-initio molecular dynamics simulations (AIMD). The results obtained from computations are reported in three main chapters. In the first part, ab initio simulations within a generalized gradient approximation (GGA) were carried out to investigate the response of MOF-5 to high pressure. Similar to the previous experimental findings, a pressure-induced amorphization (PIA) was observed at 2 GPa through the simulations. The phase transformation was an irreversible first order transition and accompanied by a volume collapse around 68%. Remarkably, the transition arose from local distortions and contrary to previous suggestions, did not involve any bond breaking or formation. Additionally, a drastic band gap closure was perceived for the amorphous state. For the second part of this project, AIMD simulations were performed to probe the high-pressure behavior of ZIF-8 over wide pressure-range. Under compression, the enormous distortions in the ZnN_4 tetrahedral units led to a crystal-to-amorphous phase transition at around 3 GPa. During the amorphization process, the Zn-N coordination was retained. No other phase change but a possible fracture of the system was proposed above 10 GPa. When the applied pressure was released just before the amorphization, the rotations of imidazolate linkers (swing effect) caused an isostructural crystal-to-crystal phase transition. In the tensile regime, no phase transition was perceived up to -2.75 GPa at which point the structural failure was observed. In the last part of this research project, the phase transitions of ZIF polymorphs (ZIF-1 to ZIF-3) under pressure were comprehensively simulated. ZIF-1 showed some consecutive crystal-crystal and crystal-amorphous phase transitions between -2 GPa (tension) and 10 GPa (compression). On the other hand, ZIF-2 and ZIF-

3 presented similar pressure-volume relation in both tension and compression regions. In compression region, a rapid crystal-amorphous at relatively lower compression regime and most likely an amorphous-amorphous transition were explored whereas the structural failure was observed at around -3 GPa for all ZIFs.

Keywords: Metal-Organic Frameworks (MOFs), Pressure-Induced Amorphization (PIA), Ab Initio Molecular Dynamics (AIMD), Amorphous



ÖZET

AMORF MALZEMELERİN MODELLENMESİ VE İNCELENMESİ

Mustafa Erkartal
Mazleme Bilimi ve Makine Mühendisliği Bölümü Doktora
Tez Yöneticisi: Prof. Dr. Murat Durandurdu
Aralık, 2019

Bu doktora tezinin amacı ab-initio moleküler dinamiği simülasyonları (AIMD) yoluyla, metal-organik çerçeve yapılarıdaki (MOF) basınca bağlı amorfizasyonu (PIA) ve ayrıca diğer faz geçişlerini araştırmaktır. Hesaplardan elde edilen sonuçlar üç ana bölümde rapor edilmiştir. Birinci bölümde, MOF-5'in yüksek basınç davranışını araştırmak için ab initio simülasyonları yapıldı. Önceki deneysel bulgulara benzer şekilde, simülasyonlar sırasında 2 GPa'da bir PIA gözlemlendi. Bu faz geçişi, tersinir olmayan bir birinci dereceden bir dönüşüm olup, geçişe yaklaşık % 68'lik bir hacim çöküşü gözlenmektedir. Dikkat çekici bir şekilde, geçiş yerel bozulmalardan kaynaklanmaktadır ve önceki önerilerin aksine, bu faz geçişi boyunca herhangi bir bağ kırılımı ve oluşumu gözlenmemektedir. Ayrıca, amorf durum çerçeve yapının elektronik bant aralığı kayda değer bir ölçüde daralmaktadır. Bu projenin ikinci kısmı için, ZIF-8'in geniş bir basınç aralığında yüksek basınç davranışını araştırmak için AIMD simülasyonları yapıldı. Sıkıştırma altında, ZnN₄ tetrahedral ünitelerindeki büyük deformasyonlar, 3GPa civarında kristal-amorf bir faz geçişine yol açar. Amorflaşma süreci boyunca, Zn-N koordinasyonu korunur. Çalışılan basınç aralığında başka bir faz değişikliği bulunmadı, ancak sistemin olası tahrip oluşu 10GPa'nın üzerinde bulundu. Uygulanan basınç, amorfizasyondan hemen önce kaldırıldığında, imidazolat ligandlarının dönüşleri (salınım hareketi), bir kristal-kristal faz geçişine neden olmaktadır. Gerilme rejiminde ise -2.75GPa'a kadar herhangi bir faz geçişi tespit edilmezken, bu basınç üzerinde yapı tahrip olmaktadır. Bu araştırma projesinin son bölümünde, ZIF polimorflarının (ZIF-1, ZIF-2 ve ZIF-3) basınç altında geçişleri kapsamlı bir şekilde simüle edildi. ZIF-1, -2 GPa (gerilme bölgesi) ve 10 GPa (sıkıştırma bölgesi) arasında ardışık bazı kristal-kristal ve kristal-amorf faz geçişleri gösterir. Öte yandan, ZIF-2 ve ZIF-3, nispeten düşük sıkıştırma rejiminde hızlı kristal- amorf ve büyük olasılıkla amorf-amorf geçişler gösterirken, bütün ZIF'ler gerilme bölgesinde -3 GPa civarında tahrip olmaktadır.

Anahtar kelimeler: Metal-Organik Çerçeve Yapılar (MOF), Basınç-İndüklü Amorfizasyon (PIA), Ab Initio Moleküler Dinamik (AIMD), Amorf Mazlemeler



Acknowledgements

During the years of my PhD I had the pleasure to work under the supervision of Prof. Murat Durandurdu. He always academically supported me, guiding me over the whole period of the doctorate but at the same time giving me the chance to make my own decisions about my work.

I would like to thank Dr. Thomas Bennett who was willing to welcome me for eight months in his team at the University of Cambridge, UK. It has been a pleasure to work with him and an important working experience.

Also I thank following people for contributing to my academic from past to today: Prof. Yalçın Elerman, Prof. İlker Dinçer, Prof. Barış Emre, Prof. Ünal Şen, Prof. Omar Farha, Prof. Özgür Yazaydın, Prof. Hakan Usta and Prof. Serdar Önses.

A particular thank goes to Hüseyin Çilsalar, Oğzuhan Ayyıldız and Ahmet F. Yazıcı for their intellectual friendship.

I have to thank the TÜBİTAK to provided financial support for my research in University of Cambridge, UK, as part of 2214-A International Research Fellowship Program for PhD Students with the grant number 1059B141700539. The calculations were partly run on The Scientific and Technological Research Council of Turkey (TÜBİTAK) ULAKBILIM, High Performance and Grid Computing Center (TRUBA) resources. This dissertation also was partially supported by Abdullah Gül University Scientific Research Projects (BAP) under contract number FBA-2017-86.

Last but not the least; I would like to thank my family: my parents Şaban and Cemile for supporting me during whole my life, and brother Murat and sister Merve for their endless supports and love.

Finally huge thanks go to starring: my wife (queen) Hatice and my daughter (princess) Umay Lina. Everything is easier with you.

Table of Contents

1. INTRODUCTION	1
2. SCIENTIFIC BACKGROUND.....	8
2.1 AMORPHOUS SOLIDS.....	8
2.1.1 <i>Quenching from Melt</i>	9
2.1.2 <i>Pressure-Induced Amorphization</i>	10
2.2 METAL-ORGANIC FRAMEWORKS (MOFs).....	13
2.2.1 <i>The Literature Survey: Pressure-Induced Amorphization in MOFs</i>	14
2.3 DENSITY FUNCTIONAL THEORY.....	19
2.3.1 <i>The mathematical foundations of DFT</i>	20
2.3.2 <i>Born-Oppenheimer Approximation</i>	21
2.3.3 <i>Electron Density</i>	22
2.3.4 <i>Hohenberg-Kohn Theorems</i>	23
2.3.5 <i>Kohn-Sham Equations</i>	24
2.3.6 <i>Approximations of the Exchange-Correlation Functionals</i>	25
2.3.6.1 <i>Local (Spin) Density Approximation</i>	27
2.3.6.2 <i>Generalized-Gradient Approximation</i>	28
2.4 MOLECULAR DYNAMICS.....	29
2.4.1 <i>Classical Molecular Dynamics</i>	29
2.4.1 <i>Ab-initio Molecular Dynamics</i>	30
2.4.1.1 <i>Car-Parrinello Method</i>	30
2.4.1.2 <i>Parrinello-Rahman Method</i>	31
2.5 SIMULATION CONDITIONS AND STRUCTURAL ANALYSIS.....	32
2.5.1 <i>SIESTA</i>	33
2.5.2 <i>Pseudopotentials</i>	33
2.5.3 <i>Basis Set</i>	34
2.5.4 <i>Periodic Boundary Conditions</i>	34
2.5.5 <i>Geometry Optimization</i>	35
2.5.6 <i>Equation of State</i>	35
2.5.7 <i>Pair Distribution Function</i>	37
2.5.8 <i>Bond Properties</i>	38
2.5.9 <i>Electronic Properties</i>	38
3. PRESSURE-INDUCED AMORPHIZATION OF MOF-5.....	40
3.1 INTRODUCTION.....	40
3.2 METHODOLOGY.....	41
3.3 RESULTS AND DISCUSSION.....	42
3.4 CONCLUSION.....	53
4. PRESSURE-INDUCED AMORPHIZATION, MECHANICAL AND ELECTRONIC PROPERTIES OF ZEOLITIC IMIDAZOLATE FRAMEWORK (ZIF-8)	54
4.1 INTRODUCTION.....	54
4.2 METHODOLOGY.....	56
4.3 RESULTS & DISCUSSION.....	57
4.4 CONCLUSION.....	70
5. PRESSURE INDUCED PHASE TRANSITIONS IN ZEOLITIC IMIDAZOLATE FRAMEWORKS (ZIFS) POLYMORPHS	71
5.1 INTRODUCTION.....	71
5.2 METHODOLOGY.....	72
5.3 RESULTS & DISCUSSION.....	73
5.4 CONCLUSION.....	90
6. CONCLUSIONS AND FUTURE PROSPECTS.....	92

6.1 CONCLUSIONS	92
6.2 CHALLENGES AND FUTURE OUTLOOK	93



List of Figures

Figure 1.1 The atomic arrangement in crystalline and amorphous materials.....	4
Figure 2.1 Effect of temperature on the enthalpy of a glass forming melt.....	10
Figure 2.2 Graphical illustration of pressure-induced amorphization (PIA) as metastable melting event.....	12
Figure 2.3 Widespread potential applications of metal-organic frameworks (MOFs).....	14
Figure 2.4 Number of articles containing the keyword “DFT” or “density functional theory (data obtained from ISI Web of Knowledge).....	20
Figure 2.5 Perdew’s the Jacob’s ladder analogy to classification of exchange-correlation functionals.....	27
Figure 2.6 Schematic description of periodic boundary conditions in 2D.....	35
Figure 2.7 Space discretization for the evaluation of the radial distribution function.....	38
Figure 3.1 Pressure dependence of conventional cell volume.....	44
Figure 3.2 (a) Total and (b) partial pair-distribution functions (PDFs) for the crystalline MOF-5 phase and its amorphized form at 2GPa.....	45
Figure 3.3 Structural evolution of extracted subunit from conventional cell.....	46
Figure 3.4 Extracted subunit from the conventional cell of MOF-5. Zinc, oxygen, carbon, and hydrogen are presented in grey, red, brown and white, respectively.	47
Figure 3.5 Bond angles distributions for the crystalline MOF-5 and α -MOF-5 phases.....	48
Figure 3.6 Calculated total density of states (TDOS) and partial density of states (PDOS) for MOF-5, the structure at 1GPa and α -MOF-5.....	49
Figure 3.7 (a) Bader atomic charges (b) Bader atomic volumes.....	51
Figure 4.1 The hydrostatic pressure dependence of ZIF-8 unit cell. Solid data represents an increase in pressure. The blue, pink and red open data show releasing of pressure from 2.5, 3 and 10 GPa respectively.....	59
Figure 4.2 (a) Total pair distribution functions (PDFs) data for structures formed at 0-50 GP pressure range. (b) Total PDFs for released pressure structures. (c) Coordination number (CN) of Zn as a function of pressure. (d) structural views of the frameworks obtained in this work.....	61
Figure 4.3 (a) Partial pair distribution functions of ZIF-8, ZIF-8-HP and apZIF-8, and amZIF-8. (b) Bond angle distributions for ZIF-8 and apZIF-8.	62
Figure 4.4 The uniaxial pressure dependence of ZIF-8 unit cell.....	64
Figure 4.5 Stress-strain curves of ZIF-8 unit cell.....	68
Figure 4.6 Calculated total and partial density of states (DOS) for (a) ZIF-8 and (b) apZIF-8.....	70
Figure 5.1 Equilibrium crystal structures of (a) ZIF-1, (b) ZIF-2, (c) ZIF-3. (d) Zn-Im-N coordination in a subunit.....	73
Figure 5.2 a) The volume and total energy per Zn plot as a function of pressure for ZIF-1 b) Normalized volume as a function of pressure for ZIF-1.....	75
Figure 5.3 Total pair distribution functions (PDFs) data for structures formed at -2.25-10 GP pressure range for ZIF-1.....	77

Figure 5.4 Partial pair distribution functions (PDFs) data for structures formed at - 2.25-10 GP pressure range for ZIF-1.....	78
Figure 5.5 a) The volume and total energy per Zn plot as a function of pressure for ZIF-2 b) Normalized volume as a function of pressure for ZIF-2.....	80
Figure 5.6 Total pair distribution functions (PDFs) data for structures formed at 0-10 GP pressure range for ZIF-2.....	82
Figure 5.7 Partial pair distribution functions (PDFs) data for structures formed at 0-10 GP pressure range for ZIF-2.....	83
Figure 5.8 a) The volume and total energy per Zn plot as a function of pressure for ZIF-3 b) Normalized volume as a function of pressure for ZIF-3.....	85
Figure 5.9 Total pair distribution functions (PDFs) data for structures formed at 0-10 GP pressure range for ZIF-3	86
Figure 5.10 Partial pair distribution functions (PDFs) data for structures formed at 0-10 GP pressure range for ZIF-3	87
Figure 5.11 Calculated total and partial density of states (DOS) for ZIF-1	89
Figure 5.12 Calculated total and partial density of states (DOS) for ZIF-1	90
Figure 5.13 Calculated total and partial density of states (DOS) for ZIF-1	90

List of Table

Table 2.1 Reported high pressure studies of MOFs.....	18
Table 3.1 Optimized structural parameters for MOF-5.....	43
Table 3.2 Calculated bond lengths for optimized structure and α -MOF-5.....	46
Table 4.1 Mechanical properties of ZIF-8.....	58





*To my wife Hatice
and
my daughter Umay*

Chapter 1

Introduction

Although amorphous materials have been known for a long time and have attracted considerable attention from the scientific community lately, when we consider solids, crystals come to the fore. For a long time, perhaps still, amorphous materials have been treated like Oliver Twist whom we have ignored both in the scientific world and therefore in our daily lives. So why? Of course, there are many reasons behind this, but now let us explain the most dominant two reasons below.

Unlike crystallography, there is no comprehensive and universal theory describing the atomic structure of amorphous solids.

Indeed, both types of materials have been known and used by mankind since ancient times. For example, in ancient Egypt, as far as we know from the discovered Pharaoh's tombs, both amorphous materials (colored glass) and crystal materials (quartz, emerald) were precious materials. Until modern times, people practically have used both types of solids for their purposes. The fact that crystalline materials have become more dominant in the scientific world when coinciding to the era in which science began to renew itself in the old world.

In the 17th and 18th centuries, Descartes, Newton and Leibniz's perspective on science was a precursor to their successors. From the beginning of the 19th century, the idea of enlightenment glowed by the fire of the Renaissance led to the fundamental changes in many areas of continental Europe and in New World. During this century, science has made great progresses. In the field of chemistry, the German chemist Friedrich Wöhler synthesized organic chemical urea from inorganic starting chemicals, which led to the emergence of organic chemistry as a sub-field of chemistry. The British chemist John Dalton published his theory,

which would inspire his successors, claiming that matter was made of tiny, invisible particles. Russian scientist Dimitri Mendeleev gave the periodic table the form that we use today. In physics, the Danish Hans Christian Oersted discovered that the electric current through a wire induces a magnetic field. The self-taught British genius Michael Faraday invented the electric motor. German physicist Hermann von Helmholtz formulated the law of conservation of energy. James Clerk Maxwell proved that light is actually an electromagnetic wave. Towards the end of the century, Joseph John Thomson discovered a negatively charged particle, which we would later call electron, using cathode rays. Still in this century, Darwin travelled to the South America and the Galapagos Islands, which would have a major impact on himself and indirectly on the world with his ideas and reports. The famous controversial work, *The Origin of Species*, was first published in 1859 by him. Louis Pasteur has proven that microorganisms cause diseases. The inventor Humphry Davy realized that inhaling ether relieved pain. Inspired from Davy, American dentist Henry H. Morgan began using ethers as anesthetic. Joseph Lister discovered antiseptic surgery. Thus, anesthetics and antiseptics made operations safer. In the field of astronomy, the Italian Giuseppe Piazzi discovered the first asteroid Ceres. Neptune, the most distant planet of the sun system, was also discovered in this century.

Crystallography is a branch of science that emerged in a relatively short time in the 19th century, as well. In 1822, the French mineralogist René Just Haüy, now known as the father of modern crystallography, published his research on crystal solids under the title of “*Traité de cristallographie*”. R. Haüy accidentally dropped the calcite crystal from his hand and broke it. When examining the fractured pieces on the ground, he was surprised by the smoothness of the fracture plane, which made him enthusiastic about performing further crystal cutting experiments. After many cutting experiments, Haüy concluded that each crystal has a basic primitive unit or linking molecule that could not be broken further without destroying its physical and chemical nature. Shortly thereafter, in 1839, Welsh mineralogist William Hallows Miller developed the hkl notation, called with his name after his death –Miller indices. A Miller index, hkl notation, is a

method which we use to define the orientation of a plane or set of planes within a unit cell. In 1848, French physicist Auguste Bravais discovered that 14 unique lattices are possible for 3-dimensional crystal systems. Today we call these lattice systems as Bravais lattices. In 1891, the Russian mathematician Evgraf Fedorov, in 1892 the German mathematician Arthur Moritz Schoenflies and in 1894 the British geologist William Barlow, each independently, discovered that only 230 symmetrical crystal arrangement forms, which we now call the space group, are possible. As a result, the theory of geometric crystallography has been completed in about 70 years.

In 1901, Wilhelm Röntgen's discovery of X-rays made it possible to prove these mathematically ideal, almost-perfectly ordered structures. Following year, Max von Laue proposed that x-rays passing through a crystal would diffract and generate a pattern, which could be recorded in a photographic film. This pattern, he proposed, could be a projection of the symmetrical arrangement of atoms within the crystal. In 1912, his theory was experimentally proved by Laue's two students. In 1913, William Henry Bragg and his son William Lawrence Bragg in England formulated the relationship between the atomic structure of a crystal and the X-ray diffraction pattern of the system, using Laue's findings. Using the formula known as Bragg's law today, the Braggs identified many crystal structures, including sodium chloride, zinc sulphide and diamond, from their diffraction patterns. The Braggs's work was a revolutionary discovery in order to understand the structure of a wide range of materials, from minerals to pharmaceuticals. So in summary, for more than a century, there has been a branch of science in which to determine the structure and properties of the crystalline materials, precisely.

Unfortunately it is not possible to say the same things for amorphous materials. Contrary to the comprehensive laws of crystallography, there are no well-established universal laws or rules that define the atomic structures of amorphous solids. [1] It is simple to elucidate the geometric structure of a crystal: there is a unit cell with relatively few atoms, and the crystalline structure is obtained by periodically repeating this unit cell in whole space. Such a procedure is not

possible for amorphous solids that do not have a periodic structure and are formed *randomly*. In this case, a question may come to mind: If amorphous solids have a random structure, why do we want to study the structure of an amorphous material? This is flogging a dead horse, isn't it? In fact, in answering this question, we will be somewhat contradictory to the aforementioned proposal. That is, amorphous solids do not actually have a long-range order (LRO), but they can have an order up to certain lengths. So, it is not possible to say that their structure is really random in statistical manner. The structure of many amorphous materials is in fact non-random at least at certain lengths and there is a considerable degree of a local structural arrangement, even if not periodic. This arrangement is called a short-range order (SRO). For example, silica and silicate in the glass phase are formed by randomly assembling the tetrahedral SiO_4 to some degree. However, in fact, the presence of each tetrahedral SiO_4 eliminates complete randomness in the structure (Figure 1.1).

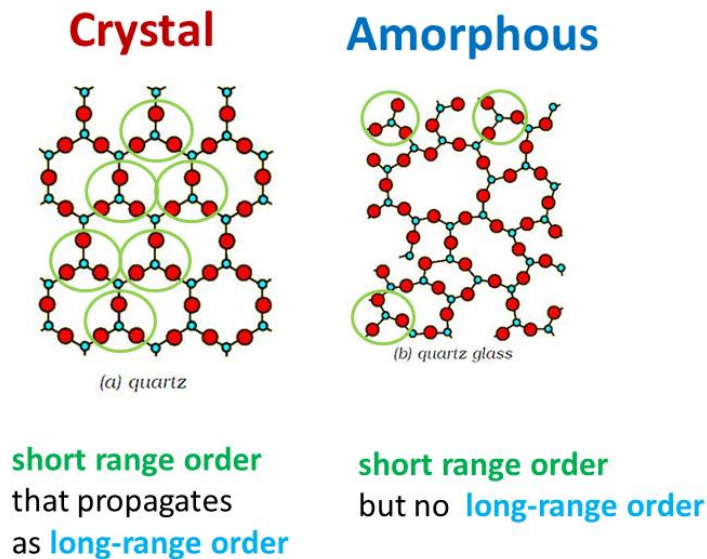


Figure 1.1 The atomic arrangement in crystalline and amorphous materials.

Similar local arrangement exists for any system in which there is a chemical bond (covalent, ionic or metallic) between atoms. Conventional experimental methods such as X-ray, neutron or electron diffractions are used to elucidate this local

arrangement. However, these techniques are particularly useful for monatomic amorphous systems. Determining the structure of amorphous systems with more than one type of atom is a very difficult task. The structure of binary compounds can be elucidated using diffraction techniques and its variants, anomalous scattering and magnetic neutron scattering. For systems consisting of more than two components, the situation is burdensome. The atomic structures of these systems can only be determined by using Extended X-Ray Absorption Fine Structures (EXAFS)[2]. Magnetic resonance (electron spin resonance (ESR)[3-6] or nuclear magnetic resonance (NMR))[7, 8] and vibrational spectroscopy (Raman)[9-11] do not directly provide information on their atomic arrangement, but it can give some supportive ideas on their bonding in SRO. Even though we can examine the structures of amorphous materials with many experimental techniques, the data obtained is quite limited. One method to overcome this problem is to develop models that mimic amorphous systems. The continuous random network (CRN) is the common structural model for non-metallic amorphous systems. The model developed to describe amorphous metals, ionic solids and some liquids is referred as the dense random packing (DRP) of hard spheres. All of these structural models are useful to examine to some extent the atomistic structure. However, each model is in fact an idealized variation of the atomic structure of amorphous solids. Unlike crystals, there is no unique structure in amorphous materials. As with CRN, systems formed by interconnecting a tetrahedral SiO_4 with different dihedral angles cannot be defined as a completely random structure.[12] In fact, each amorphous structure in itself defines a unique SRO. In crystallography, the structural variation is limited to the numbers 14 (Bravais lattices) and 230 (space groups), but in principle there are an infinite number of structural arrangements for amorphous materials.

The production of many amorphous materials may be laborious.

The difficulty here expresses two separate meanings. The first is technical difficulties in production. For example, the earliest known method of obtaining an amorphous solid is melt and quench. In this process, the molten material is cooled very quickly to obtain glass. Melted atoms have a random distribution.

When the melts begin to cool down, atoms have a tendency to arrange themselves in the lowest energy state, namely the crystalline state with long-order periodicity. When the system is cooled rapidly, the atoms cannot find enough time to reach their crystalline (equilibrium) positions, so they remain in a disordered structure without any periodic arrangement. So question is now: How quickly should we cool the melt to obtain a glass? This ratio, of course, varies according to the type of substances. For metallic glasses, for example, the cooling rate should be in the order of 10^6 Ks^{-1} and above. This is a very high value even for today's technology. Of course, for some materials with high glass forming ability, such as B_2O_3 , this value is quite low, around 1 Ks^{-1} . [12]

The second difficulty, as mentioned above, an amorphous material does not have a unique structure, and infinite different structural formations are possible for an amorphous solid depending on the preparation technique. Therefore, it is difficult to produce the same amorphous material with different production techniques, or to prove that the structures are geometrically identical even if they are produced. Even the same production methods can lead to different amorphous systems unless sufficient attention is paid to the various production parameters. In short, reproducibility is a very problematic issue for amorphous materials.

Contrary to the desperate picture we have drawn above, interest in amorphous materials is increasing day by day. So why? Because amorphous materials, just like their atomic structure, have many unique properties unlike crystals. Therefore, it is scientifically important to clarify the structures of amorphous materials.

In this context, pressure-induced amorphous phases of metal-organic frameworks, a new type of material, were investigated in this study. Metal-organic frameworks are porous materials formed by the combination of metal nodes with organic ligands. The research, which began in 1995 with the discovery of the first MOFs by Omar Yaghi and his friends, [13] has become an area of interest today, where thousands of academic publications are published each year. MOFs attract researchers from many different disciplines because of their characteristics in which to contribute to several sustainable development goals set by the United

Nations (UN).[14] For example, MOF-based water harvester, developed by Yaghi et al.,[15] converts the water in air into drinkable water even in low humidity environments. MOFs have also been reported as a suitable material for many energy applications; storage of energy carriers such as hydrogen and fuel as methane, solar energy conversion applications, and electrical energy storage and conversion systems[16]. Recently it has been shown that MOFs can be used in wastewater treatment and removal agricultural wastes from groundwater[17].

Obviously, MOFs are now an engineering material in many areas such as gas adsorption or separation. From a practical point of view, an engineering material is resistant to the mechanical stimuli to which it is subjected during processing and application is an important parameter. However, in recent years there has been growing interest in studies investigating the behavior and the mechanical properties of MOFs under high pressure.[18] Although most of the MOFs are crystalline, amorphous MOFs of considerable number with interesting structural properties for promising applications have been reported to a small extent in the literature.[19]

In this thesis, we investigated the behavior of different MOFs under hydrostatic and uniaxial high pressure by using ab-initio molecular dynamics simulations (AIMD). After providing a scientific background in Chapter 2, we present our work on pressure-induced amorphization in MOF-5 in Chapter 3. In Chapter 4, we present a study on the behavior of ZIF-8 under high pressure, pressure-induced phase transitions, mechanical and electronic properties. We have studied the pressure-induced phase transitions of ZIFs polymorphs in Chapter 5. Finally, we conclude the thesis by making final remarks and giving a future outlook in Chapter 6.

Chapter 2

Scientific Background

This thesis covers the ab-initio molecular dynamics (AIMD) studies on pressure-induced amorphization of metal-organic frameworks (MOFs), and their structural, electronic and mechanical properties at high pressure. Before presenting the details of our works, we find beneficial to give some background information. In this context, we first provide brief information on amorphous solids. Then, we continue with an introduction to MOFs and a literature review on their high pressure studies. Subsequently in next two parts, the theories of AIMD and structure analysis methods are presented.

2.1 Amorphous Solids

The Greek roots of amorphous are clear: morphē means "form," and a- means "lacking or without." [20] In physics and materials science, an amorphous solid or non-crystalline solid where in atoms or molecules are not packing in a definite lattice pattern, namely they are lack of long-range order as crystals have. Early on, while the term "amorphous" has been used synonymously with glass, today glass is considered to be subset of amorphous solids, which has a glass-transition property. [1, 12]

Although there are a lot of uncertainties about both the formation and structure of many amorphous materials, they are attracting increasing interest due to their extraordinary properties. So far, two common methods for production of amorphous solids have been used: quenching from melt and solid-state amorphization (SSA). [12]

2.1.1 Quenching from Melt

The most common method used to make a glass substance from a crystal is melting. The process is thermodynamically depicted in Figure 2.1. When the liquid is cooled down to any temperature below the melting temperature, the state usually transforms into a crystalline state, which has periodicity and long-range order. In such a case, the enthalpy abruptly drops to an enthalpy value, which is appropriate for a crystal. The cooling of the crystal from this point will cause an extra decrease in enthalpy due to the crystalline state heat capacity. If the liquid is cooled to below the melting temperature without crystallization, then, a supercooled liquid is obtained. As temperature decreases, liquid rearrangement continues, but due to the disordering in rearrangement, no sharp decrease in enthalpy is observed. When the liquid is heated, its viscosity will increase. When viscosity reaches a threshold point, the atoms can no longer be fully rearranged in the equilibrium liquid phase. From this point on, the enthalpy begins to shift from the line of equilibrium and follows a decreasing curve. When the viscosity is too high, the liquid remains the same and is no longer temperature dependent. The temperature zone of the enthalpy between the equilibrium liquid and frozen solid is defined as the glass transformation range. The frozen solid is now a glass.[21]

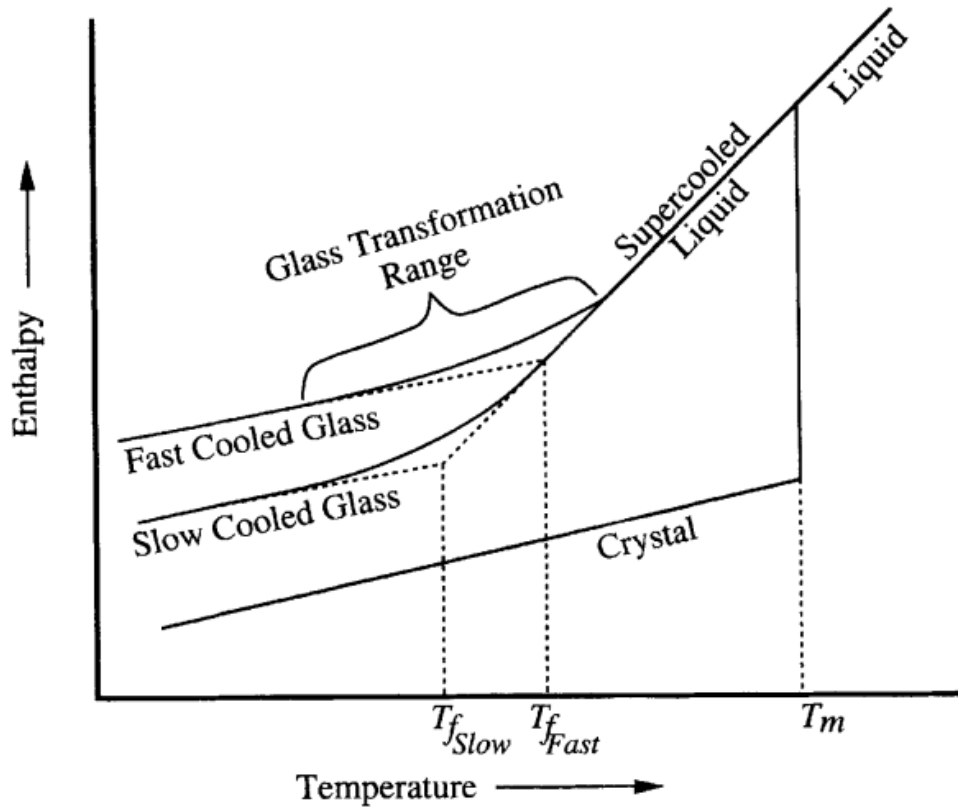


Figure 2.2 Effect of temperature on the enthalpy of a glass forming melt

2.1.2 Pressure-Induced Amorphization

Until the 1980s, there were two common methods for the production of amorphous materials: the first is, as described in details above, the quenching from melt, and the other is the condensation of the vapor phase on a cold substrate. Both methods have long been traditional methods for the production of amorphous materials, both commercial scale and in laboratories. Many different types of equipment have been developed for achieving rapid cooling. However, especially in materials with low glass forming ability, such as metals, the formation of amorphous material from the vapor or molten phase requires a very high cooling rate. This imposes certain limitations on the dimensions of the material to be produced. In order to eliminate these limitations, especially after 70s, methods for the production of amorphous materials without vapor or liquid

phase were developed. These include: by prolonged grinding of alloys or mixtures of elements in ball mills, amorphization of metal alloys upon hydrogen absorption at moderate temperatures, under intensive irradiation of samples, by anomalous diffusion on contact of two different crystal materials. All these techniques are called solid-state amorphization (SSA). Since SSA techniques do not require very high quenching rates, amorphous materials can easily be produced in very high quantities. [22]

Among the SSA methods, pressure-induced amorphization (PIA), in which pressure is used as a driving force for amorphization, is a method of particular interest in the literature.[22] The rearrangement (disordering) process in PIA is different from thermally initiated disorders. It is therefore essential for understanding the phenomena of disorder in condensed matter and computational physics, including solid state amorphization and stability of crystals. However, the underlying mechanism of PIA remains one of the most impressive open questions. Some separate possibilities have been proposed as driving forces for such a solid state amorphization.[23-26]

Chronologically, the first proposed mechanism for PIA is a metastable melting process. In 1984 Mishima et al. [27] discovered that when hexagonal-ice (ice-Ih) cooled down to 77 K and pressurized to 1 GPa, it could not transform into crystalline ice-IX and became amorphous. According to this heuristic argument as depicted in Figure 2.2, a low pressure phase A has a negative melting slope, which is intersected by a transition into a dense phase B at high pressure. But, when the compression is applied at low temperature –even to absolute zero– such that the crystalline phase transition is kinetically impeded, under glass transition temperature (T_g), the system can intersect the metastable extension of the melting line A. Under such a circumstance, metastable compressed crystal transforms into an amorphous phase. Due to the definition such an amorphization process is called as “pressure-melting” or “pseudo-melting”. After Mishima’s inspired work, many studies on ice amorphization induced by pressure were reported over the last few years. [28-37]

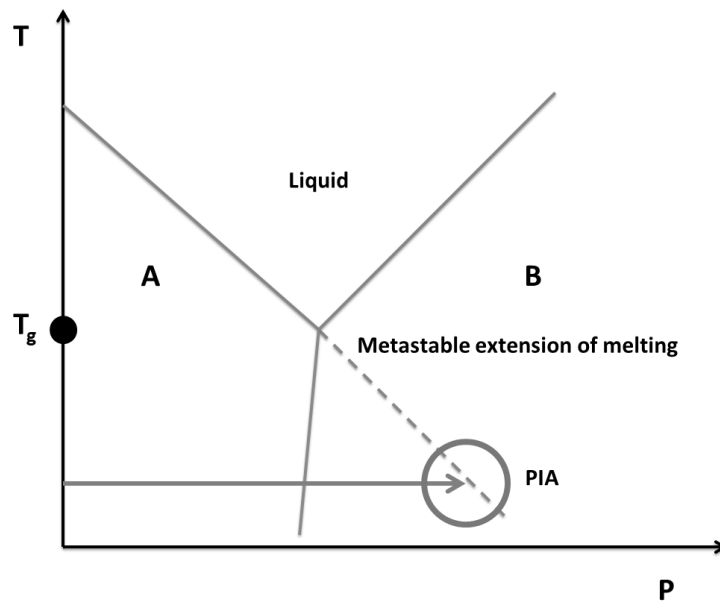


Figure 2.2 Graphical illustration of pressure-induced amorphization (PIA) as metastable melting event

In 1992, by N. Binggeli and J. R. Chelikowsky reported that PIA in α -quartz has mechanical nature and amorphization is due to the weakening of a shear modulus. [38] In their study, they observed the amorphization of quartz when the structure approaches a spinodal boundary associated with an elastic instability. By using ab initio pseudopotential approach and simple ionic model, they analyzed the atomistic mechanism behind this instability, and concluded its connection with a change in the Si coordination. Later, several amorphizations in different materials were explained based on this theory in the literature. [39-42]

According to another theory, the displacive formation of a noncrystallographic packing based on polytetrahedral units causes amorphization. However, the authors stated that polytetrahedral ordering is applicable to nondirectionally bonded materials; its application to solids with covalent and hydrogen bonding is not immediately evident. [43]

It is also proposed that the formation of a metastable glassy phase depends on the existence of kinetic hindrances which impede the formation of more stable

equilibrium crystalline phases. Namely, a crystal-to-amorphous phase transition occurs when a non-equilibrium state of a crystalline solid has a free energy which is greater than that of an amorphous phase. [44, 45]

2.2 Metal-Organic Frameworks (MOFs)

Metal-organic frameworks (MOFs) are crystalline/amorphous porous materials constructed from a combination of coordinatively bonded multitopic organic linkers and metal/metal cluster nodes.[46] The term coordination polymer was first seen in the literature in the 1960s, but significant progress in this area was made in the 1990s by Omar Yaghi et al.[13] with naming these materials as metal-organic frameworks. The most important properties of MOFs are porosity, which makes them similar to traditional porous materials, zeolites. The surface area of 1 gram MOF is comparable to 1 football field (5351 m²). This exceptional surface area makes MOFs an important material for the storage of gases such as hydrogen, methane, carbon dioxide.[46] Of course, their application areas are not limited to gas storage. One of the most important features of MOFs is their structural flexibility, such that these materials can be designed desirable properties with many applications with various modifications both before and after synthesis.[47] In addition, these properties, coupled with their high surface area and low density, make MOFs promising materials in many research areas: liquid phase separation,[48] drug delivery,[49] chemical sensing,[50] heterogeneous catalysis,[51] fuel cells,[52] batteries,[53] super capacitors,[53] water harvesting,[15] solar energy conversion[54] and electronic applications.[55]

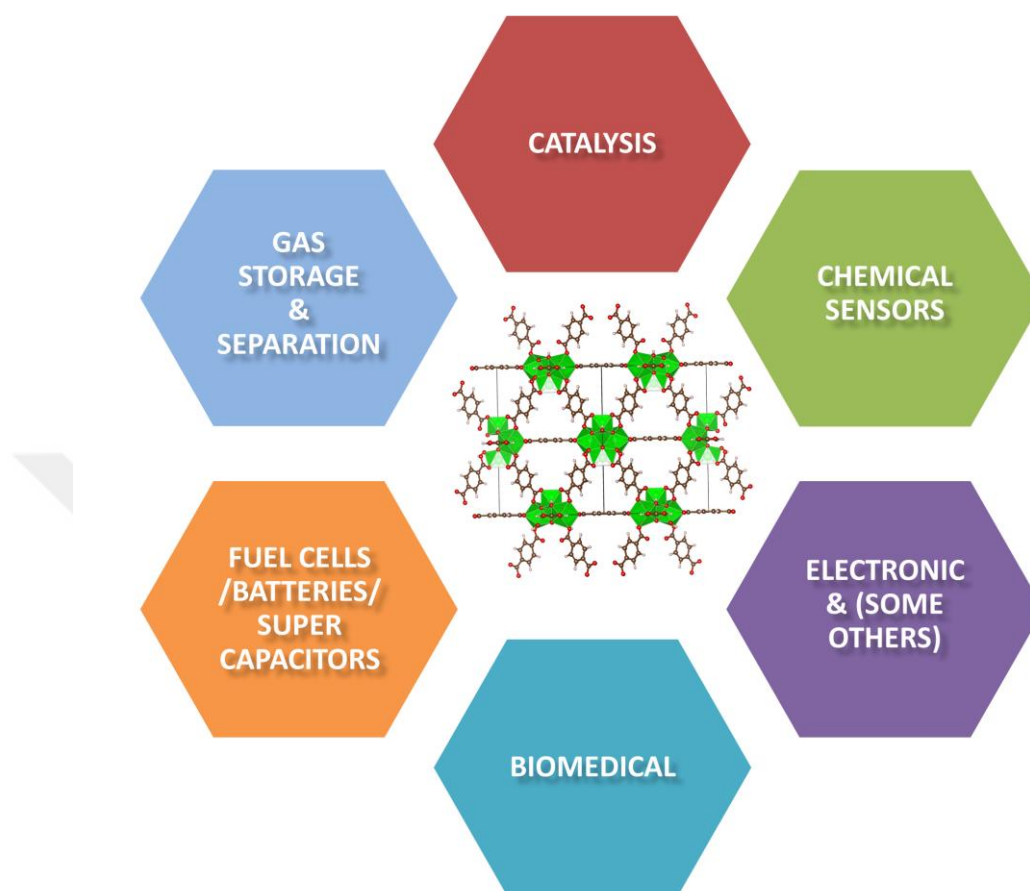


Figure 2.3 Widespread potential applications of metal-organic frameworks (MOFs) [56]

2.2.1 The Literature Survey: Pressure-Induced Amorphization in MOFs

Researchers working on the MOF have been interested in crystalline MOFs for a long time. In fact, in many articles published so far, MOFs have been emphasized that they are “crystal”. However, since 2010, numbers of studies involving non-crystalline MOFs have been increasing steadily in the literature. The definition of an amorphous MOF is somewhat similar to its crystalline counterpart: an amorphous MOF is a network formed by the linking of inorganic nodes with organic ligands. The difference between these two is as follows: In amorphous MOFs, unlike crystalline MOFs, there is no long-range order. In the

literature, different methods have offered to produce amorphous MOFs including ball milling, pressurization and heating (without melting).

Mechanochemistry, one of the green chemistry synthesis methods, has been introduced as an alternative to the traditional synthesis method of MOFs (e.g. hydrothermal), and in recent years many researches have been published papers on the synthesis of MOFs with mechanochemistry.[57-69] In the ball milling process, the continuous collision of small steel balls produces localized high pressure in a closed container. This high pressure can be used as a driving force to overcome the activation energy in the synthesis of MOFs. What if we expose a crystalline MOF to this ball milling process? One of the first studies on making amorphous MOF by ball-milling was reported by S.Cao et al.[70] In this study, the ZIF-8 crystal was subjected to ball milling for 30 minutes, and the structure underwent an irreversible amorphization. Later, in both experimental and computational DFT and classical MD studies, it was emphasized that the origin of this amorphization was shear-mode softening.[71, 72] Also, according to these reports, there is no bond breakage during amorphization and the coordination around Zn^{2+} is maintained. In another study on ZIFs, Bennett et al. used the ball-mill amorphization method for ZIF-1, ZIF-2, and ZIF-4 polymorphs, and observed an irreversible amorphization in all structures. [73] In another report [74] published by the same group, when the UiO-66 was milled at 20 Hz for 10 minutes, the structure underwent an amorphization. They stated that unlike ZIF-8, some of the bonds between the carboxylate linker and $Zr_6O_4(OH)_4$ broken in amorphous UiO-66. However, no change was observed for the bonds in the $Zr_6O_4(OH)_4$ cluster. Ball-milled amorphization was also observed in MIL-140 series MOFs, as reported in the same article. However, unlike UiO-66, bond breakages were observed in this framework both in inorganic nodes and also between inorganic nodes and ligands.

In the view of their applications, by using this amorphization method, the guest molecules were trapped in MOFs in some reported papers. In 2013, the irreversible trapping of I_2 , a nuclear waste, in ball-milled induced amorphous ZIFs was demonstrated.[75] In this study, the evacuated ZIF-4, ZIF-8 and ZIF-

69 crystals were first exposed to I₂ vapor at 77 ° C. After this adsorption, I₂ @ ZIFs materials were ball-milled for 30 minutes at 25 Hz. After this process, the excess I₂ molecules on the surface were removed by heating at 125 ° C. According to the results of the microanalysis, ZIF-8 was the best material for both uptake and retention of I₂ due to the contribution of methyl groups on imidazolate ligands. In another study reported by David-Fairen Jimenez et al.,[76] the drug calcein, selected as a model cancer drug, was incorporated into the MOF by suspended UiO-66 in calcein solution. The resulting calcein @ UiO-66 material was then ball-milled to yield amorphous calcein @ amUiO-66. When drug release duration of both crystal and amorphous resulting materials were investigated, it was observed that crystal UiO-66 released the drug in only 2 days, while the amorphous structures were releasing all drugs up to 30 days. In addition to ball milling, amorphous MOFs were simply obtained by using hydraulic piston. For example, when MOF-5 powder crystal was subjected to a uniaxial pressure by hydraulic press, an irreversible amorphization has been seen at 3.5 MPa.[77] In this study, the resulting solid state amorphization was confirmed by Raman spectroscopy and XRD. In different study, the crystal UiO-66 was subjected to compression by using a similar process up to 1.9 GPa. [78] According to the detailed EXAFS results, there was no change in the Zr-O bonds in the Zr₆O₄ (OH)₄ node, while there was a decrease of 10% in the Zr-OOC bonds at 1.9 GPa.

Another technique commonly used in high pressure studies is diamond anvil cell (DAC) experiment. In the method, the DAC container holds the material between two diamonds units while the sample is pressurized with a fluid defined as pressure transmitting medium (PTM). There are a few DAC experiments on ZIF-8 reported in the literature. In first the study reported by Moggach et al. in 2009, methanol / ethanol was used as PTM. [79] Initially, an expansion in the framework was observed since the pressure exerted by PTM on the structure was sufficiently small. As the pressure increased, a decrease in volume was observed compared to the initial volumetric expansion. This trend lasted up to 1.47 GPa. At this point the structure underwent a crystal-crystal phase transition

due to the twisting of MIm groups. Chapman et al.[80] reported that ZIF-8 underwent an irreversible amorphization at 0.34 GPa under non-hydrostatic pressure. Hu et al.[81] investigated the structural changes in ZIF-8 in the PTM-free DAC experiment up to 39 GPa by in situ FTIR. According to their results, the framework was subjected to reversible structural changes up to 1.6 GPa, but at compression values beyond this pressure, the structure exhibited an irreversible crystal-amorphous phase transition. However, at very high pressures, no change in the short-range coordination of a structure was observed. Moggach et al. stated that in the high-pressure experiment for MOF-5, in which DEF was used as PTM, the structure retained its crystallinity up to 3.2 GPa, but beyond this pressure, the structure was completely amorphous.[82] In a study on Cu-BTC, methanol / ethanol / water (MEW), IPA, FC-70 were used as PTMs.[83] Chapman et al. concluded that when MEW and IPA were used as PTM, two different linear compression regions were observed between two different close regions, indicating that the solvents penetrated into the structure. The smaller molecular size MEW compared to IPA caused the transition pressure to shift from 0.8 GPa to 2.2 GPa. However, when FC-70 was used as PTM, which did not penetrate the structure, a direct compression was observed in the framework. As a result they pointed out that filling the pores with PTM solvent made the structure more resilient. In the publication reported by Gagnon et al., the volume of ZAG-4 ($\text{Zn}(\text{HO}_3\text{PC}_4\text{H}_8\text{PO}_3\text{H}) \cdot 2\text{H}_2\text{O}$) decreased by 27% between 0-9.9 GPa, according to the results of DAC experiments using a methanol / ethanol mixture as PTM. When the pressure was released from 9.9 GPa, the structure recovered all the volume which was initially lost. No amorphization onset or failure pressure was observed in the pressure range for this structure. They claimed that the relatively high compressibility and this reversible transition was a result of spring-like behavior of long alkyl chains in the framework. [84]

As can be seen from the studies in the aforementioned literature, although the DAC experiments are often useful in investigating the behavior of MOFs under pressure, the reliability of the results is always questionable. The most important

reason for this is that the MOFs can easily fill with PTM molecules during the DAC experiments due to their high surface area and accessible pore sizes, and this process makes them more resilient. Along with this more resilient structure and strong PTM molecules-frameworks interaction, changes (delaying) are observed in transition pressures.

In the system prepared by Suslick[85] to eliminate host-guest effects is evacuated single MOFs crystals are compressed under uniaxial stress. In 2015, Suslick et al. used in situ TEM compression test for ZIF-8, and found an onset value of 3 GPa for amorphization pressure under uniaxial pressure.[85] In the same study, the amorphization pressure for bulk powder was 1.1 GPa. The researchers attributed the pressure difference to the interaction of microcrystals each other in the powder sample. In a different study, Suslick et al. used the same system for UiO-66, they determined the amorphization pressure as 2 GPa. [78]

Name	Composition	method	reference
ZIF-1	Zn(Im) ₂	ball-milling	[86]
ZIF-2	Zn(Im) ₂	ball-milling	[86]
ZIF-3	Zn(Im) ₂	ball-milling	[86]
ZIF-4	Zn(Im) ₂	ball-milling	[86]
Co-ZIF-4	Co(Im) ₂	ball-milling	[86]
ZIF-8	Zn(mIm) ₂	ball-milling	[70]
ZIF-8	Zn(mIm) ₂	DAC	[80]
ZIF-8	Zn(mIm) ₂	DAC	[81]
ZIF-8	Zn(mIm) ₂	in-situ TEM compression	[85]
MOF-5	Zn ₄ O(BDC) ₃	hydraulic press	[77]
MOF-5	Zn ₄ O(BDC) ₃	DAC	[82]
UiO-66	Zr ₆ O ₄ (OH) ₄ (BDC) ₆	ball-milling	[82]
UiO-66	Zr ₆ O ₄ (OH) ₄ (BDC) ₆	in-situ TEM	[78]
MIL-140b	ZrO(ndc)	ball-milling	[74]
MIL-140c	ZrO(bpdc)	ball-milling	[74]
ZIF-7	(Zn(PhIm) ₂	DAC	[87]
ZIF-9	(Co(PhIm) ₂	DAC	[87]
ZIF-62	[Zn(Im) _{1.75} (bIm) _{0.25}]	DAC	[88]

Table 2.1 Reported high-pressure studies of MOFs

2.3 Density Functional Theory (DFT)

The famous physicist Paul Davies notes that many older scientists might regard the first thirty years of the twentieth century as a golden age of physics, historians may, instead, regard it to be the starting days of the “New Physics.” [89] In 1927 L.H. Thomas in Cambridge and Enrico Fermi in Rome separately, innovated a novel statistical model which defines the distributions of electrons in the atom. Later, Paul Adrien M. Dirac, Carl Friedrich and Freiherr von Weizsäcker presented the idea of defining the energy of atoms as a function of electron density. In his seminal paper of 1929, Dirac said that:[90]

“The general theory of quantum mechanics is now almost complete. . . . The underlying physical laws necessary for the mathematical theory of a large part of physics and the whole of chemistry are thus completely known. . . . It therefore becomes desirable that approximate practical methods of applying quantum mechanics should be developed, which can lead to an explanation of the main features of complex atomic systems without too much computation.”

The physicists and chemists, inspired by the pioneers of the field, started a race to develop a model which is capable of calculating the eigenvalues of the atoms, molecules and solids. In the mid-1960s, Walter Kohn, Pierre Hohenberg ve Lu Jeu Sham developed the DFT (Density Functional Theory) by combining quantum mechanical effects with electron density.[91]

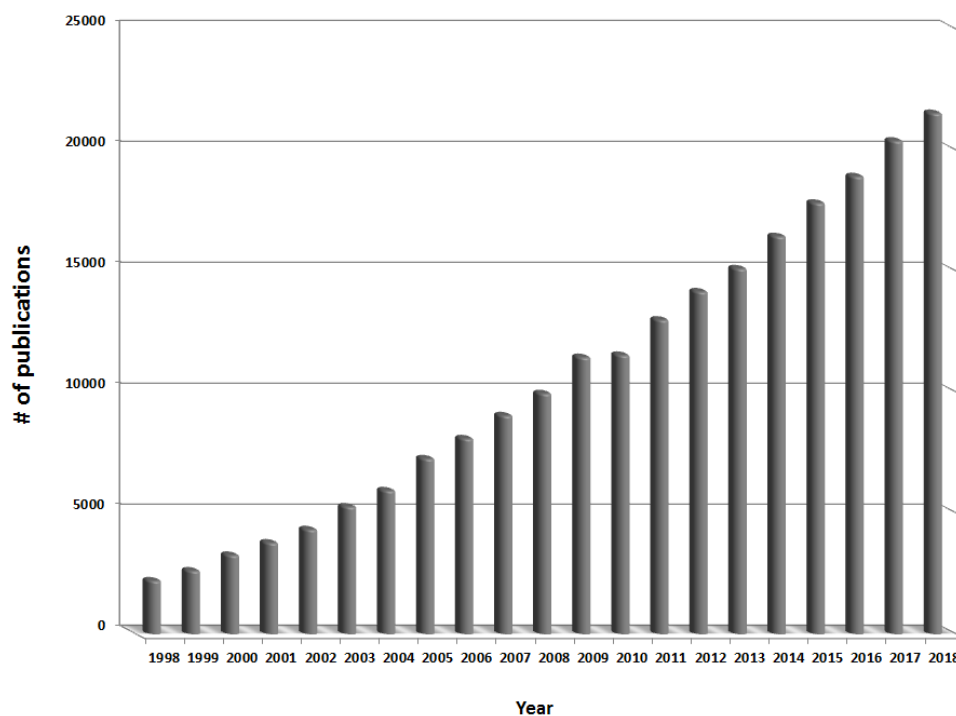


Figure 2.4 Number of articles containing the keyword “DFT” or “density functional theory” (data obtained from ISI Web of Knowledge)

After the implementation of DFT in software by Anthony Pople, it has become one of the most popular methods for calculating the chemical properties of atoms and molecules. Since the beginning of 1990s, it has been one of the most commonly used methods in the fields of chemistry, physics, materials science and geology. The DFT community has consistently come up with new solutions for problems they face with, and brought theories to higher levels. The success of this self-innovative method is also evident in Figure 2.4, which shows the number of publications produced by DFT for the last 20 years.

2.3.1 The mathematical foundations of DFT

For the nonrelativistic, time-independent form of Schrödinger equation can be written as,

$$H\psi = E\psi \quad (2.1)$$

where E is the total energy of a system and $\Psi = \Psi(r_1, r_2, \dots, r_N; R_1, R_2, \dots, R_M)$ is its many-body wave function with N -electrons and M -nuclei, and H is the Hamiltonian operator given by in atomic units:

$$H = T_e + T_n - V_{en} + V_{nn} + V_{ee}$$

$$T_e = -\frac{1}{2} \sum_i^N \nabla_i^2 \quad T_n = -\frac{1}{2} \sum_I^M \frac{\nabla_I^2}{m_I}$$

$$V_{en} = \sum_i^N \sum_I^M \frac{Z_I}{|r_i - R_I|} \quad V_{nn} = \sum_{I < J}^M \frac{Z_I Z_J}{|R_I - R_J|} \quad (2.2)$$

$$V_{ee} = \sum_{i < j}^N \frac{1}{|r_i - r_j|}$$

In these equations, T and V refer to kinetic energy and interaction potential operators, respectively. e and n subscripts are abbreviation of electron and nucleus. Z is the number of protons in the nucleus, and m denotes the mass of electron or nucleus. Thus, in equation 2.2, the first two terms represent the kinetic energy of electron and nucleus. V_{en} , V_{nn} and V_{ee} signify the electron-nucleus, the nucleus-nucleus and electron-electron interactions, respectively.

2.3.2 Born-Oppenheimer Approximation

A proton is about 2000 times heavier than an electron. When we consider an atom, the truth is that the nucleus of the atom is at least as heavy as three orders of magnitude of the electrons of an atom. The Born-Oppenheimer (BO) approximation is based on this fact. In order to solve the Hamiltonian given equation 2.2, this approach is used, so it is assumed that the electrons move in the potential created by positively charged nuclei, which is fixed a point in space. Thus, the BO approximation allows us to separate the total wave-function into two parts: an electronic part and a nuclei part.

$$\psi(r, R) = \psi_R(r) \chi(R) \quad (2.3a)$$

$$H_r \psi_R(r) = E_R \psi_R(r) \quad (2.3b)$$

$$H_R \chi(R) = E \chi(R) \quad (2.3c)$$

In the equations, $\psi_R(r)$ is the electronic wave-function, including the parametrically position of nucleus R, and $\chi(R)$ is the nuclear wave-function. In this case, it is also possible to divide the Hamiltonian into two parts:

$$H_R = T_n + V_{nn} + E_R \quad (2.4)$$

$$H_r = T_e + V_{ee} + V_{ne}$$

However, for the ground and excited states, where the electronic potential energy surfaces are very close to each other, the use of the BO is not suitable.

When we put the BO equations given above into the Schrödinger equation, we get the following equation.

$$\begin{aligned} [T_n + V_{nn} + H_r] \psi_R(r) \chi(R) = & \psi_R(r) \left[-\frac{1}{2} \nabla_I^2 + V_{nn} + E_R \right] \chi(R) - \frac{1}{2} [\nabla_I^2 \psi_R(r)] \chi(R) \\ & - [\nabla_I \psi_R(r)] [\nabla_I \chi(R)] \end{aligned} \quad (2.5)$$

The last term in the equation is the non-adiabatic correction term, originating from the coupling of electronic and nuclear wave-function due to the kinetic operator. Looking at the last equation we see that the BO approximation comprises of omitting the contribution of the first-order term ($\nabla_I \psi_R(r)$) and the second-order term ($\nabla_I^2 \psi_R(r)$) because of the difference between the electron and nuclei masses. If the non-adiabatic contribution originating from the last part of equation 2.5 is set to 0, we get only equation 2.3c.

2.3.3 Electron Density

Though the separation of wave-function into nuclear and electronic wave-functions by the BO approximation is useful, the solving of the equation 2.1 is still remains onerous, because the many body wave-function is a function of

each of the coordinates of all N electrons. For example, for a single molecule H_2O , the total wave-function is a 40-dimensional wave function. If we are working on a nanocluster with 100 Pt atoms, the full wave-function includes more the 23000 dimensions. Fortunately, with introducing the electron density we can avoid using the full electron wave-function. The particle density is given by,

$$\rho(r) = N \int dr_2 \dots \int dr_N \psi^*(r_1, r_2, \dots, r_N) \psi(r_1, r_2, \dots, r_N) \quad (2.6)$$

Normally, in Quantum Mechanics, the observables (for this case such as density) are calculated by using wave-function. Using the electron density as the main variable is warranted by the Hohenberg and Kohn theorems [92], described in the following section.

2.3.4 Hohenberg-Kohn Theorems

At the hearth of DFT, there are two theories, which were proved by Hohenberg and Kohn (HK). The first HK theorem simply states that:

1. For any system of interacting particles in an external potential $V_{\text{ext}}(r)$, the density is uniquely determined.
2. A universal functional for the system energy $E[\rho]$ can be defined in terms of the density $\rho(r)$. The exact ground state is the global minimum value of functional $E[\rho]$.

Second theorem denotes that the expected values of T , V_{ee} and V_{ne} are functionals of the density as well. Hence, we can describe the so-called universal functional $F[\rho]$ as:

$$F[\rho] = T[\rho] + V_{ee}[\rho] \quad (2.7)$$

The “universal” term mean that functional does not depend on the particular disposition of the nuclei in the system. However, V_{en} is a non-universal functional which depends on the system:

$$V_{en}[\rho] = \int dr v(r) \rho(r) \quad (2.8)$$

To compute the ground-state density of a system, the minimization of the energy functional $E[\rho]$ with respect to $\rho(r)$ is defined as:

$$E[\rho] = T[\rho] + V_{ee}[\rho] + \int dr v(r) \rho(r) \quad (2.9)$$

The problem with solving above equation is that the universal functional $F[\rho]$ is not known exactly. Fortunately, Kohn-Sham approach provides a solution for this obstacle.[92]

2.3.5 Kohn-Sham Equations

The main obstacle in the energy functional is description of T as a function of ρ and its minimization. To overcome this problem, Kohn and Sham separated the T into two parts: (i) T_s presents the kinetic energy of non-interacting particle of density ρ , (ii) T_c represent the kinetic energy of interacting particle of density ρ .

$$T[\rho] = T_s[\rho] + T_c[\rho] \quad (2.10)$$

T_s can be written in terms of the single particle-orbitals $\phi_i(r)$ of a non-interacting system with density ρ ,

$$T_s[\rho] = -\frac{\hbar^2}{2m} \sum_i^N \int dr \phi_i^*(r) \nabla^2 \phi_i(r) \quad (2.11)$$

This equation is an explicit orbital functional. It is possible to apply the same separation technique on other universal functional V_{ee} . It can be written down a summation of Coulomb integral of Hartree-Fock, which depends on the electrostatic interaction of the charge distribution ρ , i.e. $J[\rho]$, and the remainder V_{ee-r} :

$$U[\rho] = J[\rho] + V_{ee-r}[\rho] \quad 2.12$$

The summation of the unknown terms $T - T_s$ and $V_{ee} - J$ gives a new universal functional so-called the exchange correlation functional:

$$\begin{aligned} E_{xc}[\rho] &= T_c[\rho] + V_{ee-r}[\rho] \\ &= T[\rho] - T_s[\rho] + U[\rho] - J[\rho] \end{aligned} \quad (2.13)$$

By using Lagrange multipliers, universal functional is written:

$$\delta \left[T[\rho] + V_{ee}[\rho] + \int dr v(r) \rho(r) - \mu \left(\int dr(r) \rho(r) - N \right) \right] = 0 \quad (2.14)$$

Giving the Euler-Lagrange equation:

$$\mu = \frac{\delta T[\rho]}{\delta \rho} + \frac{\delta V_{ee}[\rho]}{\delta \rho} + v(r), \quad (2.15)$$

the corresponding Euler-Lagrange equation for the Kohn-Sham approximation takes form:

$$\mu = \frac{\delta T_s[\rho]}{\delta \rho} + v_{KS}(r) \quad (2.16)$$

where the Kohn-Sham (KS) potential ($V_{KS}(r)$) is given:

$$\begin{aligned} v_{KS}(r) &= v_{ext}(r) + \frac{\delta J[\rho]}{\delta \rho} + \frac{\delta E_{xc}[\rho]}{\delta \rho} \\ &= v_{ext}(r) + v_H(r) + v_{xc}(r) \end{aligned} \quad (2.17)$$

Now, the ground-state density is a solution of a non-interacting-like Schrödinger equation, called Kohn-Sham equation:

$$\left[-\frac{\hbar^2 \nabla^2}{2m} + v_{KS}(r) \right] \varphi_i(r) = E \varphi_i(r) \quad (2.18)$$

Here the global wave-function is re-built as a single Slater determinant of made of φ_i :

$$\psi_{KS} = \frac{1}{\sqrt{N!}} |\varphi_1(r_1), \varphi_2(r_2), \dots, \varphi_N(r_N)| \quad (2.19)$$

In order to solve this set of equations, an iterative procedure is required. Since all variables are function of $\rho(r)$, the first step in the proposed algorithm is choosing initial value of $\rho(r)$. Once it is chosen, it can be calculated corresponding V_{KS} , and solved the Schrödinger-like equation (Equation 2.18) for φ_i . By using particle density equation with φ_i , a new density can be calculated. This iterative process is repeated until it converges in the named “self-consistent field” (SCF) loop.

2.3.6 Approximations of the Exchange-Correlation Functionals

If the exchange-correlation functional (E_{xc}) were explicitly known, Kohn-Sham ansatz would be perfect method for obtaining the ground state energy and electron density of a physical system. Unfortunately, there is currently no method to describe the E_{xc} exactly. Up to now, a list of functionals with

improved accuracy has been proposed. In 2001, the evolution and sorting of these approximations were embodied in analogy with Jacob's ladder by Perdew et al.[93] As re-illustrated in Figure 2.5., in their metaphor the ground state is Hartree theory while Heaven is perfect (ideal) density functional. The successive rungs from earth of Hartree to heaven of chemical accuracy show the different exchange correlation functions. The first rung is occupied by local (spin) density approximation (LDA) and it uses only $\rho(r)$. The second corresponds to generalized gradient approximation (GGA) and employs the density gradient ($\nabla\rho(r)$). The third is occupied by meta-GGA and uses the kinetic energy density τ or Laplacian of electron density. The fourth rung corresponds to hyperGGA, including Hartree-Fock (HF) constitute. The last rung to heaven would include exact exchange and exact partial correlation terms. In this analogy, from down to up accuracy increases, but less simplicity in functional cause an increase in computation cost.

In addition these functional, hybrid functionals (HFs) are a class of approximations to the exchange–correlation energy functional that incorporate a portion of exact exchange from Hartree–Fock theory with the rest of the exchange–correlation energy from other sources (ab initio or empirical). The exact exchange energy functional is expressed in terms of the Kohn–Sham orbitals rather than the density, so is termed an implicit density functional. The most commonly used HFs are B3LYP (Becke, 3-parameter, Lee–Yang–Parr) and PBE0 (the Perdew–Burke–Ernzerhof).[94, 95]

In practical view, the optimum method can be chosen for on studying physical system. In this thesis we used GGA-PBE[96] exchange correlation functional.

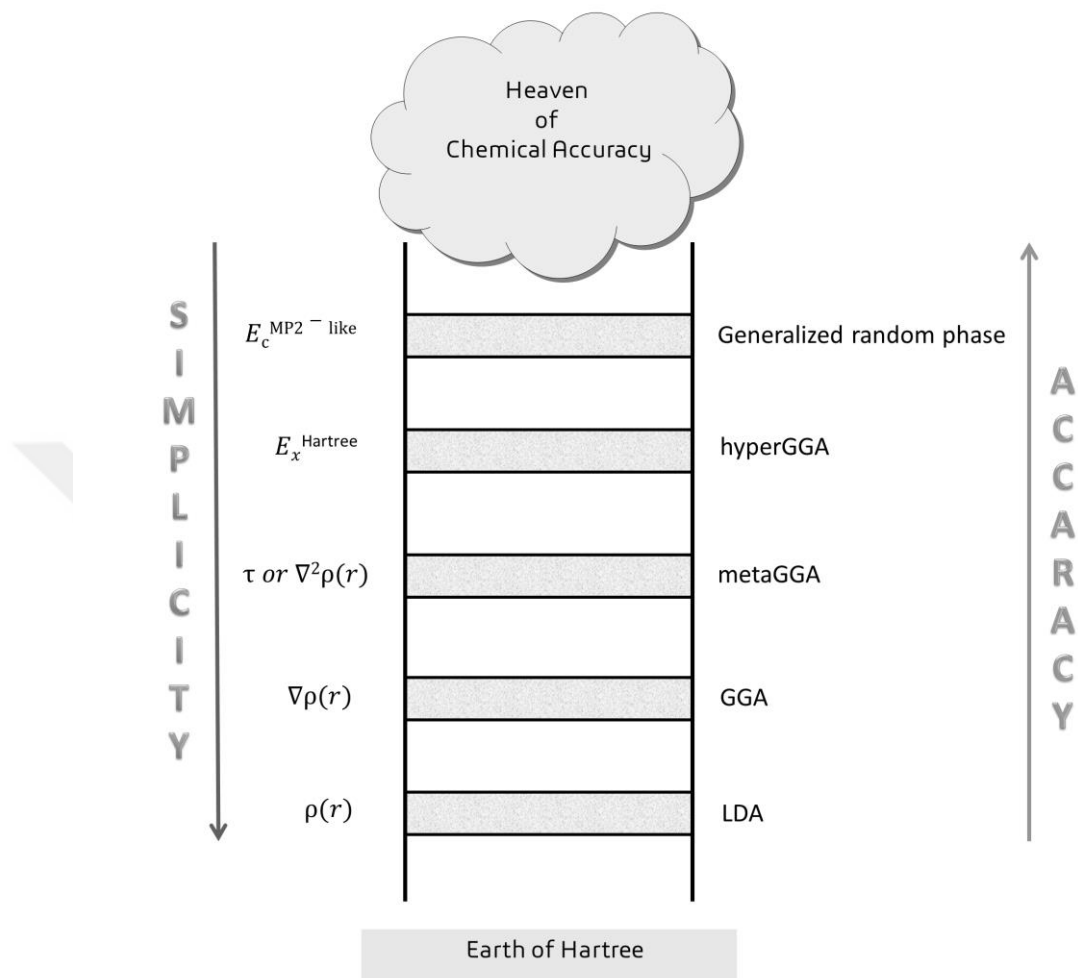


Figure 2.5 Perdeu's the Jacob's ladder analogy to classification of exchange-correlation functionals[93]

2.3.6.1 Local (Spin) Density Approximation

The local density approximation (LDA) and its extension to fermionic systems local spin density approximation (LSDA) are the oldest, easiest and the most popular examples of the exchange-correlation functionals. The concept behind this approximation is very simple: solids are usually considered to a homogenous electron gas, and LDA is based on this homogenous electron gas assumption. The exchange-correlation energy for a system is found by

integrating the exchange correlation energy density of an interacting homogenous electron gas at the density $\rho(r)$:

$$E_{xc}^{LDA} = \int dr e_{xc}(\rho(r))\rho(r) \quad (2.20)$$

Further, the exchange-correlation functional can be divided into exchange and correlation parts:

$$e_{xc}(\rho(r)) = e_x(\rho(r)) + e_c(\rho(r)) \quad (2.21)$$

The exchange part can easily be obtained from geometrical consideration:

$$e_x^{LDA} = -\frac{3}{4} \left(\frac{3}{\pi} \rho(r) \right)^{1/3} \quad (2.22)$$

However, there is no analytical expression for the correlation part e_c . The correlation part is fitted by means of quantum Monte Carlo simulations. LDA is generally valid approximation for nearly-free-electron metals. But for late transition metals with more localized electrons and where magnetism plays significant role, the results can be inconsistent.

2.3.6.2 Generalized-Gradient Approximation

In LDA, all system is assumed as homogenous. But, real systems are inhomogeneous with spatially varying electric fields, originating from nuclei and screening. Hence, the accuracy of the LDA can be enhanced by taking into account the density gradient. The GGA is described by,

$$E_{xc}^{GGA} = \int df(\rho(r), \nabla\rho(r)) \quad (2.23)$$

There are different types of GGA, each making a different choice for the function f . Among them, PBE[96] functional is used throughout this thesis due to its broad range performance compared to the others. According to the reports in the literature, GGA-PBE reasonably gives accurate results for MOFs. Although there are more accurate functionals, like hybrid functional, they are relatively new and not as commonly available for AIMD like PBE functional.

2.4 Molecular Dynamics

Molecular dynamics (MD) is a versatile and powerful computational technique to examine dynamical and structural properties of materials at the atomistic level. The two types of MD method are used in computer simulations studies, classical MD (CMD) and ab-initio MD (AIMD). Both methods have relatively some advantages and disadvantages.

We used Parrinello-Rahman MD algorithm since it appears to be very successful in reproducing experimentally observed phase transitions. In this part, after a very short introduction to the CMD and its limitation, the details of AIMD will be presented.

2.4.1 Classical Molecular Dynamics

Classical MD is a well-established technique to investigate the many-body condensed matter systems. The most challenging problem at the heart of any MD simulation is defining the interatomic potentials. In classical MD simulations, they are computed from “predefined potentials”, which have been derived from empirical data or accurate ab-initio electronic structure calculations. Even though overwhelming success in elaborating these potentials, their serious drawbacks were reported in the literature. The most prominent of these drawbacks/limitations can be summarized as follows:

- (i) Quantum Effects: Many important phenomena of modern physics and chemistry are non-classical. For example, the charge transfers during the phase transitions as a dynamic process involve with some quantum effects like changes in chemical bonding, the forming of some intermediate phases.
- (ii) Reliability of the Interatomic Potentials: The physical model of a simulated system is defined by the atomic force field. If the potential energy function does not fully mimic the forces experienced by the “real” atoms, the results of simulation will not be realistic. However, to speed up the evaluation of forces, potential must have simpler functional

form. The transferability and applicability of the potentials to other system are restricted.

2.4.1 Ab-initio Molecular Dynamics

Since many of aforementioned limitations can in principle be removed, ab-initio MD (AIMD) technique is attracting widespread interest in materials science, chemistry and physics. The basic idea underlying AIMD method is that the forces acting on the system can be calculated “on-the-fly” using Quantum Mechanics. For this approach Lagrange can be given:

$$L = T - V = \frac{1}{2} \sum_{i=1}^{3N} m_i v_i^2 - E[\psi(r_1, \dots, r_{3N})] \quad (2.24)$$

This Lagrangian suggests that calculations can be carried out consecutively. First, the ground state energy is calculated. And then, the position of nuclei is changed using an MD step. The new ground state energy is again calculated and so on. It is crucial to note that AIMD is a general approach that in principle can be used in cooperation with any electronic structure method.

2.4.1.1 Car-Parrinello Method

In 1985, R. Car and M. Parrinello[97] stepped the AIMD up. In their proposed algorithm by them, following the motion of nuclei and finding the electronic ground state given the nuclear positions are treated in a combined way with an extended Lagrange. The main idea in this concept is to describe equations of motion for both nuclei and electronic degrees of freedom that are simultaneously followed by MD. Their Lagrangian is given:

$$L = \frac{1}{2} \sum_{i=1}^{3N} m_i v_i^2 - E[\psi(r_1, \dots, r_{3N})] + \frac{1}{2} \sum_j 2\mu \int dr \left| \dot{\psi}_j(r) \right|^2 + L_{ortho} \quad (2.25)$$

While the first two terms are the same as in Eq 2.24, the last two terms are different, defining fictitious degree of freedoms. The third term introduces the kinetic energy of fictitious mass (μ), and the last term is necessary to keep the one-electron wave functions orthogonal. If the velocities associated with dynamics based on equation 2.25 are used to ascribe a temperature and scaled to

bring $T \rightarrow 0$, the equilibrium state of minimal E is achieved. This approach is called as Car-Parinello molecular dynamics (CPMD).[98]

2.4.1.2 Parrinello-Rahman Method

In the method of Parrinello and Rahman,[99] the volume of a simulation cell is treated as a dynamical variable. The volume and shape of the simulation cell can change under applied stress, thus the internal stress of the system can match the externally applied stress. In this study, the hydrostatic and uniaxial stresses on an unit cell was applied by using the Parrinello-Rahman algorithm.

The Parrinello-Rahman Lagrange for a simulation cell with lattice vectors a , b and c is given as:

$$L = \frac{1}{2} \sum m_i \dot{S}_i^t G \dot{S}_i - \sum_i \sum_{i>j} \varphi(r_{ij}) + \frac{1}{2} W \text{Tr}(\dot{h}^t \dot{h}) - P_{ext} \Omega \quad (2.26)$$

where h is the matrix formed by lattice vectors, Ω is the cell volume ($\Omega = \det h$), S_i is a position vector in fractional coordinates for atom i , $\varphi(r)$ is the pair potential, P_{ext} is the external hydrostatic pressure, h^t is the transpose of h matrix, W is the fictitious mass, and G is a metric tensor ($G = h^t h$). From the equation 2.26, the equations of motion are easily obtained:

$$\ddot{S} = m_i^{-1} \sum_{i \neq j} \chi(r_{ij})(S_i - S_j) - G^{-1} \dot{G} \dot{S}_i \quad (2.27)$$

$$W \ddot{h} = (\pi - P_{ext}) \sigma \quad (2.28)$$

where, using the dyadic notation, and writing $v_i = h \dot{S}_i$

$$\Omega \pi = \sum_i m_i v_i v_i + \sum_i \sum_{i>j} \chi(r_{ij})(r_i - r_j)(r_i - r_j) \quad (2.29)$$

If h is constant, namely MD cell is time dependent, $\dot{G} = 0$, and in this case, equation of motion becomes:

$$m_i \ddot{r}_i = \sum_{i \neq j} \frac{1}{r_{ij}} \frac{d\varphi}{dr_{ij}} r_{ij} \quad (2.30)$$

From equation 2.28, there is dynamic imbalance in the system due to the difference between externally applied stress and internally generated stress

tensor. So the equation 2.28 allows one to study such a kind of nonequilibrium phenomena. Also the same equation states that, fictitious mass W determines the relaxation time for recovery from an imbalance between the external pressure and internal stress.

From the Lagrangian, the corresponding Hamiltonian can be constructed. This Hamiltonian will define a constant of motion, because system is not subject to time dependent external forces. So, it is described by

$$H = \sum_i \frac{1}{2} m_i v_i^2 + \sum_i \sum_{j>i} \varphi(r_{ij}) + \frac{1}{2} W \text{Tr}(\dot{h} \dot{h}) + P_{ext} \Omega \quad (2.31)$$

In equilibrium conditions, at temperature T , W compensates the $9/2k_B T$ and other kinetic terms the $3N/2k_B T$. Therefore, the constant of motion H is nothing, but the enthalpy:

$$H = E + P_{ext} \Omega \quad (2.32)$$

where

$$E = \sum_i \frac{1}{2} m_i v_i^2 + \sum_i \sum_{j>i} \varphi(r_{ij}) \quad (2.33)$$

At the end, the equation of motions based Lagrangian defined in the equation 2.26 generates an NPH ensemble.

2.5 Simulation Conditions and Structural Analysis

In this part, I will present a general perspective on used simulation conditions throughout this dissertation. Firstly, I will introduce AIMD computational code SIESTA and parameterization of AIMD simulation. And then I will finish this chapter with giving an brief information on the structural analysis methods in this work.

2.5.1 SIESTA

SIESTA AIMD code (version 3.2 and 4.1) was used in this thesis to examine the pressure-induced phase transitions in various MOFs. SIESTA is abbreviation of Spanish Initiative for Electronic Simulations with Thousand Atoms, which provides a way to carry out electronic structure and AIMD calculations.[100] It employs linear combinations of atomic orbitals (LCAO) as basis sets unlike many DFT computational tools based on plane wave. Main advantage of SIESTA is that order-N-scaling algorithm, which state that the CPU time used by the calculations scale linearly with the number of atoms in the simulation cell. Hence, it can perform not only very fast simulations using minimal basis sets but also give very accurate results by using complete zeta and polarized orbitals. Due to the aforementioned properties, SIESTA is very suitable tool for simulation of large systems (>200 atoms), so it may also be the best suited code for MOFs with many atoms in their unit cell.

2.5.2 Pseudopotentials

SIESTA employs pseudopotentials to introduce the electron-ion interaction, and they are “norm conserving” kind. A solid system contains typically two types of electrons: (i) core electrons are described by localized wave-functions and tightly bound to the nuclei and so they are (assumed) chemically inert, (ii) valance electrons are almost delocalized in the solid (electron gas in metals), responsible for the formation of atomic bonds and having dominant impact on the properties of materials. By definition the core electrons screen the nuclear potential. In a pseudopotential approximation, core electrons are excluded from calculations, and in order to define their effects, an effective potential or pseudopotential is constructed. Therefore, in the Schrödinger equation, there is a modified effective potential term instead of normal Coulombic potential term for core electrons. “Norm-conserving” term means that the functional form (the norm) of each pseudo-wave-function be identical to its corresponding all-electron wave-function.

Throughout this study, to define ion-electron interaction, norm-conserving Troullier-Martins pseudopotentials were used. [101]

2.5.3 Basis Set

SIESTA uses numerical atomic orbitals (NAO), which are derived from numerical solution of the Kohn-Sham equations of isolated pseudo atom using Numerov method, as basis set. The basis functions are described by the changeable radial component and well-defined spherical harmonic for given orbital. The radial part of the orbital is constructed from one (single- ζ), two (double- ζ) or more (triple- ζ ...) radial functions. In comparison to other basis sets (such as plane wave and grids), NAOs can be designed with any shape without extra computational cost. Also, to eliminate expensive long-range interactions, they can be simply localized, thus providing better scaling. Furthermore, additional angular momenta should be described over artificial polarization functions because there is no real spherical symmetry in the solid. In this study, valance states of all atoms are described by using extensive double- ζ polarized (DZP) basis sets.

2.5.4 Periodic Boundary Conditions

In practice, the number of atoms in a simulated system is limited by the availability of computational power and memory. However, the realistic models/structures generally contain about from one thousands to several thousand atoms or molecules. Due to the usage of their certain fraction in a simulation box, homogeneity and representativity conditions may not always be fulfilled. In order to eliminate the undesired effects of boundaries, periodic boundary conditions (PBC) are usually used. The figure 2.6 represents the basic concept of PBC. The shaded square box shows the system we are simulating, whereas the dotted boxes are the periodic copies in every detail, even with the velocities of atoms. This arrangement is imagined to pave the whole space. Once an atom leaves from the simulation cell, it's replaced by another with

exactly same velocity, getting into the cell from the opposite cell face. Therefore, the number of atoms in the simulation cell remains the same.

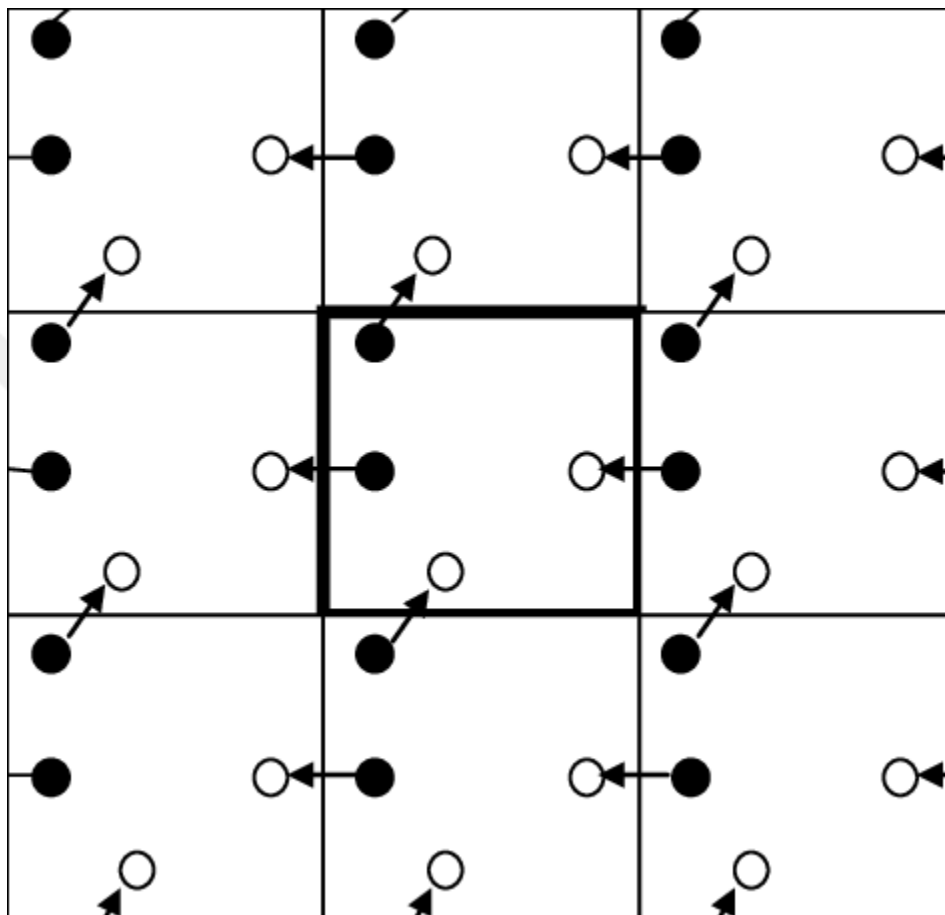


Figure 2.6 Schematic description of periodic boundary conditions in 2D.[102]

2.5.5 Geometry Optimization

For all simulations in this study, the experimentally derived starting geometries of the MOFs were taken from The Cambridge Crystallographic Data Center (CCDC). The geometry optimization was performed by a conjugate gradient (CG) variable cell method based on the independent variation of both atomic positions and unit cell parameters. Once the force tolerance criterion of 0.001 eV/\AA was achieved, the structure was considered to be optimized. The Parrinello-Rahman method is also used for the relaxation of the systems in cases where convergence or the force criterion could not be achieved by using CG.

2.5.6 Equation of State

In order to explore the behavior of a solid under compression or tension the equation of state (EOS), pressure-volume or energy-volume relations, is usually used. The simplest form of EOS for a solid under isothermal conditions is the bulk modulus (K) that is a measure of compressibility of a solid under uniform pressure. The equilibrium bulk modulus K_0 of a solid and dimensionless parameter K_0' , the first derivative of K with respect the pressure, is defined as:

$$K_0 = -V \left(\frac{\partial P}{\partial V} \right)_T \quad K_0' = \left(\frac{\partial K_0}{\partial P} \right)_T \quad (2.34)$$

Also, we can express pressure (P) as a function of volume:

$$P(V) = - \left(\frac{\partial E}{\partial V} \right)_S \quad (2.35)$$

By using equation 2.35, we can rearrange bulk modulus:

$$K(V) = V \left(\frac{\partial^2 E}{\partial V^2} \right)_{T,S} \quad (2.36)$$

In ab-initio calculations, we mostly perform our calculations at 0 K. Therefore, The Gibbs free energy becomes enthalpy at zero K, which expressed as:

$$H(V) = E(V) + P(V) \cdot V \quad (2.37)$$

The third-order Birch-Murnaghan EOS, reported in 1947 by Francis Birch, is based on finite-strain theory and establishes a relationship between the volume of a solid and the pressure applied. The equation is given:

$$E(V) = E_0 + \frac{9V_0 K_0}{16} \left\{ \left[\left(\frac{V_0}{V} \right)^{\frac{2}{3}} - 1 \right]^3 K_0' + \left[\left(\frac{V_0}{V} \right)^{\frac{2}{3}} - 1 \right]^2 \left[6 - 4 \left(\frac{V_0}{V} \right)^{\frac{2}{3}} \right] \right\} \quad (2.38)$$

Again by using equation 2.35 we can derive P(V) third order Birch-Murnaghan EOS,

$$P(V) = \frac{3K_0}{2} \left[\left(\frac{V_0}{V} \right)^{\frac{7}{3}} - \left(\frac{V_0}{V} \right)^{\frac{5}{3}} \right] \left\{ 1 + \frac{3}{4} (K_0' - 4) \left[\left(\frac{V_0}{V} \right)^{\frac{2}{3}} - 1 \right] \right\} \quad (2.39)$$

Once the pressure-volume values are obtained for a system, the enthalpy and bulk modulus can be calculated by fitting them to third-order Birch-Murnaghan EOS.

2.5.7 Pair Distribution Function

The pair distribution function (PDF), which is also called radial distribution function (RDF) or pair correlation function (PCF), gives the probability of finding an atom at a distance “r” from a given atom. By dividing the physical system volume into shells, the number of atoms $dn(r)$ at a distance between r and $r+dr$ can be calculated:

$$dn(r) = \frac{N}{V} g(r) 4\pi r^2 dr \quad (2.40)$$

where N , V and $g(r)$ refer to the total numbers of atoms, the system volume and the pair distribution function, respectively. In this formulation, the volume of the shell with dr thickness is approximately:

$$V_{shell} = \frac{4}{3} \pi (r + dr)^3 - \frac{4}{3} \pi r^3 \approx 4\pi r^2 dr \quad (2.41)$$

The pair distribution function for two species $g_{\alpha\beta}(r)$ is given by

$$g_{\alpha\beta}(r) = \frac{dn_{\alpha\beta}(r)}{4\pi r^2 \rho_{\alpha}} \quad \text{with} \quad \rho_{\alpha} = \frac{N}{N_{\alpha}} = \frac{V}{N \times c_{\alpha}} \quad (2.42)$$

where c_{α} denotes the concentration of atomic species α in the system.

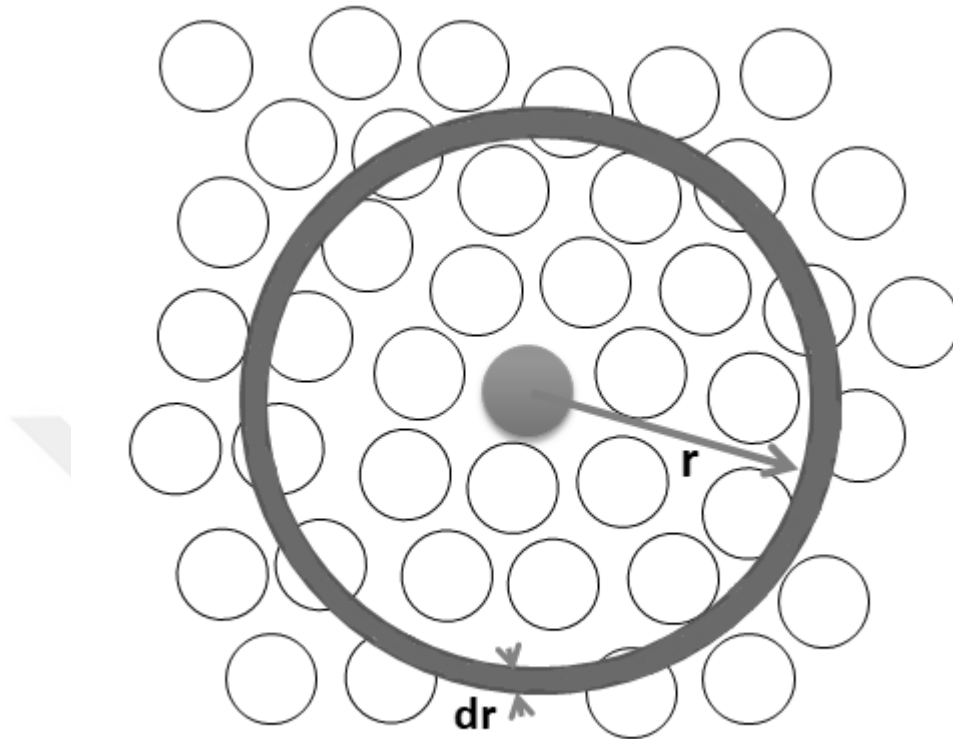


Figure 2.7 Space discretization for the evaluation of the radial distribution function.

2.5.8 Bond Properties

Distribution of bond lengths for the first coordination shell, bond and dihedral angles distributions, proportion of tetrahedral units in the simulation cell and average first coordination numbers were calculated for all structures by using an open source analysis program I.S.A.A.C.S.[103]

2.5.9 Electronic Properties

The electronic density of states (EDOS) is used to describe the electronic properties or/and electronic structures of both crystal and amorphous solids. EDOS is defined as the number of single-particle states in a given energy range and can be formulated:

$$\rho_{EDOS}(E) = \frac{1}{N_f} \sum_{i=1}^{N_f} \delta(E - \varepsilon_i) \quad (2.43)$$

where N_f is the total number of occupied electronic states and ε_i is the energy eigenvalue of the electronic Hamiltonian. The determination of band gap and Fermi level, information on valance and conduction bands, and also understanding electron conduction mechanism in the solid are provided by the EDOS.



Chapter 3

Pressure-Induced Amorphization of MOF-5

The work presented in this chapter is published in **M.Erkartal**, M.Durandurdu, ChemistrySelect **2018**, 3, 8056–8063.

3.1 Introduction

Amongst numerous MOFs, MOF-5, first synthesized by Yaghi and co-workers,[104] is one of the most well-known materials. It has Zn_4O clusters coordinated by benzene-1,4,-dicarboxylic acid (BDC) linkers to form a cubic 3D framework.[105] Up to now, considerable efforts have been devoted to investigate its gas storage properties both experimentally and theoretically due to its high specific surface area, 4700 m^2/g . In recent years there have been growing theoretical interests to probe its electronic,[106-108] optical,[109, 110] mechanical[111-113] and spectroscopic[109, 111] properties. Furthermore, there have been few new studies that discuss the potential usage of MOF-5 as quantum dots,[114] photocatalysts,[115] semiconductor materials,[116] supercapacitor components,[117] and fuel cell electrodes.[118] To the best of our knowledge, there are two reports, showing the mechanical amorphization of MOF-5, in the literature. In the first study, Hu et al. experimentally revealed a pressure-induced amorphization in a polycrystalline MOF-5 sample at room temperature and 3.5 MPa. They pointed out that the destruction of carboxylate groups could be a main reason behind the amorphization.[77] In the second one, Moggach et al.[82] showed the complete amorphization of a single crystal MOF-5 sample above 3.2 GPa in a diamond anvil cell (DAC) experiment using diethyl formamide (DEF) as a pressure transmitting medium. The authors underlined that the amorphization of framework might be related to Zn-O bonds. [82]

In this report, inspired by both previous works, we investigated the PIA in MOF-5 by using a constant pressure ab initio technique to have an atomistic level description of this phase transition. During the simulations, the crystalline MOF-5 phase was subjected to a gradually increased hydrostatic pressure, and the collapsing of the pores was observed at 2 GPa, which resulted in an irreversible first-order phase transition in the framework. Further, we performed the Bader charge analysis to explore the charge transfers among atoms during this transition and investigated the electronic structure of both crystalline and amorphous states. Our calculations show that amorphization is due to the local structural distortions without any breaking bonds in the framework, and a charge transfer occurs between Zr-O and C-H.

3.2 Methodology

The SIESTA ab initio code, based on the density functional theory (DFT), has been used to perform the molecular dynamics (MD) simulations.[100] The Perdew-Burke-Ernzerhof (PBE) generalized gradient approximation (GGA) for the exchange-correlation[96] and Troulier-Martins pseudopotentials were used to define the ion-electron interactions.[101] The double- ζ polarized orbitals were preferred for the calculations. Real space integration was carried out on a ordered grid corresponding to a plane-wave cut off of 200 Ry. The single-crystal derived conventional cell, which consists of 424 atoms, was used as a starting geometry. The optimized structure was achieved by conjugate gradient (CG) variable cell method with 0.01 eV/Å force tolerance. Due to the relatively higher number of atoms in the simulation boxes, only Γ -point sampling of k-mesh was used. Hydrostatic pressure was applied under isoenthalpic-isobaric (NPH) simulations via the the Parinello-Rahman method.[99] The Henkelman code was used for the Bader charge analysis.[119] The VESTA program[120] for visualization of the obtained structures and ISAACS code[103] for further structural analysis were used. A period of 5000 MD steps was applied to have equilibrium state at each pressure step. Also, additional 5000 MD steps were run at and before the phase transitions to guarantee that the system reached to the

true equilibrium volume. The time step for each MD simulation was 1 femtosecond (fs). Pressure was applied to the framework as follows: The optimized zero-kelvin structure was used as starting geometry and pressure (P) was increased (or decreased) with a ΔP pressure step. At each new pressure $P + \Delta P$, the pressure was applied to the structure obtained from the previous pressure (P). The ΔP was 1 GPa.

3.3 Results and Discussion

The porous framework structure of MOF-5 formed by linking Zn_4O nodes with BDC ligands has a cubic Fm3m symmetry (no. 225) with the lattice parameter of $a_0 = 25.866 \text{ \AA}$. Prior to the application of pressure, experimentally obtained X-ray diffraction structure[104] was optimized via a CG method with 0.01 eV/\AA force tolerance at zero pressure. The equilibrium lattice parameter and structural data obtained are in good agreement with the experimentally elucidated structure of MOF-5 as seen from Table 3.1. Yet, a small difference between the experimental and calculated lattice parameter originates from the fact that the GGA-PBE approach generally overestimates the lattice parameters. [121]

Property	PBE-GGA	Exp.[104]	PBE-GGA[109]	LDA[111]
Crystal System	Cubic	Cubic	Cubic	Cubic
Space Group	$Fm\bar{3}m$	$Fm\bar{3}m$	$Fm\bar{3}m$	$Fm\bar{3}m$
a₀ (Å)	26.236	25.885	26.044	25.888
V₀ (Å³)	18060	17344	17665	17350
ρ (g/cm³)	0.57	0.59	-	0.589
Atom Type	Atomic Positions (x,y,z)		Atomic Positions (x,y,z)[122]	
Zn₁ (32f)	(0.2937, 0.2937, 0.2937)		(0.2935, 0.2935, 0.2935)	
O₁ (8c)	(0.2500, 0.2500, 0.2500)		(0.2500, 0.2500, 0.2500)	
O₂ (96k)	(0.2187, 0.7810, 0.3668)		(0.2194, 0.7806, 0.3661)	
C₁ (48g)	(0.2500, 0.8853, 0.2500)		(0.2500, 0.8885, 0.2500)	
C₂ (48g)	(0.2500, 0.9467, 0.2500)		(0.2500, 0.9461, 0.2500)	
C₃ (96k)	(0.7170, 0.2826, 0.4734)		(0.7175, 0.2825, 0.4734)	
H₃ (96k)	(0.6916, 0.3085, 0.4528)		(0.6956, 0.3044, 0.4552)	

Table 3.1 Optimized structural parameters for MOF-5

After the relaxation process, the gradually increased hydrostatic pressure was applied to the equilibrated structure and the change in the volume and structure was monitored. The Figure 3.1 presents the pressure dependence of conventional cell volume and the evolution of a subunit consisting of BDC and Zn linkage nodes. A sharp decrease in the volume (68 %) indicates a first-order phase transition at 2 GPa. Beyond this pressure, there is an insignificant change in the volume. Upon decompression from 4 GPa, the structure only recovers a small percentage (~6 %) of its original volume, indicating the irreversible nature of this transition.

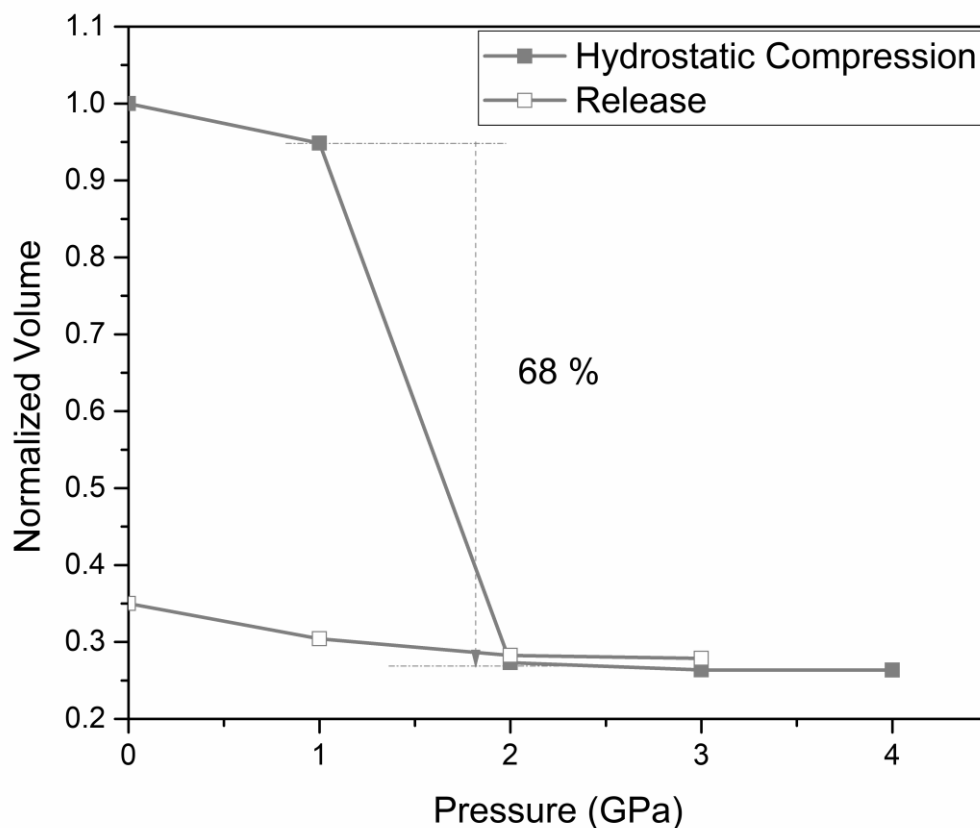


Figure 3.1 Pressure dependence of conventional cell volume.

In order to identify the structure at this pressure and compare it with the MOF-5 crystal at ambient pressure, we first probe their total and partial pair distribution functions (PDFs), which can provide detailed information on their short-range order (SRO). Total and partial PDFs for both structures are given Figure 3.2. The results disclose quite different PDFs for them as expected, specifically beyond 4 Å. The PDFs of MOF-5 show long-range correlations (have a pattern with discontinuous and sharp peaks along the given range) though PDFs of the structure at 2 GPa contain relatively less intense peaks up to 4 Å and present typical characteristics of an amorphous state such that it has a well-defined short-range order and the lack of long-range correlations. This observation suggests the occurrence of a pressure-induced amorphization at this pressure in the simulation.

Our coordination number analysis using the first minimum of the PDFs suggests that the coordination number of each species does not change during the phase

transformation. This finding does not corroborate the experimental findings and suggestions. Obviously, the local structural distortions, especially in the vicinity of Zn_4O nodes, diminish the long-range order, namely its crystallinity (Figure 3.3).[83, 123] Our structural analysis shows that a new reconstruction mechanism without any bond breaking in the framework is possible due to the free rotation ability of the C-C single bonds on the both sides of the ligands.

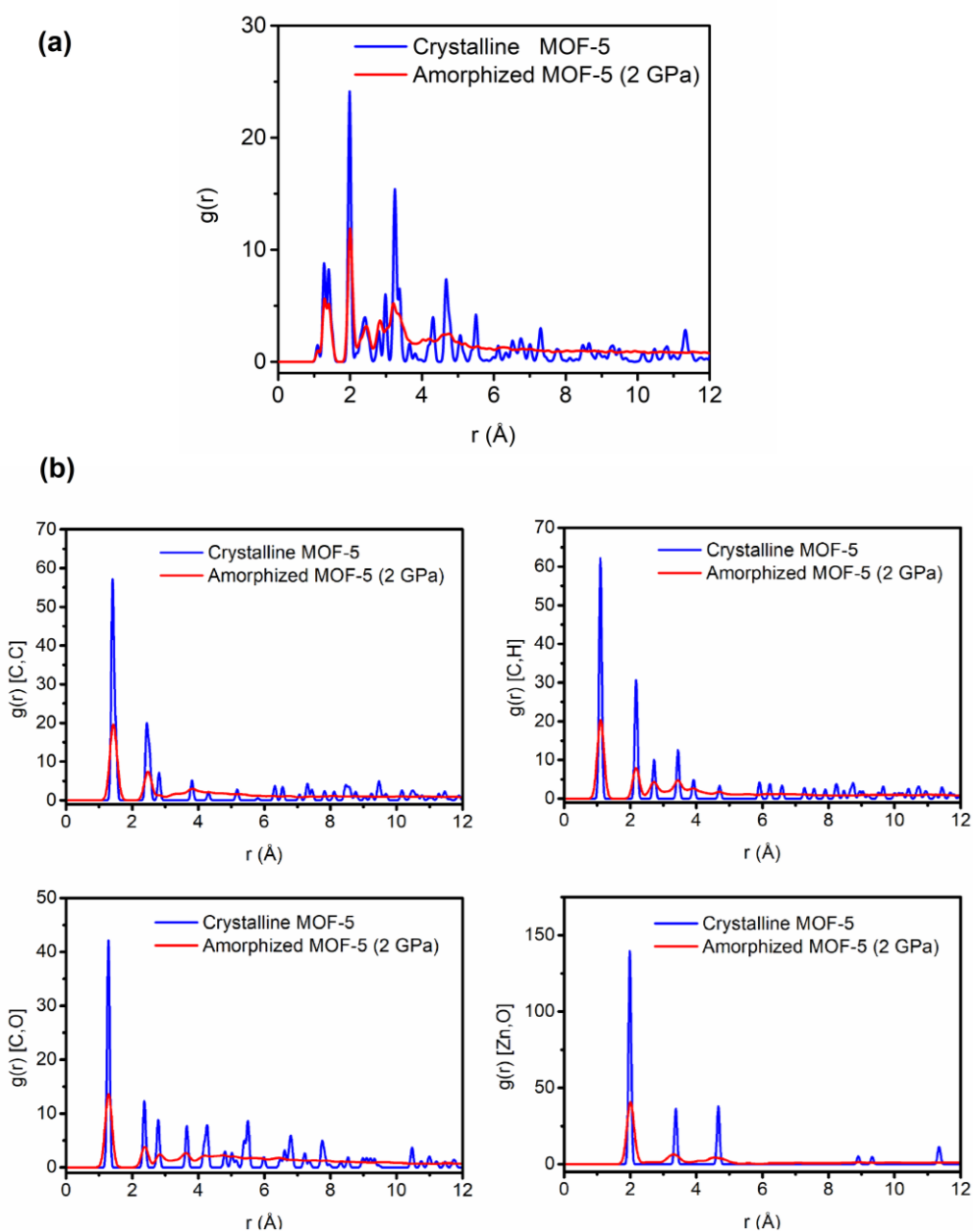


Figure 3.2 (a) Total and (b) partial pair-distribution functions (PDFs) for the crystalline MOF-5 phase and its amorphized form at 2GPa.

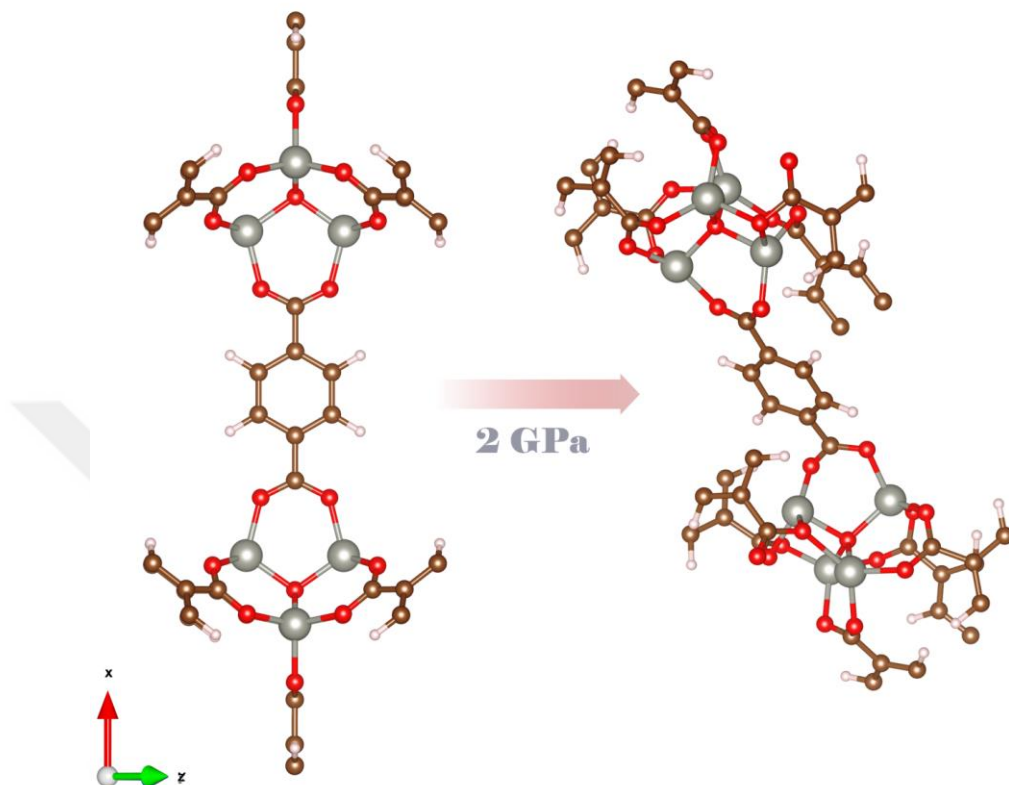


Figure 3.3 Structural evolution of extracted subunit from conventional cell.

Bond	MOF-5 (GGA-PBE) (Å)	α -MOF-5 (2GPa) (Å)	Exp. (Å)[122]	MOF-5
C ₁ -C ₂	1.412	1.407	1.383	
C ₂ -C ₃	1.498	1.486	1.500	
C ₃ -O ₁	1.284	1.279	1.262	
O ₁ -Zn	1.988	2.008	1.940	
O ₂ -Zn	1.988	1.967	1.938	
C-H	1.10	1.10	0.97	

Table 3.2 Calculated bond lengths for optimized structure and α -MOF-5

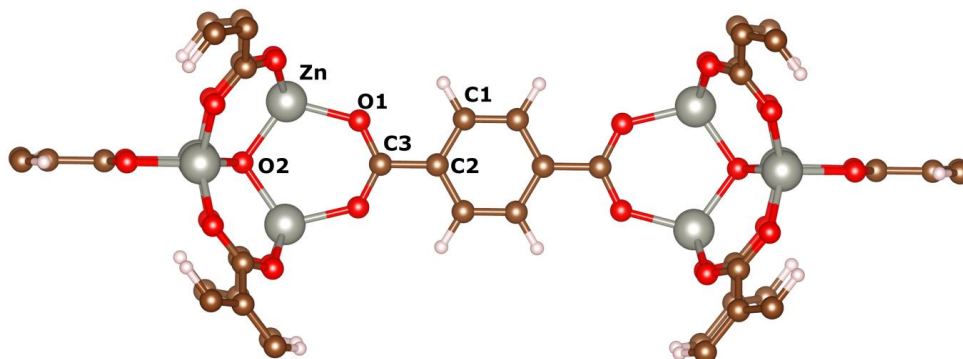


Figure 3.4 Extracted subunit from the conventional cell of MOF-5. Zinc, oxygen, carbon, and hydrogen are presented in grey, red, brown and white, respectively.

The determined bond lengths from the chosen subunit depicted in Figure 3.4 for MOF-5 and amorphous MOF-5 along with the experimental values are listed in Table 2. According to the results obtained, the bond lengths slightly change during the phase transition. For example, for the crystalline MOF-5 at zero pressure, the C3-O1, O1-Zn, O2-Zn bond lengths are 1.284, 1.988, and 1.988 Å, respectively. For the amorphous form at 2 GPa, the C3-O1, O1-Zn, O2-Zn bond lengths alter to 1.279, 2.008 and 1.967 Å, correspondingly. Furthermore, in order to investigate the structural deformation in details, we plot the bond angle distribution functions of both structures. From the histograms as shown in Figure 3.5, we can see that the pressure causes significant alterations on the bond angles. For instance, the O-Zn-O angles are at 106° and 110° for MOF-5 and range from 89° to 140° for the amorphous state. Similarly, while Zn-O-Zn angle is located at 131° for the crystalline structure, it ranges from 85° to 130° in the amorphous form.

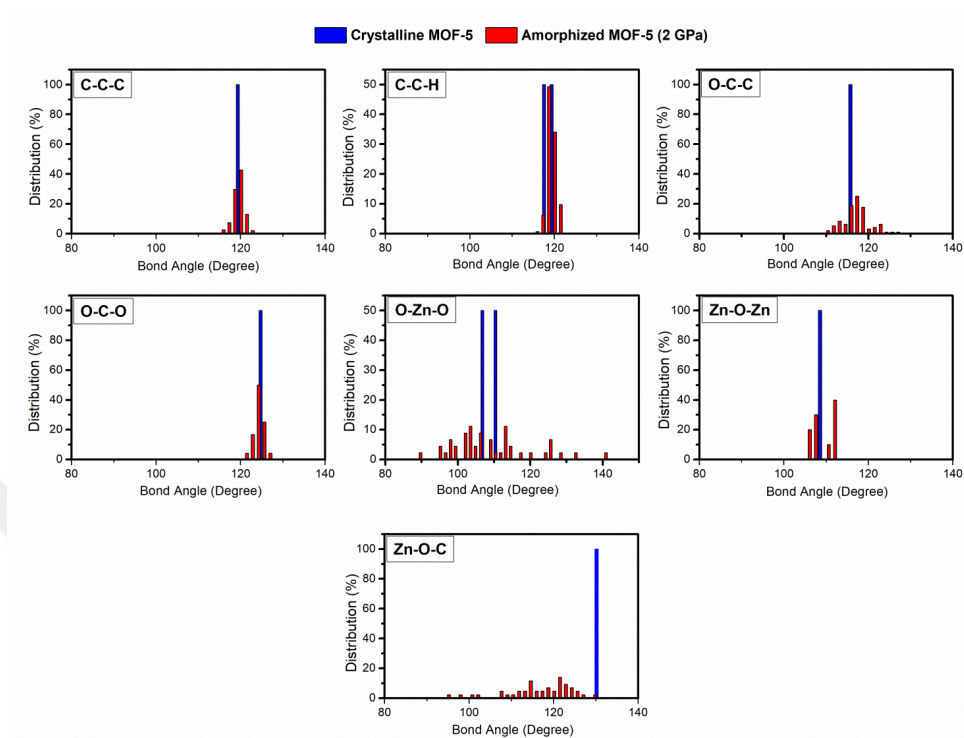


Figure 3.5 Bond angles distributions for the crystalline MOF-5 and α -MOF-5 phases.

The calculated total electronic density of states (TDOS) and partial density of states (PDOS) at different pressures are shown in Figure 3.6. The estimated GGA band gap value for MOF-5 is 2.5 eV, indicating that this structure has a semiconducting property. As might have been expected, this value is much lower than experimentally obtained band gap energy of 3.4-4.0 eV for MOF-5[124, 125] since DFT-GGA methods generally yield a lower band gap due to the ground-state formalism of DFT.[121] The overall electronic properties of MOF-5 are governed by both inorganic Zn_4O nodes and organic BDC linker. In this context, the metallic Zn_4O nodes give the structure a wide band gap property.[124] The delocalized electrons in the BDC may seem to improve the conductivity of the structure because the conduction is interrupted at insulating Zn_4O nodes.[111] PDOSs provide further perspective how both components contribute the formation of valance and conduction bands. It is apparent from Figure 6 that the bottom of the conduction band is determined by the unoccupied s and p states of the C,O and Zn atoms, while the top of the valance band is

predominantly formed by the hybridization of the 2p-states of C and O with Zn-3d states.

Also as can be clearly seen from the graph, for the structure at 1 GPa, no significant difference was found in the electronic structures. This might be predictable because there is no notable structural change in the framework at this pressure and its crystallinity is preserved. On the other hand, accompanied by the phase transformation, interesting and remarkable changes are observed in the electronic structure. The band gap drops to 1.5 eV at 2 GPa.

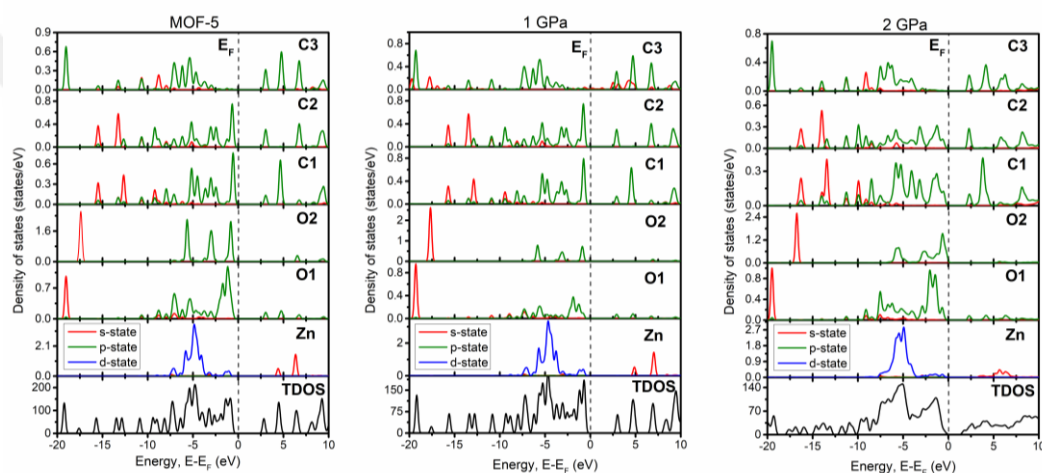


Figure 3.6 Calculated total density of states (TDOS) and partial density of states (PDOS) for MOF-5, the structure at 1GPa and α -MOF-5.

The Bader charge analysis is an unbiased method to determine changes in atomic charges and volumes. In this technique, a complex chemical system – such as a molecule- can be partitioned into single atomic (Bader) volumes. Each Bader volume has a single charge density maximum. Also, these volumes are separated from each other by surfaces where the charge density is a minimum normal to the surface. Thus, there is only one Bader volume for each atom and one charge density maximum at each atomic center. So, the Bader charge analysis is a well-defined, precise and useful method, and also more robust than wavefunction-based population analysis (for example, Mulliken population analysis).[119, 126, 127] Furthermore, the Bader charge analysis can be used for the investigation of phase-transitions.[128, 129] Here, the Bader charge

analysis was employed in order to explore roles of atomic charges and volumes in the crystalline-to-amorphous phase transition in MOF-5. The results are summarized in Figure 3.7a – 3.7b. Both the Bader charge and volume plots are parallel to the pressure-volume curve of MOF-5. At ambient pressure, due to large electronegativity difference between Zn ($\chi=1.65$) – O ($\chi=3.44$) and C ($\chi=2.55$) – O ($\chi=3.44$) atom pairs, each O1 and O2 atoms gain ~ 1.08 and $\sim 1.25e$ from each C3 and Zn atoms, respectively. The calculated the Bader volume for O1 atom (113 \AA^3) and O2 atom (102 \AA^3) are about much higher than C3 atom (42 \AA^3) and Zn atom (81 \AA^3), and this also confirms the charge transfers between referred atoms. During the phase transition at 1-2 GPa, a significant charge transfer was observed between Zn-O1, O1-C3 and terminal H atoms. At this pressure range, the Bader charge results show that about $0.13e$ moved from Zn and O1 atoms to C3 and H* atoms. Beyond the phase transition range, at 2-4 GPa, there is no significant charge transfer between the constituents' atoms. Moreover, the Bader analysis of individual atoms in the simulated cell shows that in the crystalline phase the Bader charges and volumes differences for the same atoms are very small, while in the amorphous phase there are significant fluctuations in charges and volumes. This is probably due the lack of a long-range order but almost the same short-range order around the same kind atoms.

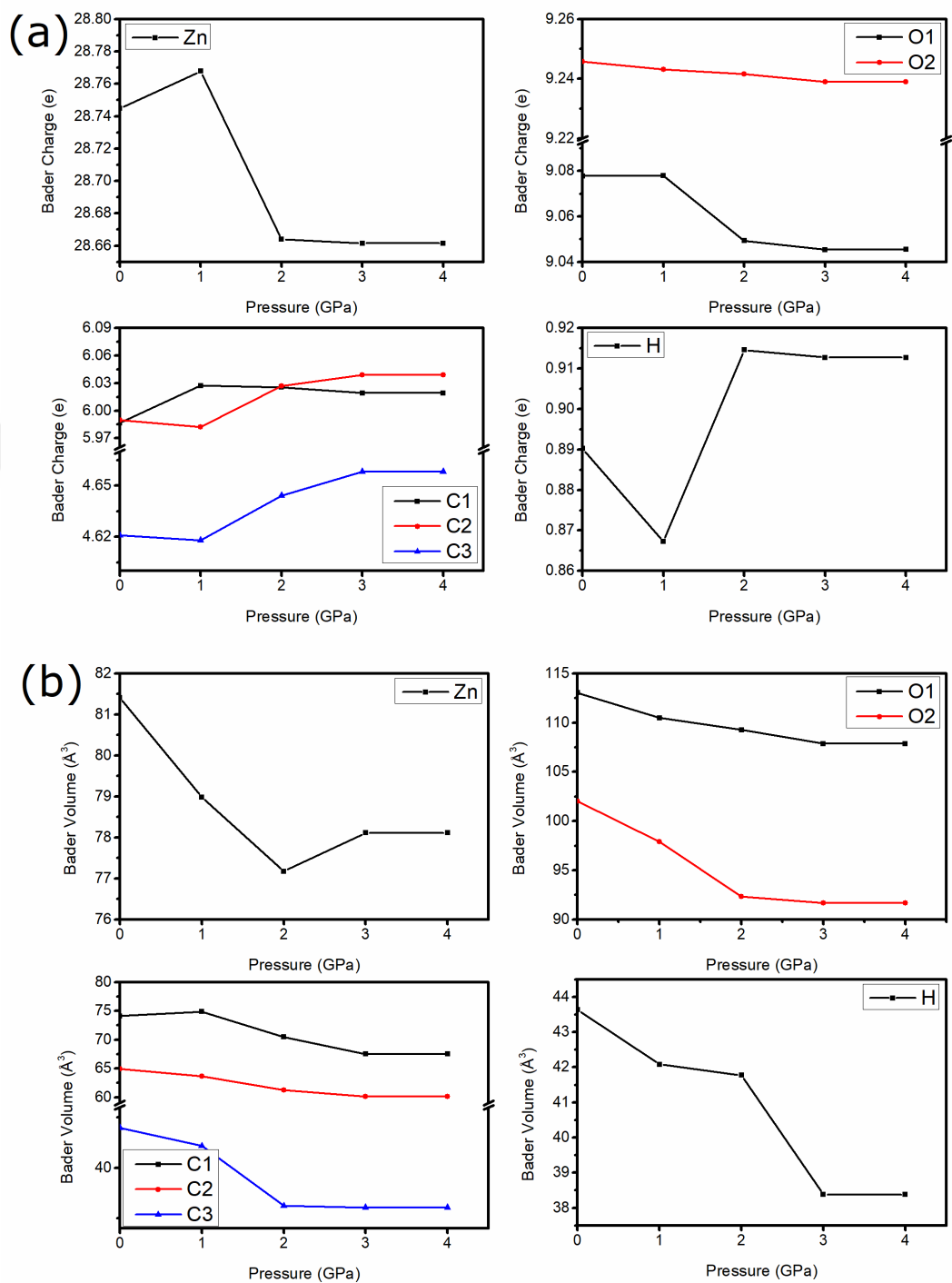


Figure 3.7 (a) Bader atomic charges (b) Bader atomic volumes

In general, the analysis of the coordination number, bond lengths, and angles expose that the crystalline-to-amorphous phase transition is a result of local distortions i.e. bond bending in the framework and does not involve any new

bond formation or breaking. It would appear that the structural changes mainly act on the Zn_4O nodes and coordination sites. These findings are in contradiction with Hu et al.'s report, where they claimed that pressure-induced amorphization occurs via the destroying (bond breakage) some carboxylate groups. Additionally, their amorphization pressure (3.5 MPa) is significantly lower than what we found in the simulation (2 GPa). The difference between the simulation conditions and experimental conditions is probably responsible for this inconsistency. In our study, there are no factors, such as surface effects due to the use of periodic boundary conditions and structural defects that can significantly influence phase transitions in the simulated framework. On the other hand, Hu et al.[77] reported the amorphization of a polycrystalline pellet MOF-5 sample, including crystal-crystal interaction, surface and boundary defects, and uniaxial nature of applied pressure. In a different work, Moggach et al. [82] testified the complete amorphization of a single crystal MOF-5 sample at 3.2 GPa in a DAC experiment in which the diethyl formamide (DEF) was used as a pressure-transmitting medium (PTM). They pointed out that the squeezing of PTM molecules into pores leads to delaying the onset of amorphization of framework. This feature could well be responsible for the difference in amorphization pressures between the simulation and experiment. Moggach et al.[82] also highlighted that the amorphization of MOF-5 was governed by change in Zn-O bonds. According to our bond length calculations, both Zn-O1 bonds (to the carboxyl oxygen atom) and Zn-O2 bonds (to the μ_4 -oxygen atom) moderately change during the phase transition. The Bader charge analysis further shows the charge transfers between Zn, O and C (to the carboxyl carbon atom) atoms, and provides insight about the alterations in these bond lengths through the crystalline-to-amorphous phase transition. Importantly, the amorphization of framework leads to a drastic narrowing in band gap energy. Therefore, pressurizing or pressure-induced amorphization can be used in band-gap engineering of MOFs.

In the literature, pressure-induced transitions (PIT) of MOFs are commonly referred as adsorption-induced transitions (AIPs). Although AIPs are very useful

to describe the transitions in gas adsorption applications, it is insufficient to directly determine the mechanical behavior of frameworks. Namely, once the pores of the MOF are filled with adsorbate molecules, the framework turns into more resilient structure, which is considerably different than porous structure. Furthermore, the adsorbent-adsorbate interactions may affect the phase transition characteristics. Similarly, the DAC experiments in the existence of the PTM are also inadequate to directly determine the mechanical properties of MOFs due to the strong framework-PTM interactions. The in situ TEM compression test proposed by Suslick[85] seems to be a reliable approach to determining the mechanical properties and amorphization pressure of single crystal MOFs. However, due to the requirement of equipment infrastructures, it is unlikely that these experiments are widely available for now. On the other hand, ab initio simulations allow the modeling of framework under desired pressure (isotropic, uniaxial, etc.) and taking into account quantum mechanical phenomena (charge transfer, bonding, etc.), as well as it is easily accessible and provides reproducible simulations.

3.4 Conclusion

In conclusion, this study represents an investigation of pressure-induced amorphization in MOF-5 by using an ab initio technique. We have successfully observed an irreversible crystal-to-amorphous phase transition at 2 GPa and propose that the origin of phase transition is due to the local distortions through the framework, and does not involve any bond breaking and/or formation. Furthermore, the results show that the electronic properties of the crystalline MOF-5 phase are considerably different than the amorphous phase. We believe that that our results may improve the knowledge about pressure-induced amorphization in MOFs.

Chapter 4

Pressure-induced amorphization, mechanical and electronic properties of zeolitic imidazolate framework (ZIF-8)

The work presented in this chapter is published in **M.Erkartal**, M.Durandurdu, Materials Chemistry and Physics 240 (2020) 122222.

4.1 Introduction

Zeolitic imidazolate frameworks (ZIFs), a sub-class of metal-organic frameworks (MOFs), are currently attracting increasing interest by reason of their relatively high chemical and thermal properties.[130] They also offer promising potentials for gas storage,[131-133] catalysis[134-136] and electrochemical[137-139] applications. They possess zeolite topologies, wherein each tetrahedral metal nodes ($M = \text{Zn(II)}$ or Co(II)) coordinates to imidazolate-based linkers ($\text{Im}^- = \text{C}_3\text{H}_3\text{N}_2^-$) to form $(M(\text{Im})_2)$ neutral open framework structure.[131, 140] Specifically, the M-Im-M coordination linkage in ZIFs subtends an angle of around 145° at Im ring center, equivalent to the Si-O-Al angle in aluminosilicate zeolites.[70, 131] ZIF-8 ($\text{C}_8\text{H}_{10}\text{N}_4\text{Zn}$), zinc tetrahedral bridged 2-methylimidazolate (mim), has a high symmetry sodalite (SOD) topology and crystallizes in the cubic $I\bar{4}3m$ space group ($a=16.992 \text{ \AA}$).[21] The pores with a diameter around 12 \AA connected by 3.5 \AA diameter six-ring apertures with the 4-ring yield a large pore volume, $\sim 2400 \text{ \AA}^3$. [80]

Pressure-induced transition (PIT) investigations on MOFs are generally categorized into two groups in the literature: adsorption-induced transitions (AIP), and mechanical-stress induced transitions (MSIT).[19, 141] AIP studies have mainly focused on clarifying the relationship between structural distortions and adsorbent (framework) –adsorbate (e.g. N₂) interactions during the adsorption process.[142-145] The common technique for monitoring phase transitions in the MOFs is the diamond anvil cell (DAC) experiment, in which the frameworks are exposed to a hydrostatic pressure by means of pressure-transmitting medium (PTM).[73, 80] However, because of the pores being filled with PTM molecules, the framework changes to a more resilient structure, which causes a delay in amorphization pressure.[81] In addition, the results may be controversial due to framework-PTM molecules interactions and changes in the physical properties of the carrier fluid under high pressure.[85] So far, in situ TEM compression method was proposed to investigate the direct amorphization process of a single crystal MOF and its mechanical properties.[85] However, it is improbable that these experiments are widely available for now because of the equipment infrastructure required.

As a promising engineering material family, it is vital to determinate the mechanical properties and phase transition pressure/temperature of the MOFs. A key problem with much of literature on determination of them for MOFs is use of gas molecules or liquids as PTM in both experimental and computational studies. Although these reports provide crucial information for some applications (such as gas adsorption, separation), it is not possible to reveal mechanical properties of the frameworks reliably by using this method. Since the aforementioned experimental methods are not widely available for now, the most appropriate method is computational material tools. To date, the mechanical properties of ZIF-8 have been studied with both classical molecular dynamics (MD) and density functional theory (DFT) simulations. But as far as we know, such a wide pressure range has never been studied before. So in this work, we reported the high-pressure behavior of desolvated ZIF-8 over a wide compression and tension stresses ranging from -2.75 GPa to 50 GPa using ab

initio molecular dynamics (AIMD) simulations, inspired by Suslick's[85] in-situ TEM compression study and Hu's[30] DAC experiment. We witnessed a crystal-amorphous phase transition, a possible fracture of the material on compression, and a crystal-crystal phase change upon decompression through the simulations. The amorphization took place under uniaxial compression as well. Under tension, the framework was failed at -2.75 GPa. The mechanical and electronic properties of the framework were also investigated.

4.2 Methodology

The optimization of the structure and the behavior of ZIF-8 as a function of pressure were studied a LCAO (Linear Combination of Atomic Orbitals)-based DFT approach as implemented in the SIESTA (version 3.2) code.[100] The Perdew-Burke-Ernzerhof (PBE) generalized gradient approximation (GGA)[96] for the exchange-correlation potentials and non-local norm conserving Troulier-Martins pseudopotentials[101] were used to define the ion-electron interactions. The Kohn-Sham orbitals were expanded by numerical orbital basis sets with double- ζ polarized (DZP) functions. Real space integration was performed on an ordered grid corresponding to a plane-wave cut off of 250 Ry and only Γ -point sampling of k-mesh was used. All calculations were performed with periodic boundary conditions.

Starting coordinates and lattice parameters were taken from X-ray diffraction derived structure of ZIF-8.[140] The geometry optimization was performed by a conjugate gradient (CG) variable cell method based on the independent variation of both atomic positions and unit cell parameters. Once the force tolerance criterion of 0.001 eV/\AA was achieved, the structure was considered to be optimized. Pressure studies were performed based on the Parrinello-Rahman method[99] with the power quench technique under isoenthalpic-isobaric (NPH) ensemble. A period of 5000 MD steps was applied to have equilibrium state at each pressure step. Also, additional 5000 MD steps were run at and before the phase transitions to guarantee that the system reached to the true equilibrium

volume. The time step for each MD simulation was 1 femtosecond (fs). Pressure was applied to the framework as follows: The optimized zero-kelvin structure was used as starting geometry and pressure (P) was increased (or decreased) with a ΔP pressure step. At each new pressure $P + \Delta P$, the pressure was applied to the structure obtained from the previous pressure (P). The ΔP was 0.25 GPa from -2.75 to 5 GPa, 1 GPa from 5 GPa to 10 GPa, and 2 GPa from 10 GPa to 50 GPa. Thence, we were able to simulate the pressure dependence of the framework and explore the first/second order phase transitions. Through the study, two different types of pressure were applied to the structure. Under hydrostatic pressure, the simulation box was compressed or tensioned in all three directions. To apply uniaxial pressure, we compressed or tensioned the simulation box along the [100] for x, [010] for y and [001] for z directions. A dispersion correction term was not used through the calculations since the framework materials were less influenced by van der Waal-type interactions.[82] The VESTA[120] program for visualization of the obtained structures and the ISAACS code[103] for further structural analysis were used.

4.3 Results & Discussion

The cell parameter ($a = 17.01 \text{ \AA}$) and bulk modulus ($K = 8.46 \text{ GPa}$) of the relaxed ZIF-8 structure provided in Table 4.1 are in excellent agreement with the experimental data,[146] emphasizing the validity of our simulation. Figure 4.1 presents the hydrostatic pressure dependence of the unit cell volume. The volume shows a gradual decrease of approximately 22% up to 2.5 GPa. Then, the volume is drastically reduced at 3.0 GPa, indicating a first order phase transition. Beyond this pressure, the framework less reacts to the applied pressure, and the change in the volume is around 15% in the range of 3.5 – 50 GPa. Figure 4.2a shows total pair distribution functions (PDF) of ZIF-8 as a function of pressure. Until the transition occurs, the structure preserves its symmetry because the PDFs for 0 and 2.5 GPa structures remain almost the same. On the other hand, beyond the short-range order (SRO) defined as the

distance between two Zn^{2+} (6 Å), there is no significant peak belonging to ZIF-8 at 3 GPa, indicating that framework does not have a long-range order, namely it is amorphous. At 10 GPa and higher pressures, $g_{\text{Zn-Zn}}(r)$ (6 Å), $g_{\text{Zn-N}}(r)$, (4.2 Å) eventually diminish. However, the pattern below 3 Å is the same for all pressure ranges, providing evidence for the preservation of integrity of the imidazole rings.

Constant/Unit	This work (GGA-PBE (0 K)	Ortiz et al. (MD)[71]	Tan et al.[146] Exp. (Brilloun Scattering (295K)	Tan et al.[146] PBE (0 K)
a (Å)	17.01	-		17.26
C11 (GPa)	10.02	11.3	9.52	10.14
C12 (GPa)	7.69	7.6	6.87	8.00
C44 (GPa)	1.22	2.7	0.97	0.78
K (GPa)	8.46		7.75	8.71
GV (GPa)	1.198		1.11	0.90
GR (GPa)	1.197		1.08	0.87
GH (GPa)	1.1975		1.095	0.885
E (GPa)	3.43		3.145	2.57
ν	0.43		0.43	0.45
ν_t (m/s)	1140			~1200
ν_l (m/s)	3258			~3100
ν_m (m/s)	1296			

Table 4.1 Mechanical properties of ZIF-8

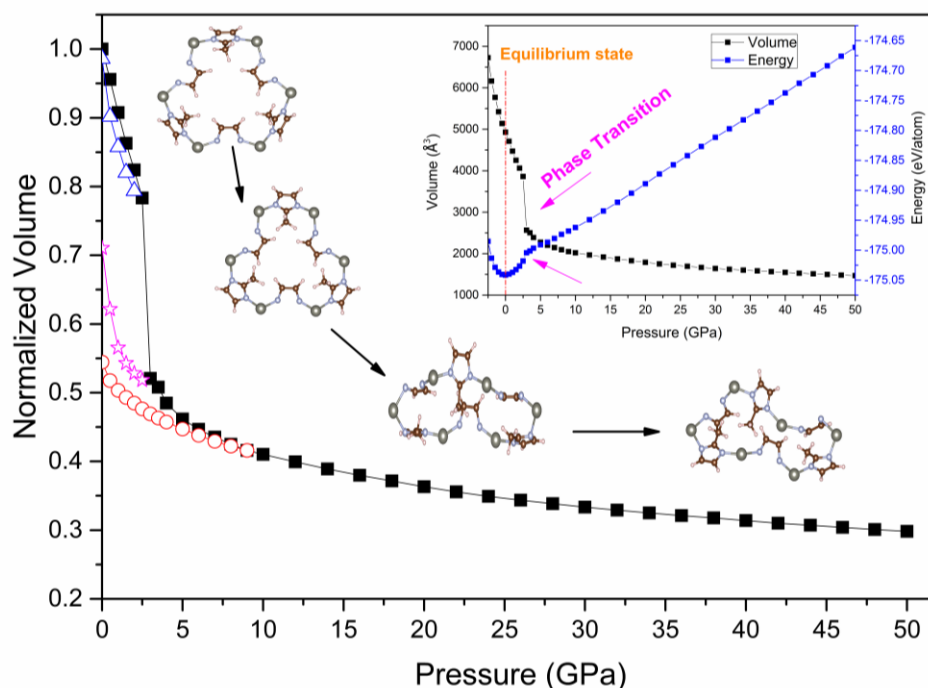


Figure 4.1 The hydrostatic pressure dependence of ZIF-8 unit cell. Solid data represents an increase in pressure. The blue, pink and red open data show releasing of pressure from 2.5, 3 and 10 GPa respectively.

According to the coordination number (CN) analysis performed using the ISAACS code, no coordination modification is observed during the pressure-induced amorphization and the CN of Zn remains 4 up to 10 GPa at which point it drops to 3.67, i.e., some Zn-N bonds are broken in this pressure range. The CN of Zn decreases gradually to 2.54 at 30 GPa. Beyond this pressure, CN of Zn firstly drops to 2 at 40 GPa and then, to 1.6 at 50 GPa (Figure 4.2c). Our critical pressure for the hydrostatic compression correlates fairly well with the experimental amorphization pressure of 4 GPa.[85] The decrease of the CN is interpreted as the fracture of the framework. According to our calculations, the fracture begins beyond 10 GPa.

Previously, it has been reported that the PIA transition of zeolites[147] and ZIFs[73] may be reversible. In order to uncover whether the phase transitions observed in this study are reversible, we release the applied pressure on the framework from following pressures: (i) 2.5 GPa at which the structure remains crystal, (ii) 3.5GPa at which transition ends, (iii) 10 GPa at which first bond

breaking is observed. The total PDFs for these structures are shown in Figure 4.2b. Firstly, once the pressure is released from 2.5 GPa, the framework recovers almost the entire volume, but the obtained structure, hereafter referred as ZIF-8-HP, differs slightly from ZIF-8. As previously reported, the imidazolate ligands under pressure freely rotate to increase the accessible pore window. This phenomenon is named “swing effect” and defined by ϕ angle [139, 148]. The calculated ϕ angles for ZIF-8 and ZIF-8-HP are 19.8° and 10.6° respectively. These results indicate that ZIF-8 is in a “gate-closed” configuration, and ZIF-8-HP is in a relatively “gate-opened” configuration. Further, the symmetry analysis with KPLOTT [122] confirmed that ZIF-8-HP has the same space group symmetry ($I\bar{4}3m$) with ZIF-8. Secondly, when the pressure is released from 3.5 GPa the structure recovers approximately 25 % its starting volume ($V/V_0 = 0.71$). Figure 4.2b illustrates, beyond the (SRO) there is no significant peak, meaning that framework remains amorphous, referred as apZIF-8. Finally, the structure released from 10 GPa recovers 13% of the starting volume ($V/V_0 = 0.71$), and as expected this structure does not have a long-range order as well.

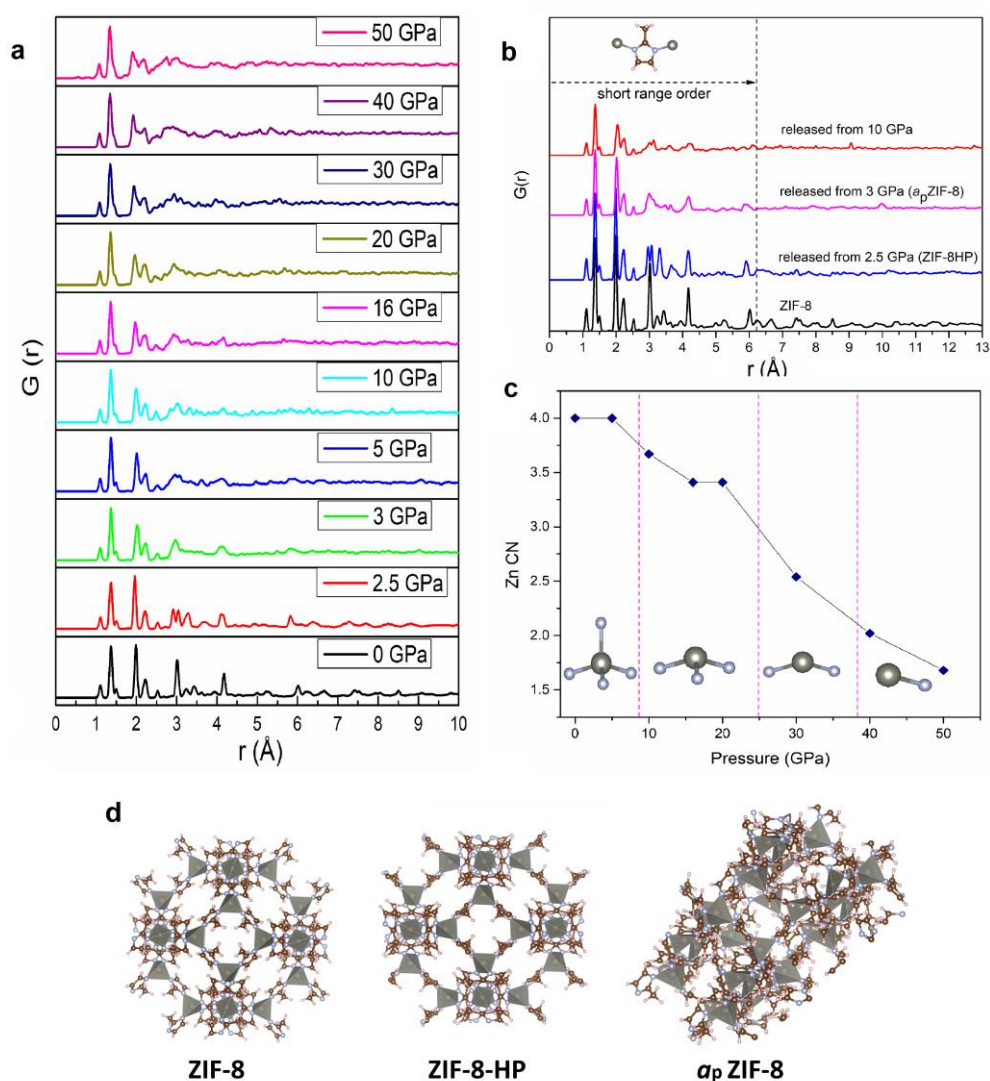


Figure 4.2 (a) Total pair distribution functions (PDFs) data for structures formed at 0-50 GP pressure range. (b) Total PDFs for released pressure structures. (c) Coordination number (CN) of Zn as a function of pressure. (d) structural views of the frameworks obtained in this work.

Figure 4.3a shows partial pair distribution functions (PPDF) for ZIF-8, a_p ZIF-8 and the experimentally ball-mill amorphized framework, referred as amZIF-8. Evidently, $g_{Zn-N}(r)$ peaks (at 2 and 4 Å) ascribing the bonds between metal and ligand in the crystal structure are preserved in the amorphous structure. Similarly, the C-C (1.3 and 2.1 Å), C-N (1.3, 2.2, 2.6 Å) and N-N (2.2 and 3.2 Å) correlations are retained below 6 Å. The calculated PDFs are well match

with experimental data obtained for the ball-mill amorphized ZIF-8,[21] further confirming the validity of our calculations.

To examine the effects of phase transition on bond angles, we study the key bond angle distributions for ZIF-8 and apZIF-8 (Figure 4.3b). In ZIF-8, the N-Zn-N bond angles (θ_{N-Zn-N}) are at 108° and 109° depending on whether the bonding is within 4MR or 6MR pore windows. On the other hand, the θ_{N-Zn-N} shows a wide range of distribution from 90° to 150° in apZIF-8, suggesting that distortions in the tetrahedral units are very effective on the phase transition, or vice versa. The Zn-N-C bond angles (θ_{Zn-N-C}) are at 122° and 126° in ZIF-8, but it shows a wide distribution from 110° to 135° for the amorphous phase.

To see how the structure behaves in the tensile regime we apply tensile stresses to ZIF-8. The framework's volume linearly increases up to -2.75 GPa and beyond this pressure, the structural failure, which is defined as a tremendous increase in volume and breakage of almost all bonds, is observed.

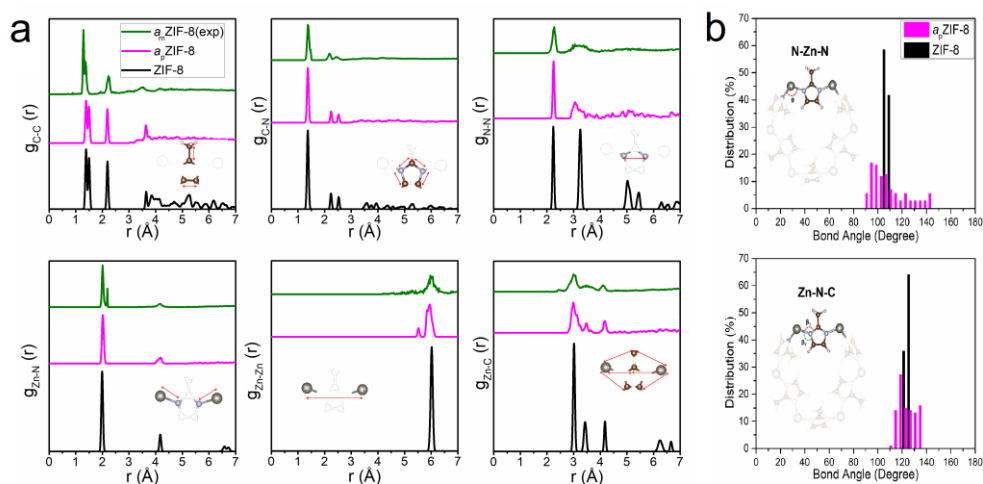


Figure 4.3 (a) Partial pair distribution functions of ZIF-8, ZIF-8-HP and a_p ZIF-8, and a_m ZIF-8. (b) Bond angle distributions for ZIF-8 and a_p ZIF-8.

According to the previous reports, ZIF-8 shows structural anisotropy.[85, 146] Therefore, the mechanical properties of the framework are highly dependent on the orientation of applied stresses. In order to investigate the effect of direction of uniaxial stresses on the crystalline-amorphous phase transition; we apply

uniaxial pressure on the framework. The changes of the ZIF-8-unit cell volume under uniaxial pressures are shown in Figure 4.4. It is obvious that the deformation process occurs in three steps: (i) a linear volumetric reduction of 15% is observed over the pressure range of 0-1.5 GPa; (ii) the framework resists further compression and just a small reduction of 7% in volume occurs up to 4 GPa; (iii) the volume drastically drops between 4-5.5 GPa, and the final reduction in volume is about 50% at 5.5 GPa. Then, the framework partially retrieves to 62% of its starting volume upon the release of pressure. Similar to hydrostatic pressure, the CN of Zn-atoms maintains through all uniaxial pressures. There are no significant differences between uniaxial amorphous phases in terms of density. However, the amorphous phases formed under uniaxial pressure are about 20% denser than the one formed under the hydrostatic pressure. The trend in uniaxial P-V curves is in good agreement with Suslick's in situ TEM compression results[85]. However, amorphization pressures are overestimated in this work due to the simulation conditions, such as lack of surface effects, fast loading etc.

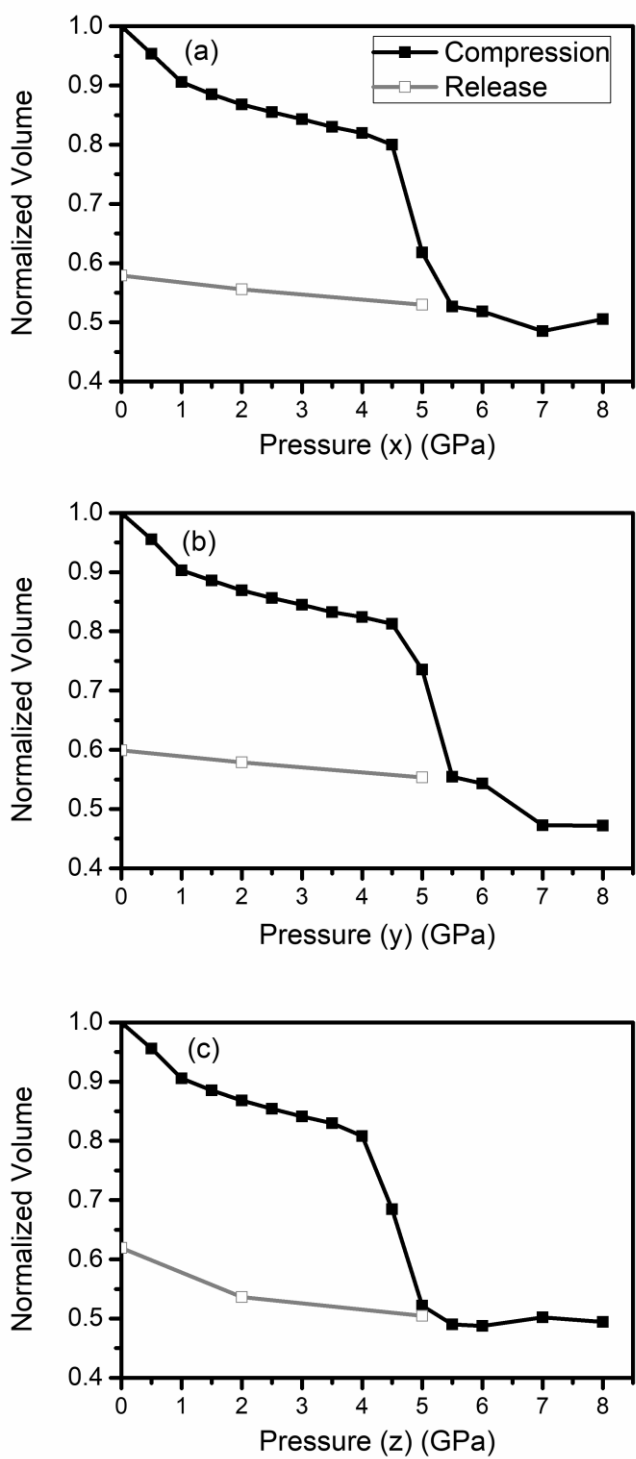


Figure 4.4 The uniaxial pressure dependence of ZIF-8 unit cell.

Zero Kelvin elastic constants can be estimated from the energy variation by applying small strains to the equilibrium structure.[149, 150] The elastic energy of a solid is defined by

$$E = E_0 + \frac{V}{2} \sum_{i=1}^6 \sum_{j=1}^6 C_{ij} e_i e_j + O(e_i^3) \quad (4.1)$$

where E_0 and V is the equilibrium energy and volume, C_{ij} is the elastic constants, e_i and e_j are strains vectors. Due to the symmetry, there are three independent elastic constants C_{11} , C_{12} and C_{44} for cubic structure. When a volume preserving orthorhombic strain is applied on the lattice:

$$\begin{pmatrix} \delta & 0 & 0 \\ 0 & -\delta & 0 \\ 0 & 0 & \delta^2 / (1 - \delta^2) \end{pmatrix} \quad (4.2)$$

Equation 4.1 reduces to:

$$E(\delta) = E(0) + (C_{11} - C_{12})V\delta^2 + O(\delta^4) \quad (4.3)$$

Additionally, there is a relationship between bulk modulus and those two elastic constants,

$$K = \frac{1}{3}(C_{11} - 2C_{12}) \quad (4.4)$$

To calculate C_{44} , a volume preserving monoclinic strain is applied,

$$\begin{pmatrix} 0 & \delta & 0 \\ \delta & 0 & 0 \\ 0 & 0 & \delta^2 / (1 - \delta^2) \end{pmatrix} \quad (4.5)$$

In this case, Equation (4.1) transform into:

$$E(\delta) = E(0) + 2C_{44}V\delta^2 + O(\delta^4) \quad (4.6)$$

After for each set of strain calculation, data were fitted to (4.3) and (4.6) equations to obtain C_{11} , C_{12} and C_{44} .[45] Also, it is possible to calculate the useful elastic properties for polycrystals by Voigt, Reuss and Hill

approximations with elastic constants of single crystals.[151] According to these approximations, shear modulus G is defined by,

$$\begin{aligned}
 5G_{Voigt} &= C_{11} - C_{12} + 3C_{44} \\
 \frac{5}{G_{Reuss}} &= 4(S_{11} - S_{12}) + 3S_{44} \\
 G_{Hill} &= \frac{1}{2}(G_{Reuss} + G_{Voigt})
 \end{aligned} \tag{4.7}$$

where S_{ij} are elements of elastic compliance matrix (S), which is inverse of elastic constants matrix. Moreover, Young's modulus (E), Poisson's ratio (ν), and the sound wave velocities; transverse (v_t), longitudinal (v_l) and mean (v_m) are derived by using G_H (shear modulus by Hill approximation), E, ν and K_H (bulk modulus by Hill approximation) (Equation 4.8).[151]

$$\begin{aligned}
 E &= \frac{9K_H}{\left(1 + \frac{3K_H}{G_H}\right)} \\
 \nu &= \frac{\frac{1}{2}(K_H - \frac{2}{3}G_H)}{\left(K_H + \frac{1}{3}G_H\right)}
 \end{aligned} \tag{4.8}$$

$$v_t = \sqrt{\frac{G_H}{\rho}}, \quad v_l = \left(\frac{E(1-\nu)}{\rho(1+\nu)(1-2\nu)}\right), \quad v_m = \left(\frac{1}{3}\left(\frac{2}{v_t^3} + \frac{1}{v_l^3}\right)\right)^{-1/3}$$

The elastic and mechanical constants of ZIF-8 obtained in this work are shown in Table 4.1 and comparable with available data in the literature. [71]

For a more accurate determination of pressure region where the framework is subjected to elastic and plastic deformation, ZIF-8 was exposed to uniaxial pressure between 1.5 and -1.5 GPa ,with an increment of $\Delta P = 0.1$ GPa. The

stress-strain curves are shown in Figure 4.5. As previously reported [146] and it is clearly apparent from calculations -vide supra-, the framework shows a slight anisotropy with the highest strength on x-axis. The average Young's modulus, E_{avg} , obtained from the slope of stress-strain curve in elastic region is 5.6 GPa, which is consistent with the experimental value. ($E_{load}=4.6$ GPa).[85] The most important result to be noted here is that the compression and tensile strength of the material are very different from each other. Accordingly, the tensile strength of the structure is 50% higher than its compression strength. While ductile materials generally have the same compression and tension strengths, they can be different for brittle materials.[152] Such a distinct behavior also has been observed in lamellar and porous bones.[152] Analogous to compact bones, ZIF-8 is mechanically weak against to compression forces since the structure is highly porous. Still, due to the flexible nature of the framework it shows relatively higher tensile strength.

Poisson's ratio of ZIF-8 was calculated from the strain values obtained in this regime, with following formula:

$$V_{ij} = - \frac{\Delta L_i / L_i}{\Delta L_j / L_j} \quad (4.9)$$

where L_{ij} are the diagonal terms of the lattice parameters. For compression and tension regions, six different Poisson's ratios were estimated. The averaged Poisson's ratio obtained for the applied compression and tension stresses are 0.4 and 0.5, respectively. The compression value is well match with both Poisson's ratios in the literature[146] and predicted using the Hill approximation in this work.

To summarize and compare, the elastic moduli of metals and metal alloys are around 100 GPa and above, and their Poisson's ratios are in the range of 0.2-0.3. Ceramics have relatively lower elastic modulus (typically $E \sim 60-70$ GPa), and Poisson's ratio ($\nu \sim 0.2$). Polymers have very low elastic modulus ($E \sim 1-3.5$ GPa) and very high Poisson's ratios (0.4-0.5). As confirmed by our results and other

studies[72] in the literature, ZIF-8 is mechanically very similar to polymeric materials.

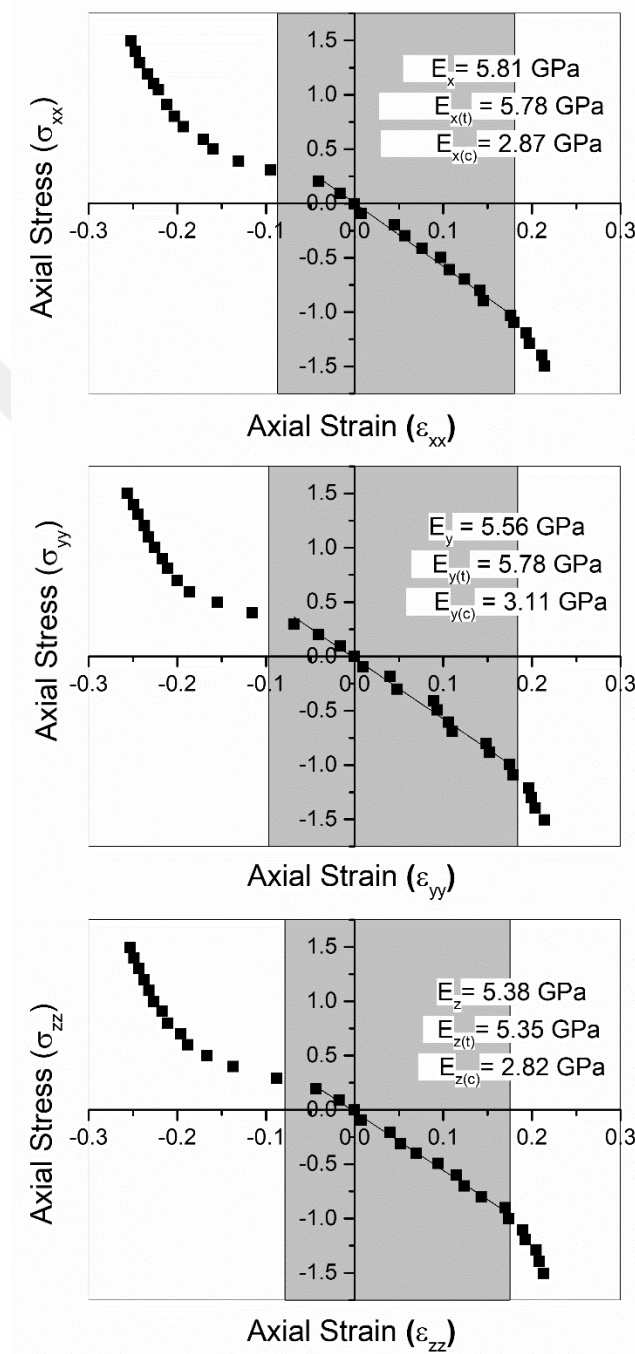


Figure 4.5 Stress-strain curves of ZIF-8 unit cell.

The calculated partial density of states (PDOS) and total density of states (TDOS) for ZIF-8 and apZIF-8 are shown in Figure 4.6a and 4.6b, respectively.

Both phases demonstrate similar features in the DOS curves. The energy bands between -18 and -10 eV mainly consist of 2s electronic states of N, H and C atoms. More significantly, in the upper portion of valence band (VB), where from -7.5 eV to -2.5 eV, a hybridization occurs between 1s-state of H, 2s-, 2p-states of N and C and 3d state of Zn, indicating the covalent bonds on imidazole ring and coordination bond between Zn and N. In contrast to discontinuous structure of VB, the conduction band (CB) has a continuous form. The sharp peak is assigned to hybridization of 2p-states of N and C atoms. The most likely underestimated band gap for ZIF-8 and apZIF-8 due to the ground state formalism of DFT is 4.4 and 4.3 eV, respectively. These results indicate that ZIF-8 and apZIF-8 are good insulators. Clearly, a crystal-amorphous phase transition in ZIF-8 does not significantly alter the electronic properties of the framework, despite the changes in charge distributions, bond lengths and bond angles. The most important reason of such an observation is that the electronic structure of ZIF-8 is dominated by insulating 2-methylimidazole ligands.[55] For example, as reported in our previous study,[153] the band gap of MOF-5, which is containing relatively conductive terephthalic acid (BDC), significantly decreases under a crystalline-amorphous phase transition.

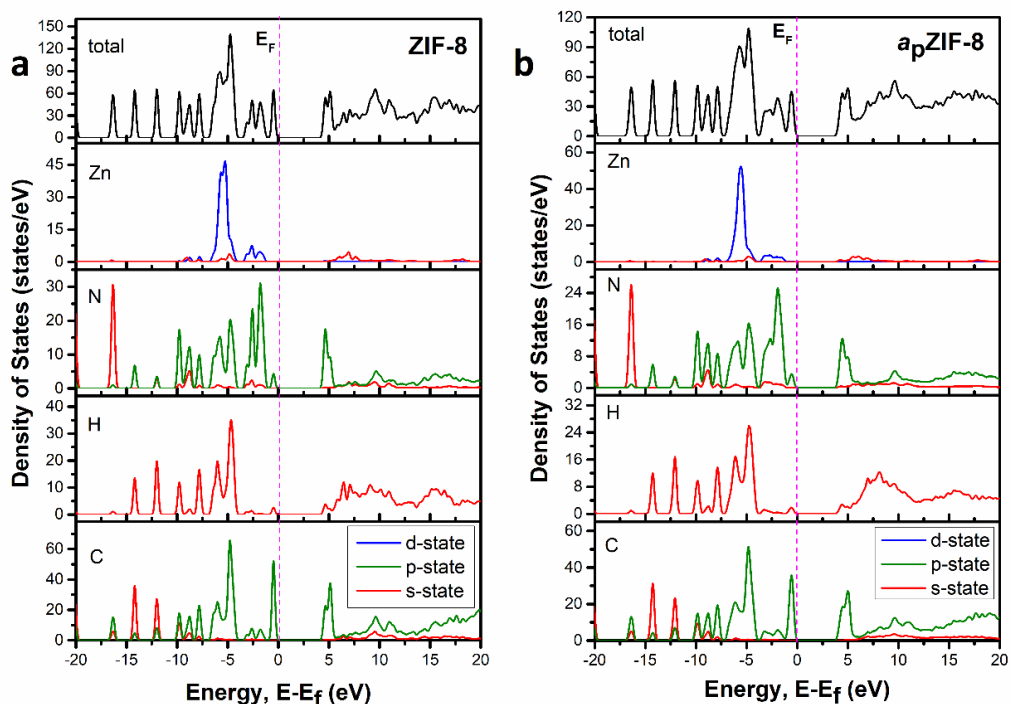


Figure 4.6 Calculated total and partial density of states (DOS) for (a) ZIF-8 and (b) a_p ZIF-8.

4.4 Conclusion

We have presented the pressure-induced amorphization of ZIF-8, and its mechanical and electronic properties by using ab initio molecular dynamics simulations. The Parinello-Rahman algorithm appears to be very successful in reproducing experimentally observed crystal-crystal phase transition and crystal-amorphous transition. The overestimated critical pressures can be ascribed to the simulation conditions, such as lack of surface effects due to the periodic boundary conditions, non-defective structure etc. All mechanical properties of ZIF-8 are accurately estimated by using two different approaches, and interestingly like compact bones, different compression and tensile strengths are proposed for the crystalline framework. The electronic properties of ZIFs are mostly governed by imidazolate linkers. Since the imidazolate retains its structural integrity, the crystal-amorphous phase transformation does not have significant impact on the electronic properties of ZIF-8.

Chapter 5

Pressure Induced Phase Transitions in Zeolitic Imidazolate Frameworks (ZIFs) Polymorphs

5.1 Introduction

Zeolitic imidazolate frameworks (ZIFs), a sub-class of MOFs, are isomorphous with zeolites, and they usually exhibit exceptional chemical and thermal stabilities. ZIFs are composed of tetrahedral inorganic building units, wherein every divalent metal cation M^{2+} ($M = Co$ and Zn) coordinates to four imidazolate based anion linkers ($Im^- = C_3H_3N_2^-$) to form neutral porous framework structures ($M(Im)_2$) with zeolitic topologies.[70, 72, 130]

Non-crystalline or amorphous ZIFs have been attracting considerable interest due to their extraordinary properties.[19] In order to elucidate their structures, several experimental characterization techniques have been used, including EXAFS,[154] neutron diffraction,[155] positron annihilation lifetime spectroscopy (PALS),[155] Raman spectroscopy and Brillouin spectroscopy.[156] Also in a few research, MD simulations[157] and ab-initio calculations[158] have been performed.

In this work, we focus on the pressure-induced phase transitions of three ZIF structures, ZIF-1 to ZIF-3, all of which has the same chemical composition $Zn(Im)_2$ (Figure 5.1). However, their physical properties, geometrical parameters, crystal symmetries and network topologies are significantly different. We show that the behavior of ZIF-1 to ZIF-3 under hydrostatic pressure is distinctive from each other using AIMD simulations. We have

explored a number of high pressure phase transitions, including crystal-crystal, crystal-amorphous and amorphous-amorphous, which are previously unreported.

5.2 Methodology

The LCAO (Linear Combination of Atomic orbitals)-based DFT code, SIESTA[100] (version 3.2), was used to optimize the starting geometries and simulate the high-pressure phases of ZIFs. The Perdew-Burke-Ernzerhof (PBE) generalized gradient approximation (GGA),[96] the Troulier-Martins pseudopotentials,[101] and the double- ζ polarized orbitals were preferred for the simulations. Real space integration was carried out on an ordered grid corresponding to a plane wave cut off of 250 Ry. Due to the relatively higher number of atoms in the simulation boxes, only Γ -point sampling of k-mesh was used. Van der Waals corrections (DFT-D) were applied using semiempirical dispersion potential parametrized by Grimme.[159]

The initial atomic coordinates with the lattice parameters were taken from X-ray diffraction derived structures of ZIF-1, ZIF-2 and ZIF-3. The conjugate gradient variable cell (CG-VC) procedure was used to relax the positions of atomic nuclei with the force tolerance criterion of 0.001 eV/Å. The hydrostatic pressure was applied on the structures by the Parrinello-Rahman method[99] within the power quench technique under isoenthalpic-isobaric (NPH) ensemble. Pressure was applied to the frameworks as follows: The relaxed zero-Kelvin system was used as an initial structure. Then, pressure was increased/decreased with a $\Delta P=0.25$ GPa pressure step in both tension and compression regions. Note that the negative values of pressure denote tension. Pressure was applied to the structure obtained from previous pressure step for each new pressure. At each pressure step, a period of 5000 MD steps was performed to obtain equilibrium state. In order to guarantee that the system had the true equilibrium volume, additional 5000 MD steps were used at and just before phase transitions. Each MD time step was set to 1 fs. The VESTA[120] program for visualization and ISAACS code[103] for post-processing of obtained data were used.

5.3 Results & Discussion

Firstly, in order to identify the behavior of the ZIFs under the applied hydrostatic pressure (for compression and tension), the volume and total energy values were plotted as a function of pressure. So that we would be able to explore phase transitions since the discontinuities and slope changes in the volume versus pressure plots are an indicative of the first/second order transitions. After the detection of the phase changes, to investigate the structures, their total and partial pair distribution functions (PDFs) were plotted for each phase. The average values and standard deviations of pertinent distances ($d_{\text{Zn-N}}$) and angles ($\theta_{\text{N-Zn-N}}$ and $\theta_{\text{Zn-N-C}}$) were derived from PDFs, and coordination numbers (CNs) were calculated to describe the structural changes in the frameworks. And last, while the fracture is defined as the partial bond breakage through the frameworks, the structural failure, which is observed in tension regime, refers as a tremendous increase in volume and breakage of almost all bonds.

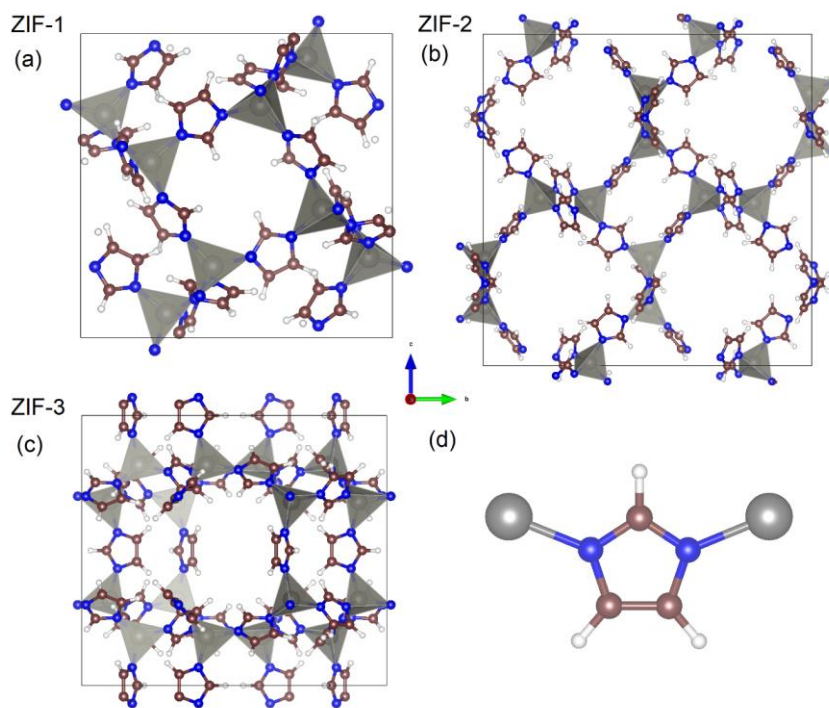
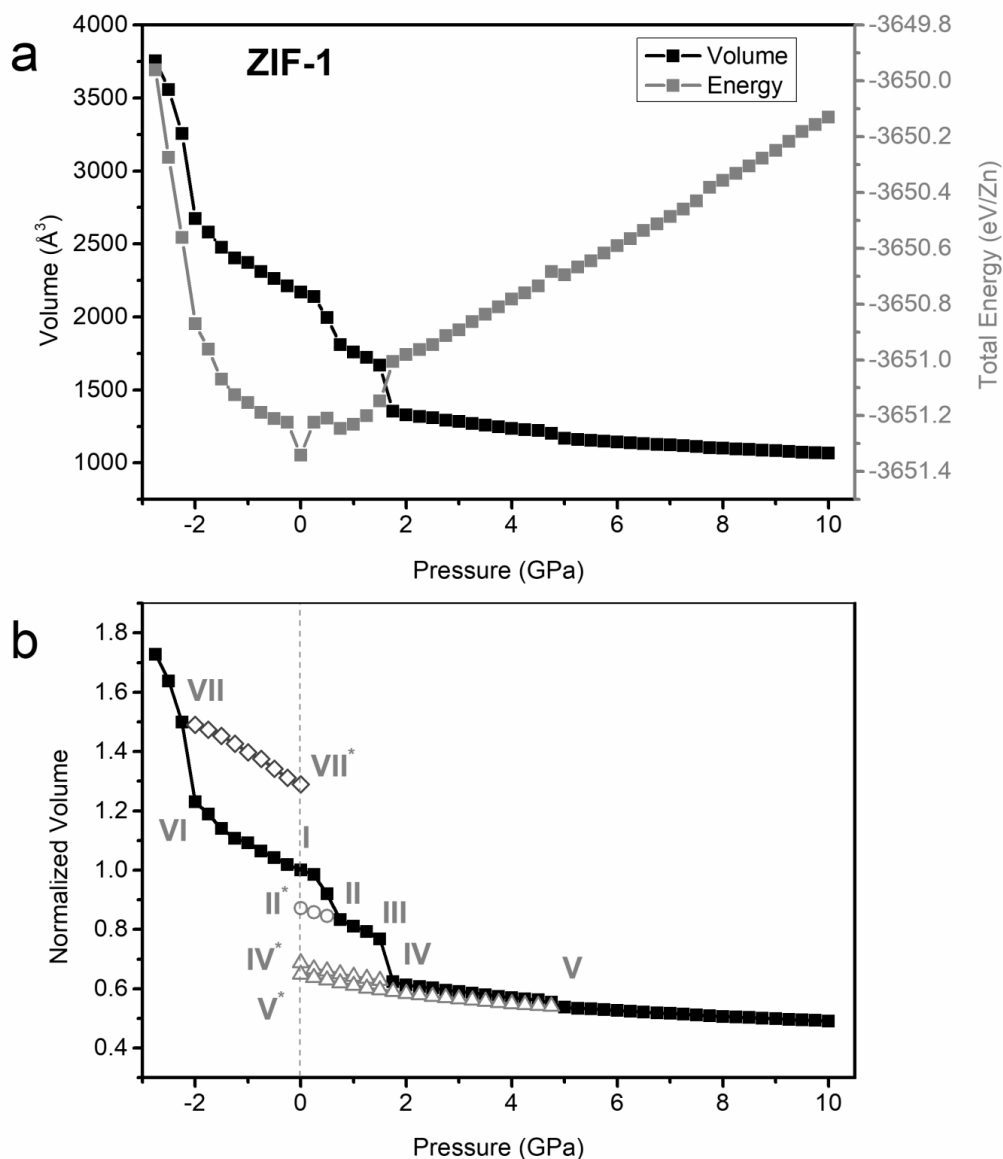


Figure 5.1 Equilibrium crystal structures of (a) ZIF-1, (b) ZIF-2, (c) ZIF-3. (d) Zn-Im-N coordination in a subunit

ZIF-1: Figure 5.2 shows the unit cell volume and its total energy of unit cell per Zn atom as a function of pressure. Phase I is the equilibrium structure, which has the minimum energy configuration at 0 GPa. For equilibrium structure, we found $d_{\text{Zn-N}} = 1.983 \pm 0.031 \text{ \AA}$, $\theta_{\text{N-Zn-N}} = 109 \pm 3^\circ$, and $\theta_{\text{Zn-N-C}} = 126 \pm 3^\circ$. At 0.75 GPa, phase I transforms discontinuously into a phase II of significantly smaller volume. For phase II, we obtained $d_{\text{Zn-N}} = 1.975 \pm 0.032 \text{ \AA}$, $\theta_{\text{N-Zn-N}} = 109 \pm 7^\circ$, and $\theta_{\text{Zn-N-C}} = 125 \pm 6^\circ$. It is apparent from Figure 5.2 that phase II located in a local-energy minimum, indicating a novel phase of ZIF-1. However, this transition is not accompanied by any bond breakage or forming according to CN number analysis. From phase II to phase III (1.5 GPa), a continuous decrease in the volume was observed, but no significant change in Zn-N distance ($d_{\text{Zn-N}} = 1.978 \pm 0.032 \text{ \AA}$) and Zn_4 tetrahedra ($\theta_{\text{N-Zn-N}} = 109 \pm 7^\circ$) was perceived. At 1.75 GPa, phase III now transforms discontinuously into phase IV. As in the previous case, this transition does not involve any bond breakage/forming but the structural changes mostly affect the Zn tetrahedra. Also we revealed the collapse of four-member rings (4MR) in the framework. For phase IV we obtained $d_{\text{Zn-N}} = 1.984 \pm 0.037 \text{ \AA}$, $\theta_{\text{N-Zn-N}} = 109 \pm 15^\circ$, and $\theta_{\text{Zn-N-C}} = 121 \pm 6^\circ$. Up to 4.75 GPa there is a continuous decrease in the volume, and continuous increase in total energy. However, between at 4.75 GPa and 5 GPa, both volume and total energy plots show a small discontinuity. We obtained $d_{\text{Zn-N}} = 1.989 \pm 0.050 \text{ \AA}$, $\theta_{\text{N-Zn-N}} = 109 \pm 19^\circ$, and $\theta_{\text{Zn-N-C}} = 122 \pm 9^\circ$ for phase V.

In tension regime, phase I transforms into phase VI (-2 GPa) with a gradual expanding in the framework volume. For phase VI we found $d_{\text{Zn-N}} = 2.062 \pm 0.032 \text{ \AA}$, $\theta_{\text{N-Zn-N}} = 109 \pm 5^\circ$, and $\theta_{\text{Zn-N-C}} = 122 \pm 9^\circ$. At -2.25 GPa, the volume shows a significant increase, a transformation into phase VII. We obtained $d_{\text{Zn-N}} = 2.108 \pm 0.035 \text{ \AA}$, $\theta_{\text{N-Zn-N}} = 109 \pm 5^\circ$, and $\theta_{\text{Zn-N-C}} = 122 \pm 9^\circ$ for phase VII. Beyond this pressure, the volume and total energy continue to increase, and a structural failure was observed at -3 GPa.



**Figure 5.2 a) The volume and total energy per Zn plot as a function of pressure for ZIF-1
b) Normalized volume as a function of pressure for ZIF-1.**

In order to determine the reversibility of the transitions; we released the pressure from the point where phase transitions completed (Figure 5.2b). Clearly, the phase change to II, IV, V and VII are irreversible. Upon decompression from phase II, the framework undergoes minor changes in its structure, and does not transform back to the equilibrium phase due to the trapped in the local energy minima. For phase II* we obtained $d_{\text{Zn-N}} = 1.987 \pm 0.032 \text{ \AA}$, $\theta_{\text{N-Zn-N}} = 109 \pm 6^\circ$, and $\theta_{\text{Zn-N-C}} = 125 \pm 6^\circ$. To check whether transition from I to II is crystal-crystal,

The KPLLOT symmetry analysis was performed for both phase II and II*. Curiously, the space group-symmetry of the phases II and II* were determined to be P21/c. Indeed P21/n and P21/c are different configurations of space group 14, and such a transition –from P21/n to P21/c- has been reported for minerals and molecules.[160] According to the angle analysis, the slight deformation of Zn₄ tetrahedra and rotation of imidazolate linkers can be the underlying mechanism of this crystal-crystal transition. Also, while β is 99° for the equilibrium structure, it is at around 120° for both phases II and II*. This implies that the high pressure phases are very oblique in comparison with the equilibrium phase.

Upon decompression from phase IV and V, the recovered volume is trivial. Once the framework collapses, it does not return to its original state. Also, the structural changes are insignificant during the releasing of pressure. For example, for phase IV* we obtained $d_{\text{Zn-N}} = 2.015 \pm 0.034 \text{ \AA}$, $\theta_{\text{N-Zn-N}} = 109 \pm 15^\circ$, and $\theta_{\text{Zn-N-C}} = 121 \pm 7^\circ$. It would appear that the strong distortions in Zn₄ may trigger irreversible crystal-amorphous and amorphous-amorphous transitions.

The local structural modifications at certain pressures are also probed by total and partial pair distributions functions. Figure 5.3 shows the total pair distribution function of structures formed between -2.25 – 10 GPa for ZIF-2. Clearly, the broadening in the peaks beyond 3Å for the high pressure structures in the compression region was observed. However, the PDF pattern of the structure at -2.25 GPa has sharper peaks, which is very similar with that of the equilibrium phase, in the given range. For the structures formed at pressures higher than 1.5 GPa, the PDF gradually becomes more continuous form. However, even at 10 GPa, sharp peaks are still observed at distances smaller than 3Å, indicating that the imidazolate anion retains its structural integrity.

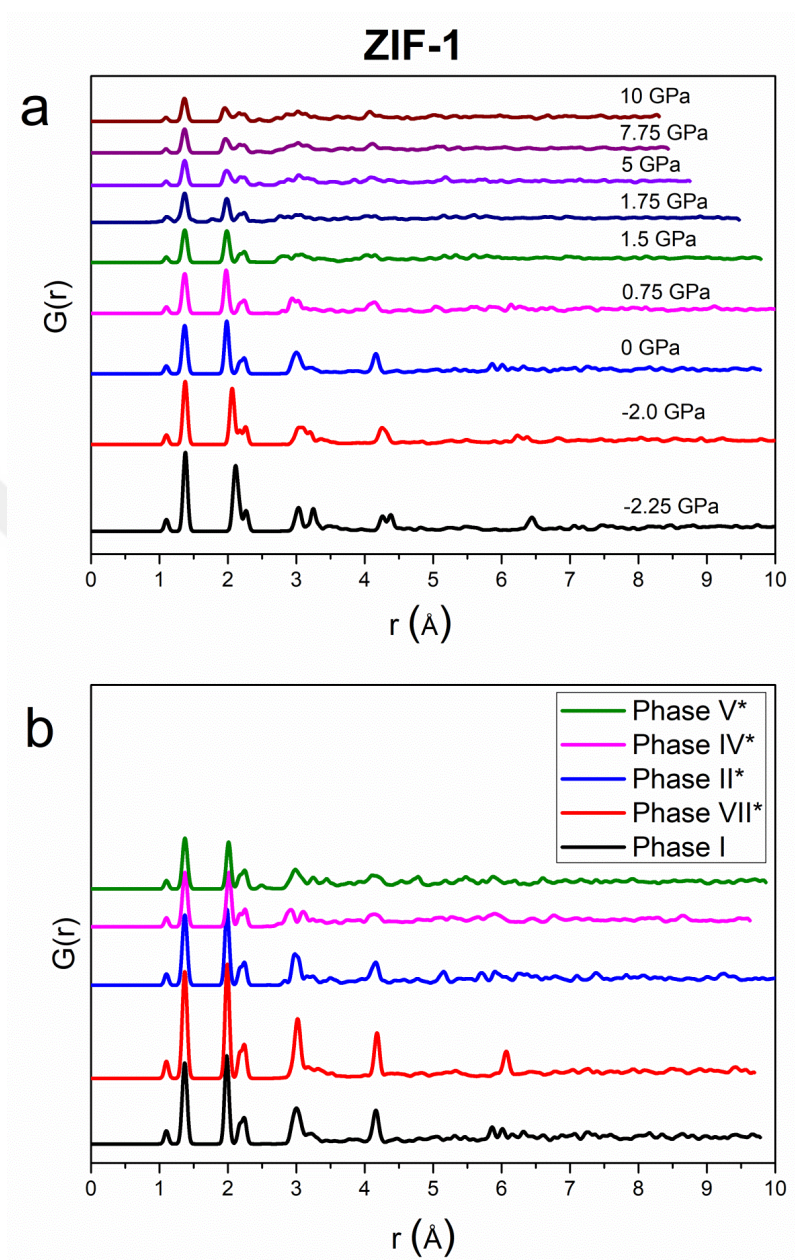


Figure 5.3 Total pair distribution functions (PDFs) data for structures formed at -2.25-10 GP pressure range for ZIF-1

The peaks of $g_{Zn-N}(r)$, which are assigned the coordination between metal and ligand at 2\AA and 4.2\AA , still exist at high pressures, but their intensity decreases and they are broadened (Figure 5.4a-5.4d). In ZIFs, as stated above, $g_{Zn-Zn}(r)$ peaks at 6\AA and beyond the limit of the SRO, have a random pattern for the high pressure phases. For the structures in the tension region, phase I, phase II,

phase II* and phase VII*, the Zn-Zn peaks show a relatively uniform distribution, while it has a nearly-random distribution for the other high-pressure phases, indicating that these phases do not have a long-range order (Figure 5.4b-5.4e). Similar randomness is observed beyond 4.5Å for C-Zn distances, providing additional support for amorphization at pressures above 2 GPa.

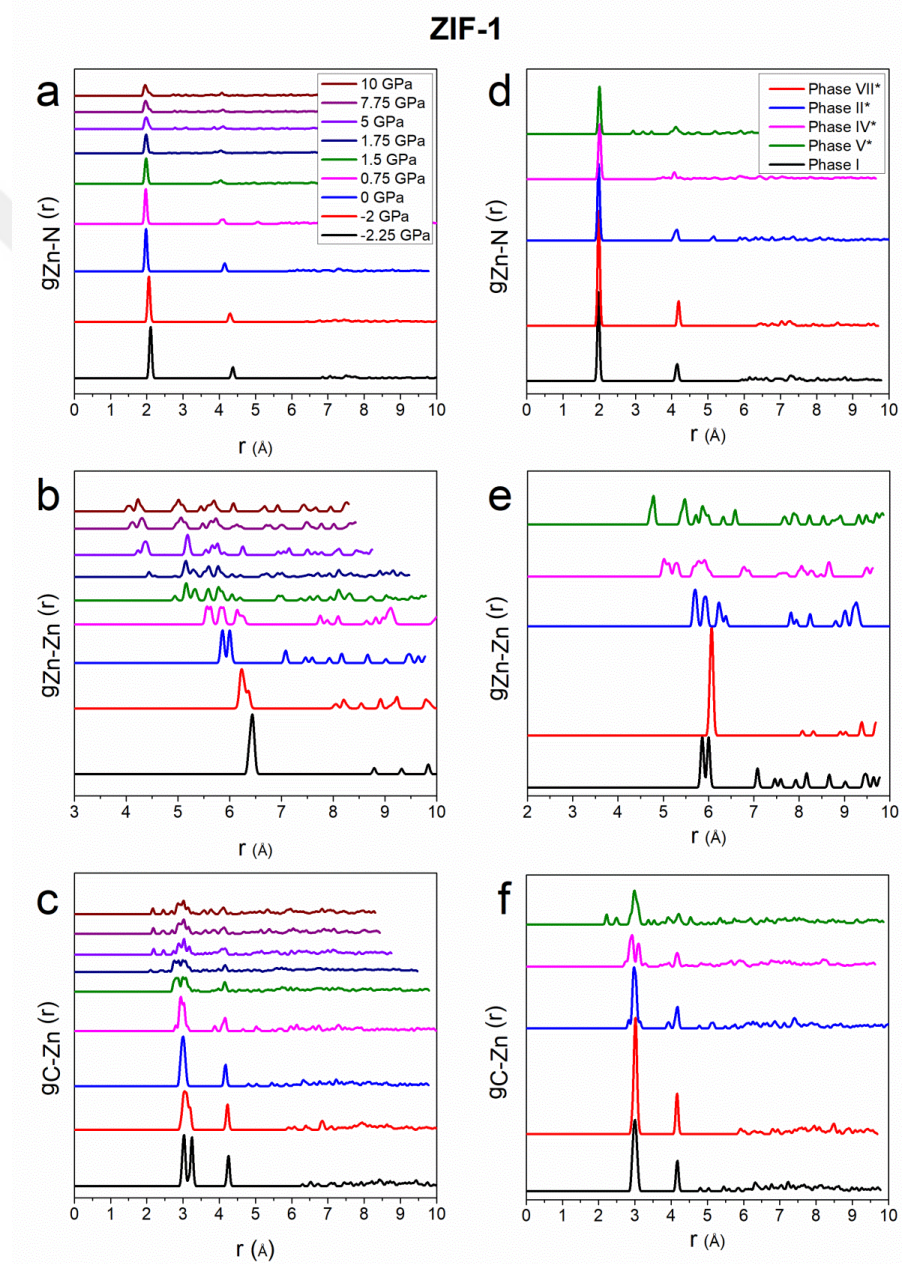
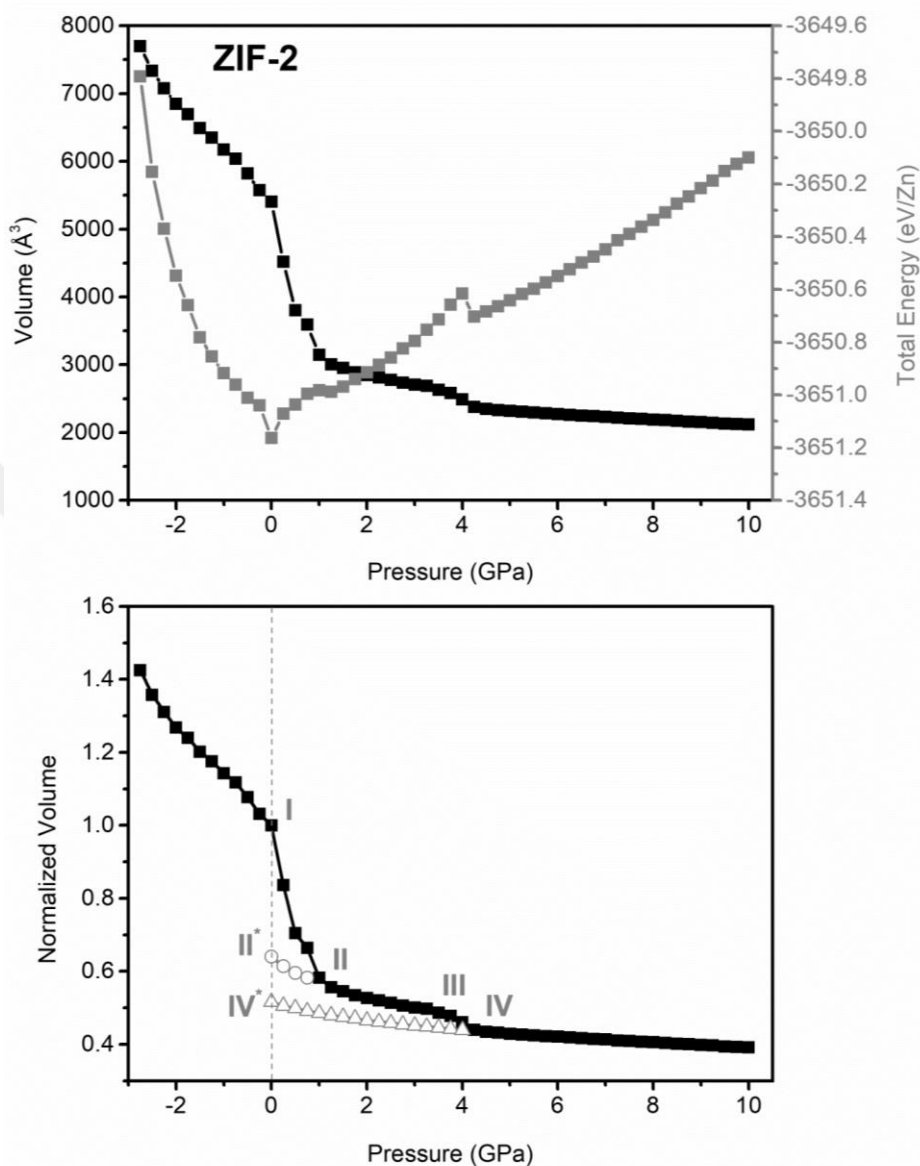


Figure 5.4 Partial pair distribution functions (PDFs) data for structures formed at -2.25-10 GP pressure range for ZIF-1

ZIF-2: The unit cell volume and total energy per Zn atom of the structure as a function of pressure are shown in Figure 5.5a. The reference structure at 0 GPa, phase I, is characterized by $d_{\text{Zn-N}} = 1.980 \pm 0.032$ Å, $\theta_{\text{N-Zn-N}} = 109 \pm 4^\circ$, and $\theta_{\text{Zn-N-C}} = 126 \pm 2^\circ$. Interestingly, the application of hydrostatic pressure immediately leads to a first-order transition. Accordingly, phase I transforms into phase II with a 40% reduction in the volume at 1 GPa. For phase II we found $d_{\text{Zn-N}} = 2.000 \pm 0.037$ Å, $\theta_{\text{N-Zn-N}} = 109 \pm 7^\circ$, and $\theta_{\text{Zn-N-C}} = 125 \pm 6^\circ$. While there is no change in the CN of Zn, relatively strong distortions in ZN_4 tetrahedra and free rotations of imidazolate linkers may cause this transition. Additionally, a collapse is observed in 8MR structure at this pressure. Up to 4 GPa, the volume gradually decreases, the energy, on the other hand, continuously increases. For phase III at 4 GPa we found, $d_{\text{Zn-N}} = 2.010 \pm 0.044$ Å, $\theta_{\text{N-Zn-N}} = 109 \pm 6^\circ$, and $\theta_{\text{Zn-N-C}} = 125 \pm 6^\circ$. At 4.25 GPa, both volume and energy are discontinuously reduced. This small discontinuity can be attributed to another first-order phase transition or may be related to the small size of the simulation box. At this point, although the CN of Zn dropped to 3.67, no major change is detected in ZN_4 tetrahedra. Thus, phase IV at 4.25 GPa is characterized by $d_{\text{Zn-N}} = 2.012 \pm 0.045$ Å, $\theta_{\text{N-Zn-N}} = 109 \pm 7^\circ$, and $\theta_{\text{Zn-N-C}} = 124 \pm 6^\circ$. The volume continues to decrease between 4.25 GPa and 10 GPa. However, there is no change in CN of Zn in this range; it remains as 3.67 up to 10 GPa.

Under tension, the volume continuously increases up to -2.75 GPa, but a structural failure associated with a dramatic volume expansion is observed at 3 GPa. Figure 5.5b also shows the irreversibility of the high-pressure phases of ZIF-2. When the pressure is released from 1 GPa, the system recovers only 10% of its initial volume. For phase II* we found $d_{\text{Zn-N}} = 2.000 \pm 0.034$ Å, $\theta_{\text{N-Zn-N}} = 109 \pm 6^\circ$, and $\theta_{\text{Zn-N-C}} = 125 \pm 6^\circ$. The phase IV* obtained by releasing the pressure from 4.25 GPa has more structural deformation than phase II*, and is more dense. We found $d_{\text{Zn-N}} = 2.017 \pm 0.043$ Å, $\theta_{\text{N-Zn-N}} = 109 \pm 8^\circ$, and $\theta_{\text{Zn-N-C}} = 124 \pm 7^\circ$ for phase IV*. The higher Zn-N distance emphasizes that the structure contains some coordination defects, which is already 3.67 for phase IV.



**Figure 5.5 a) The volume and total energy per Zn plot as a function of pressure for ZIF-2
b) Normalized volume as a function of pressure for ZIF-2.**

The total and partial PDFs for the obtained phases of ZIF-2 are shown in Figure 5.6 and 5.7. The total PDF of phase II shows some similarities with that of the equilibrium structure. On the other hand, there is a broadening of peaks beyond 3 \AA . The PDFs of phase IV and the structure at 10 GPa has continuous form beyond 3 \AA . Similar trend is observed in phase II* and phase IV*.

According to the partial PDFs, the peaks of $g_{\text{Zn-N}(r)}$ still occur at high pressure, even 10 GPa, but the intensity of the peaks decline and the peaks become

broader (Figure 5.7). While $g_{\text{Zn-Zn}}(r)$ shows uniform distribution with sharp peaks at 6 Å and above, it has a random distribution for phase II* and IV*. Similarly, $g_{\text{C-Zn}}(r)$ pattern also has a random distribution with increasing pressure. Both findings confirm that phase II* and IV* are amorphous phases.



ZIF-2

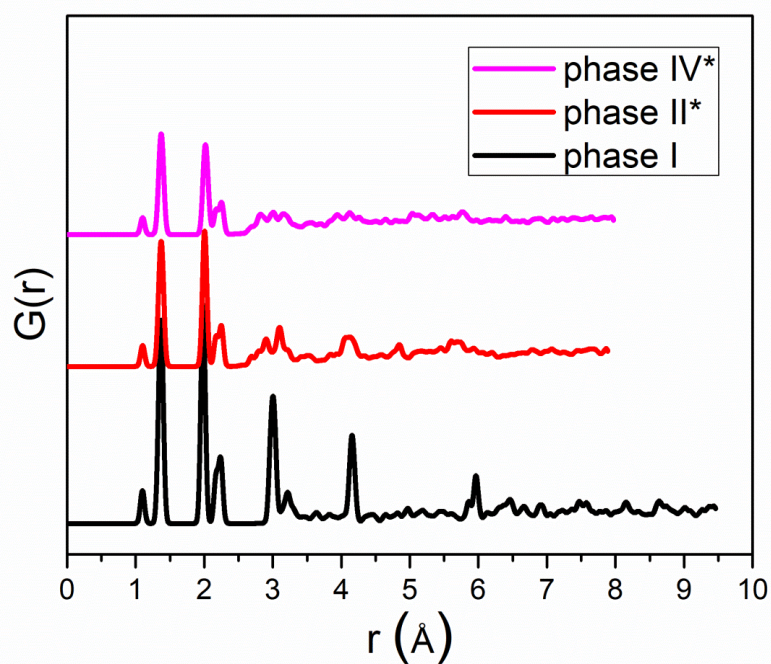
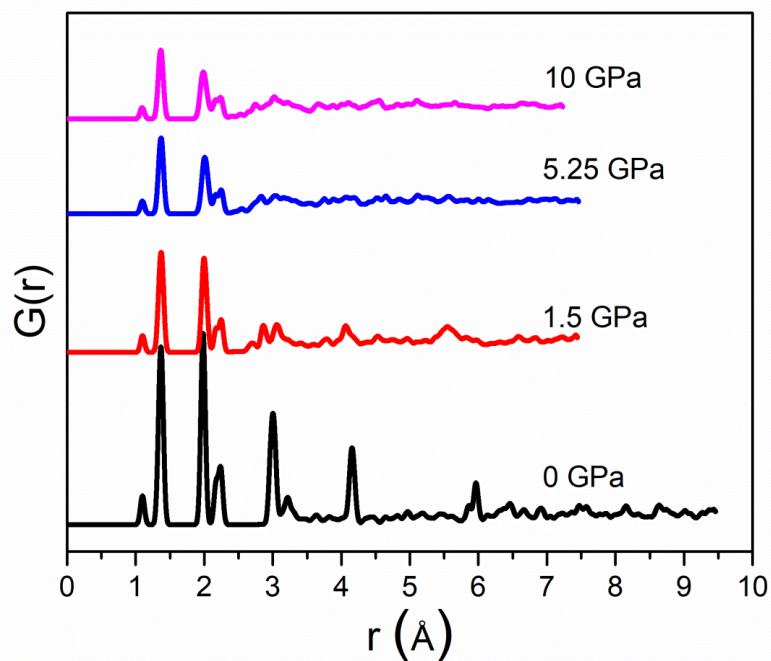


Figure 5.6 Total pair distribution functions (PDFs) data for structures formed at 0-10 GP pressure range for ZIF-2

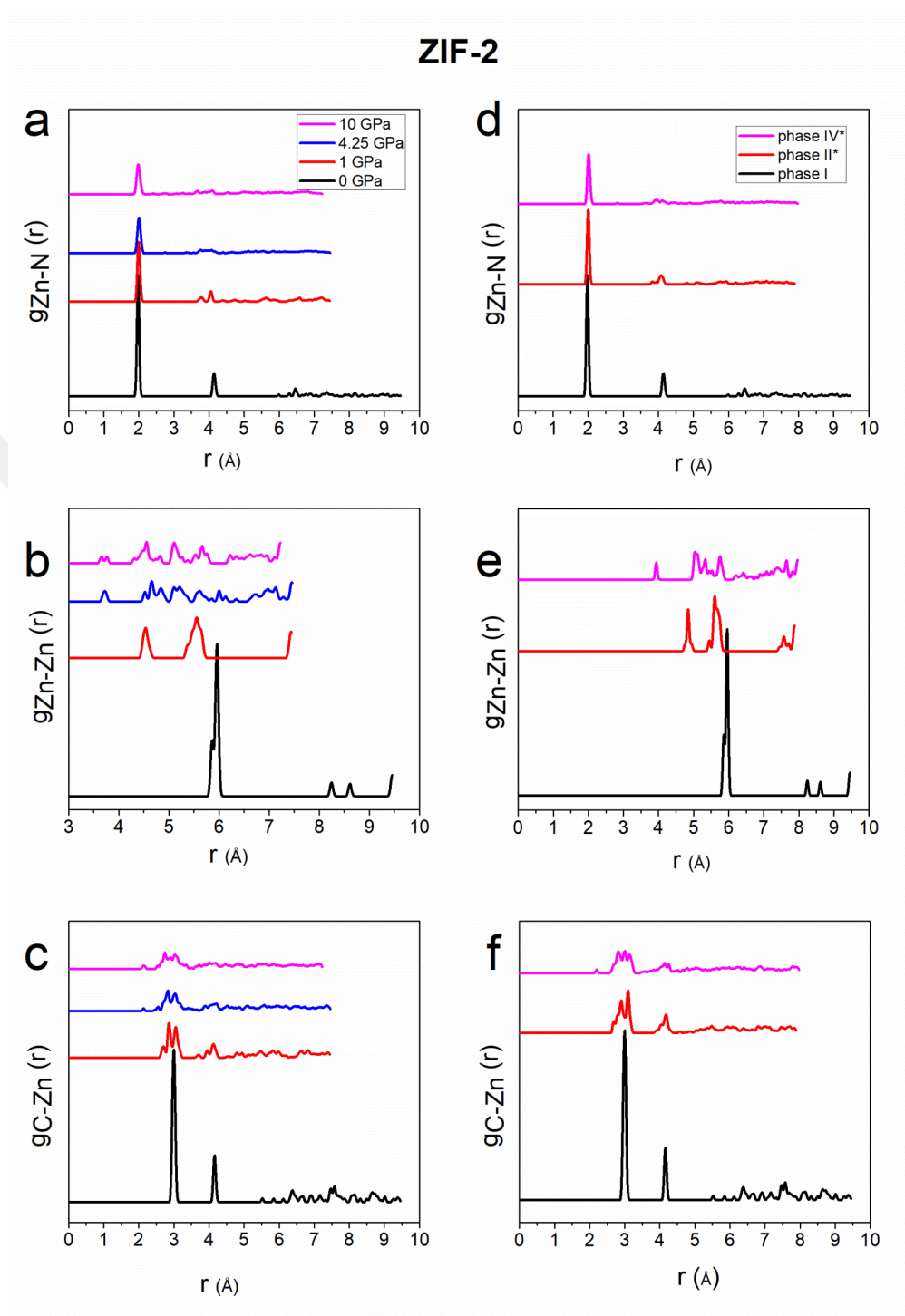
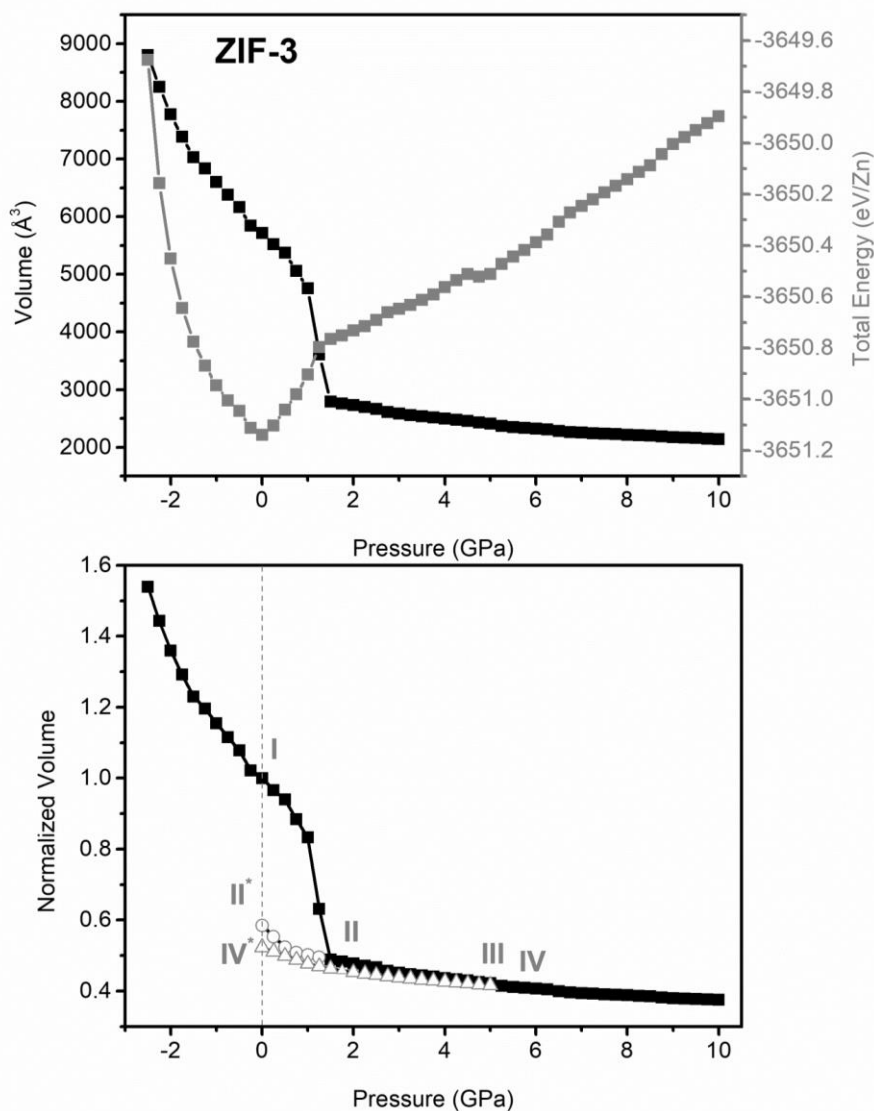


Figure 5.7 Partial pair distribution functions (PDFs) data for structures formed at 0-10 GPa pressure range for ZIF-2

ZIF-3 Figure 5.8a shows the unit cell volume and total energy/Zn of the system as a function of pressure. Phase I is the equilibrium structure, which has the

minimum energy configuration at 0 GPa. We obtained $d_{\text{Zn-N}} = 1.990 \pm 0.031 \text{ \AA}$, $\theta_{\text{N-Zn-N}} = 109 \pm 4^\circ$, and $\theta_{\text{Zn-N-C}} = 126 \pm 3^\circ$ for this structure. Up to 1 GPa, the volume continuously decreases and the energy increases. At 1.5 GPa, we observe a first-order transition into phase II. The decrease in the volume in this stage is around %52 compared to the equilibrium volume. Phase II at 1.5 GPa is characterized by $d_{\text{Zn-N}} = 1.968 \pm 0.030 \text{ \AA}$, $\theta_{\text{N-Zn-N}} = 108 \pm 11^\circ$, and $\theta_{\text{Zn-N-C}} = 125 \pm 7^\circ$. During the transition, CN of Zn reduced to 3.67, 8MRs collapse, Zn_4 tetrahedra is distorted and the crystallinity is lost. The results points out likelihood that the transition to phase II at 1.5 GPa is a crystal-amorphous phase transition.

No phase change is observed between 1.5 and 5 GPa, where while the volume decreases, the total energy increases gradually. For phase III we obtained $d_{\text{Zn-N}} = 2.000 \pm 0.045 \text{ \AA}$, $\theta_{\text{N-Zn-N}} = 106 \pm 19^\circ$, and $\theta_{\text{Zn-N-C}} = 124 \pm 6^\circ$. The CN of Zn reduced to 3.34 at 5 GPa. Both volume and energy show a small discontinuity at 5.25, which might denote a first-order like phase transition -an amorphous-amorphous, or it may be attributed to the small size of simulation box. For phase IV at 5.25 GPa, we found $d_{\text{Zn-N}} = 2.001 \pm 0.045 \text{ \AA}$, $\theta_{\text{N-Zn-N}} = 106 \pm 19^\circ$, and $\theta_{\text{Zn-N-C}} = 124 \pm 7^\circ$. Beyond this pressure, the volume continues to decrease gradually. In tension range, the volume gradually increases up to -2.5 GPa. At 2.75 a structural failure was observed for ZIF-3. As shown in Figure 5.8b, all transitions are irreversible in ZIF-3. Upon decompression from 1.5 GPa, the structure recovers approximately 25% of its original volume. Phase II* is characterized by $d_{\text{Zn-N}} = 2.002 \pm 0.037 \text{ \AA}$, $\theta_{\text{N-Zn-N}} = 108 \pm 10^\circ$, and $\theta_{\text{Zn-N-C}} = 124 \pm 8^\circ$. In comparison to phase II*, phase IV* has structurally more distorted Zn_4 tetrahedra and longer Zn-N distance. For phase IV* we obtained $d_{\text{Zn-N}} = 2.011 \pm 0.040 \text{ \AA}$, $\theta_{\text{N-Zn-N}} = 107 \pm 19^\circ$, and $\theta_{\text{Zn-N-C}} = 124 \pm 7^\circ$. It is crucial to note that the increase in the average Zn-N distance indicates the existence of high-coordination defects, which is also confirmed by CN analysis.



**Figure 5.8 a) The volume and total energy per Zn plot as a function of pressure for ZIF-3
b) Normalized volume as a function of pressure for ZIF-3.**

The total and partial PDFs of ZIF-3 and its high pressure phases are shown in Figure 5.9 and 5.10. Obviously, the total PDF of phase II and the equilibrium structure show some similarities, but there is broadening in the peaks beyond 3 \AA in PDF of phase II. The PDFs of high pressure phases –phase IV and the structure at 10 GPa- are continuous form beyond 3 \AA . The peaks of $g_{\text{Zn-N}}(r)$ are observed at even higher pressures, but the peak's intensity decreases and the

peaks transform to broader one. With the further increase in pressure, the total PDFs become continuous, indicating the diminishing of long-range order.

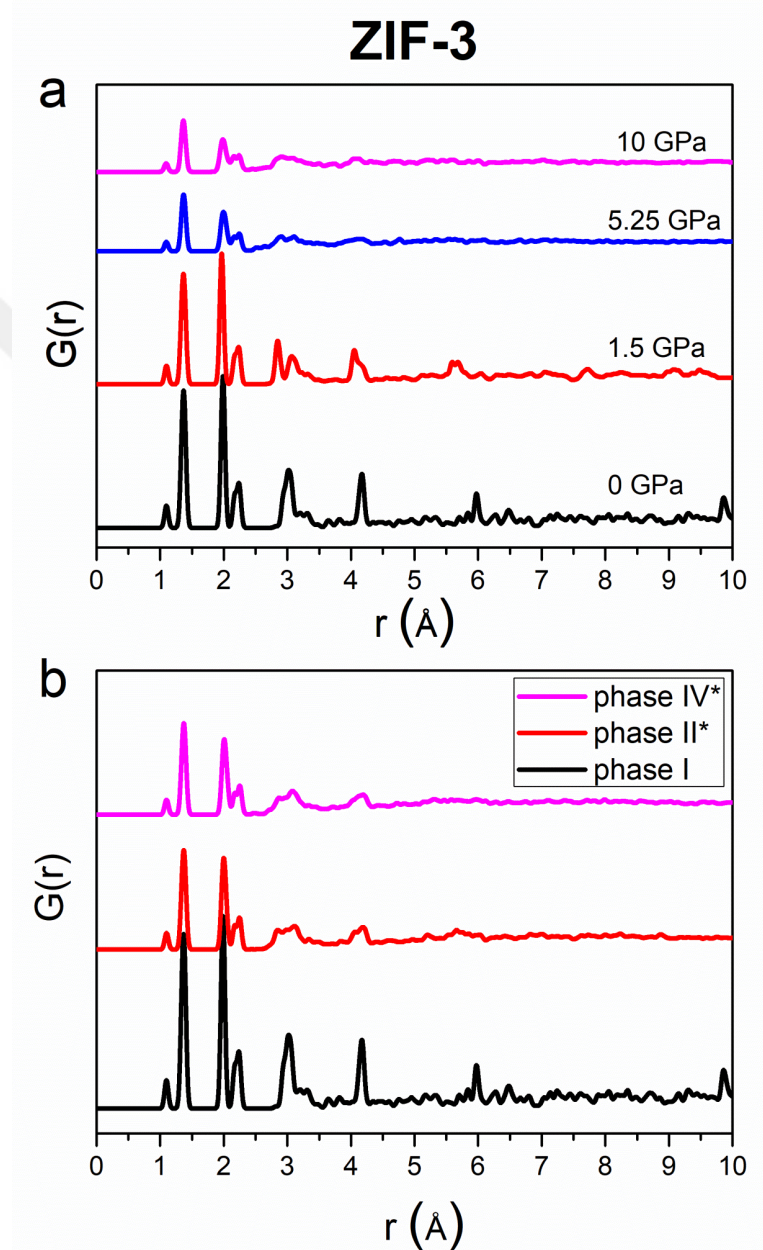


Figure 5.9 Total pair distribution functions (PDFs) data for structures formed at 0-10 GP pressure range for ZIF-3

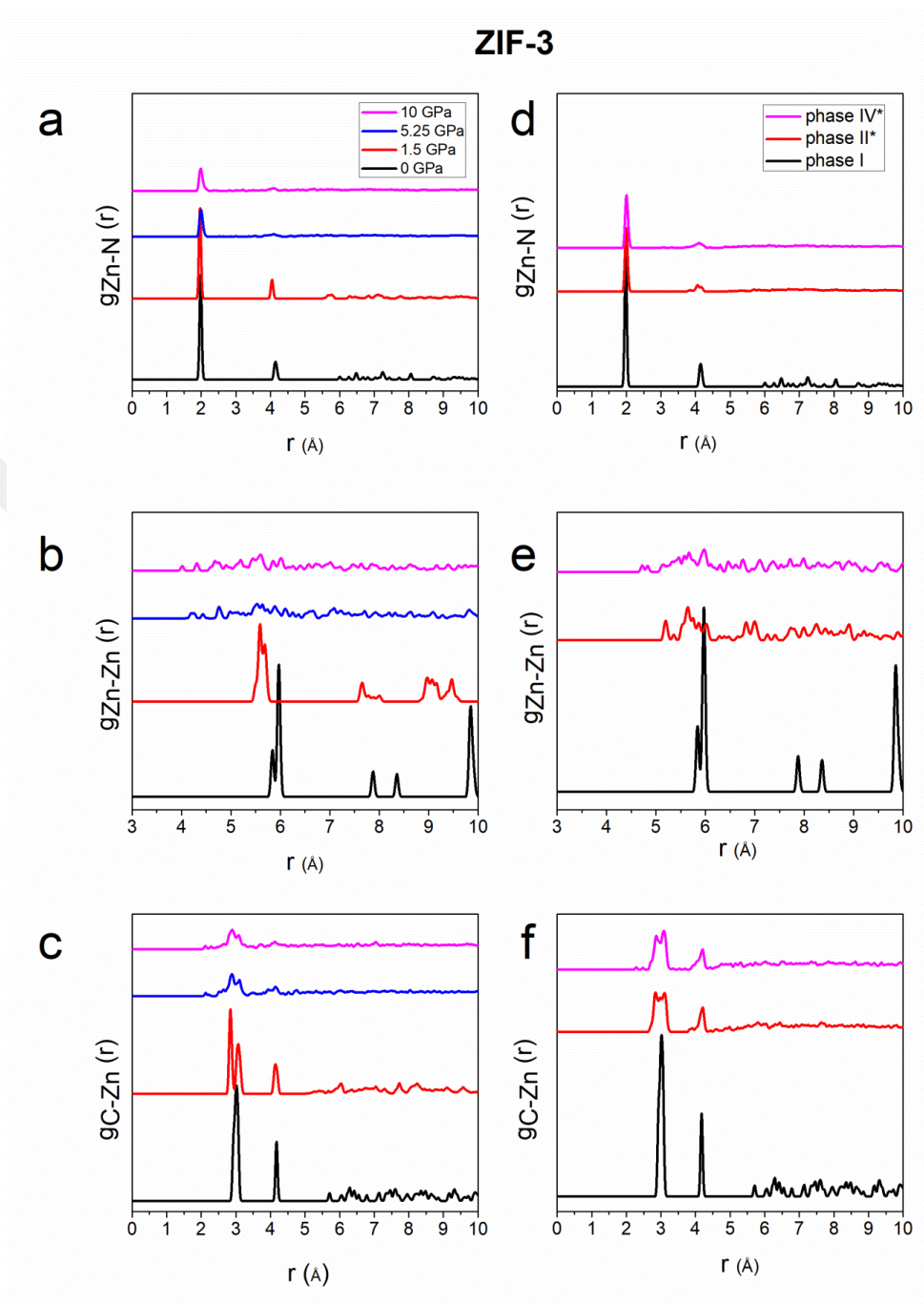


Figure 5.10 Partial pair distribution functions (PDFs) data for structures formed at 0-10 GP pressure range for ZIF-3

The electronic structures for three ZIFs and their high pressure phases were calculated. The partial density of states (PDOS) and the total density of states (TDOS) are shown in Figure 5.11-13. All phases have similar features in their

DOS curves. In general, the energy bands between -18 and -10 are formed by 1s electronic state of H and 2s electronic states of N and C atoms. From -7.5 eV to -2.5, hybridizations between 1s-state of H, 2s-, 2p-states of N and C and 3d state of Zn indicate the covalent bonds on imidazole rings and coordination bonds between Zn and N. The sharp peak in the lower part of conduction band (CB) is ascribed to hybridization of 2p-states of N and C atoms. In contrast to discontinuous structure of valence band (VB), the CB has a continuous form. The valence band maxima (VBM) and the conduction band minima (CBM) for all phases are dominated by imidazolate. The predicted band gaps for all phases indicate that both crystal and amorphous phases are insulators. We are aware that these calculated band gaps are inevitably underestimated due to the shortcomings of GGA-DFT calculations. It is well known that the band gap can be reliably predicted by using hybrid density functionals, such as the Heyd–Scuseria–Ernzerhof (HSE)[161] formulation. Yet, the calculations with hybrid functionals are very onerous and time-consuming for complex amorphous ZIFs, even crystalline frameworks with many atoms. Despite the limitations of GGA method, and consequently underestimated band gaps, our findings do however suggest that there is a band gap narrowing trend during the crystal-amorphous transitions. For example, while the predicted band gaps for ZIF-1, ZIF-2, ZIF-3 are 4.15, 4.10 and 4.56 eV, for their amorphous phases are 3.83, 3.72 and 3.40 eV, respectively.

Butler and co-workers [55] systematically investigate the electronic structures of some ZIFs. They reach the conclusion that electronic conduction in ZIFs is mediated by hopping mechanism and its efficacy highly depends on the interaction of the linker and metal. For crystalline ZIFs, the weak overlap between d-orbitals of Zn and sp^2 hybridized orbitals of N results in a wide gap formation. In amorphous phases of ZIFs, presumably, the strong distortions on tetrahedral units and densification in the framework may increase the Zn-N interactions, contributing to a decrease in band gap. Nonetheless, they are still insulators. The most important reason for this is that the electronic structure of the ZIFs is mostly controlled by the imidazolate anion, as can be seen from

PDOS plots, so conductivity is only achieved by the hopping mechanism. However, as reported in Chapter 3, the band gap of MOF-5 significantly decreases with a crystal-amorphous transition since the densification provides an enhancement in conductivity by π -stacking.

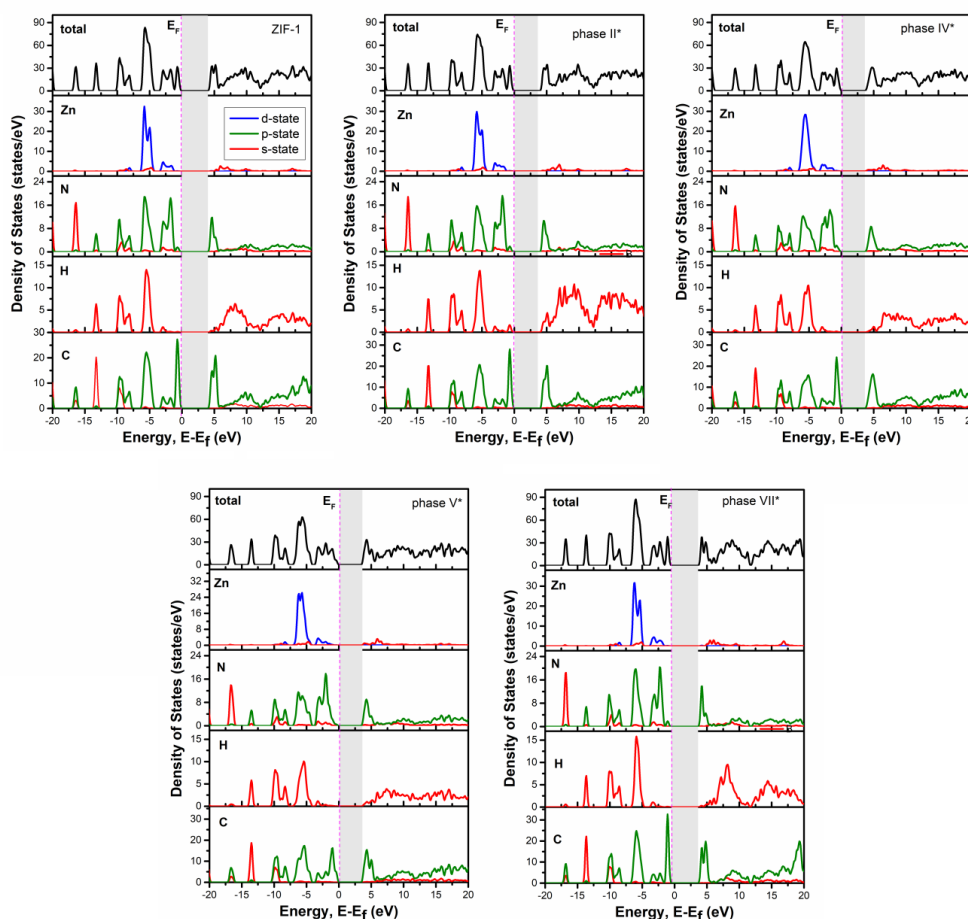


Figure 5.11 Calculated total and partial density of states (DOS) for ZIF-1

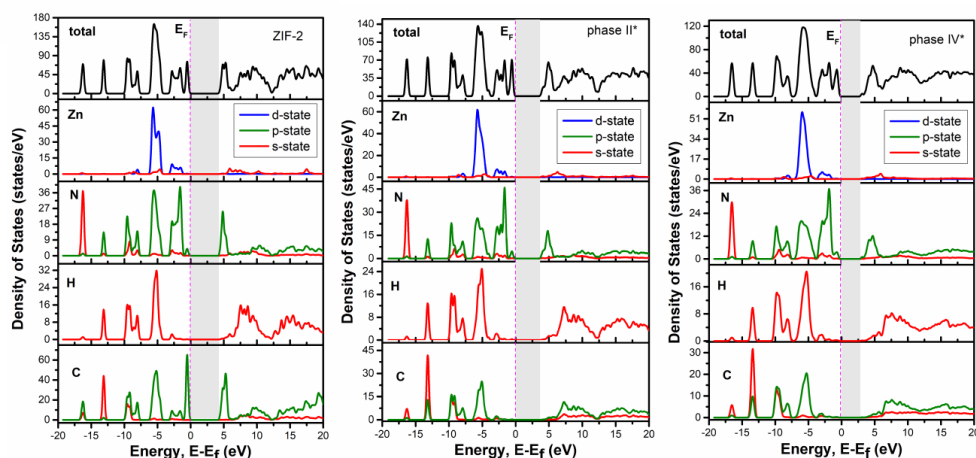


Figure 5.12 Calculated total and partial density of states (DOS) for ZIF-2

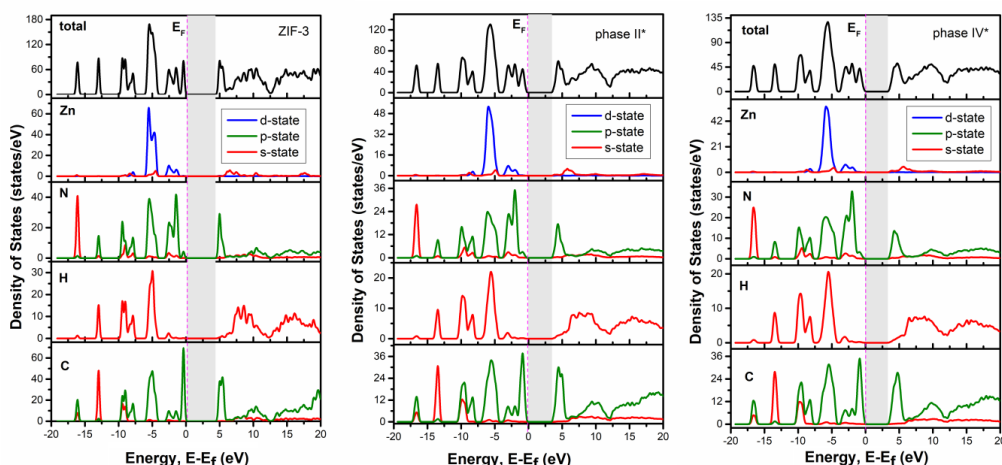


Figure 5.13 Calculated total and partial density of states (DOS) for ZIF-3

5.4 Conclusion

We explored the high pressure behaviors of three structurally polymorphic ZIFs by using AIMD simulations. According to our results, ZIF-1 shows some consecutive crystal-crystal and crystal-amorphous phase transition between -2 GPa (tension) and 10 GPa (compression). On the other hand, ZIF-2 and ZIF-3 have very similar pressure-volume behavior in both tension and compression

regions. In compression region, a rapid crystal-amorphous at relatively lower compression pressure and a most likely an amorphous-amorphous transitions were explored whereas the structural failure was observed at around -3 GPa for all ZIFs. The underlying mechanism triggering these phase transitions might be distortions in the tetrahedral units and the structural rearrangement of the imidazolate linker in the frameworks due to the free rotation ability under pressure.



Chapter 6

Conclusions and Future Prospects

6.1 Conclusions

In this thesis, we applied AIMD simulations to study the pressure-induced phase transitions in selected metal-organic frameworks (MOFs). The SIESTA code has been used to generate simulation conditions on the frameworks and calculating their properties.

In chapter 3, we presented the pressure-induced amorphization in MOF-5. We successfully observed a crystal-amorphous phase transition at 2GPa. The main findings indicate that the origin of phase transition was due to the local distortions through the framework, and it did not involve with any bond breaking and/or formation. Furthermore, the results revealed that electronic properties of the crystalline MOF-5 were considerably different than the amorphous phase. Namely, a band gap narrowing from 2.5 eV to 1.5 eV was observed by the crystal-amorphous phase transition.

In chapter 4, we showed the pressure-induced amorphization of ZIF-8, and its mechanical and electronic properties. The Parinello-Rahman algorithm appears to be very successful in reproducing experimentally observed the crystal-crystal and the crystal-amorphous transitions. The overestimated critical pressures could be ascribed to the simulation conditions, such as lack of surface effects due to the periodic boundary conditions, non-defective structure etc. All mechanical properties of ZIF-8 were accurately estimated by using two different approaches, and interestingly like compact bones, different compression and tensile strengths were proposed for the crystalline framework. The electronic properties of ZIFs are mostly governed by imidazolate linkers. Since the

imidazolate retained its structural integrity, the crystal-amorphous phase transformation did not have significant impact on the electronic properties of ZIF-8.

In chapter 5, we explored the high pressure behaviors of three structurally polymorphic ZIFs by using AIMD. According to our results, ZIF-1 shows some consecutive crystal-crystal and crystal-amorphous phase transitions between -2 GPa (tension) and 10 GPa (compression). On the other hand, ZIF-2 and ZIF-3 have very similar pressure-volume relation in both tension and compression regions. During compression, rapid crystal-amorphous and amorphous-amorphous transitions were explored whereas the structural failure was observed at around -3 GPa for all ZIFs.

Overall, in this dissertation, pressure induced phase transitions of 5 different MOFs in both compression and tensile regimes were investigated by AIMD simulations. Our findings expose many undiscovered properties offered by the field of solid state amorphization in MOFs, and the stimulate possibilities that it can rouse to basic science and practical engineering. We hope that the detailed data on the high-pressure behavior, structural and electronic properties of the frameworks reported herein will be advantageous to guide the future research, design and manufacturing of amorphous MOFs.

6.2 Challenges and future outlook

There are some challenges of determining the mechanical properties and amorphization pressure of MOFs. Among them, the most well-known issue is that DAC experiments cannot give reliable results due to the porous structure of MOFs. However, as DAC experiments without PTM cannot produce a real hydrostatic pressure medium, and the results can still be unreliable. AIMD simulation techniques are a valid method to model the true behavior of MOFs under pressure, as well as to elucidate the atomic structures of the resulting high pressure phases. The results obtained in this study also confirm this postulation.

Despite the limitations of the number of atoms in the simulation cell and time scale of MD simulation, this dissertation is the one of the first steps towards enhancing our understanding of phase transitions in MOFs. Our findings are reliable and provide important opportunities.

For example, as we shown in chapter 3, amorphization causes a significant narrowing in the electronic band gap of certain MOFs. From this point of view, we believe that some amorphous MOFs can be a promising material for electronic applications. Also electronically, amorphous ZIFs can be used as dielectric materials in many applications due to their insulating properties.

Another possible application of crystalline-amorphous transitions in MOFs is trapping harmful guest molecules in the framework. In such an embodiment, the harmful guest molecule is introduced into crystal MOF by adsorption, and then MOF is amorphized, providing the trapping of the molecule in the pores. One of the most critical parameters of this application, which can be used for the storage of nuclear waste, is to know the amorphization pressure of the MOF. Therefore, we believe that the results obtained in this study will be useful at this stage. Additionally, the phase transitions in MOFs can be attractive for variety of piezoresponsive applications such as pressure sensors, pressure switches and shock absorbing materials. For gas storage applications, densification MOF is of great interest, but pressure induced structural changes is lacking. The present findings might also prove beneficial to those studying the processing and shaping MOF powders.

Considering both the above limitations and our findings, we are confident that studies on amorphous MOFs will continue to increase rapidly over the next few years.

BIBLIOGRAPHY

- [1] Z.H. Stachurski, *Fundamentals of Amorphous Solids*, 1 ed., Wiley-VCH2015.
- [2] R. Manaila, D. Macovei, Exafs in Amorphous Materials, *J Non-Cryst Solids* 90(1-3) (1987) 383-392.
- [3] Y. Cros, D. Jousse, J. Liu, J.C. Rostaing, Ir, Electron-Spin-Resonance and Resistivity Measurements on Amorphous-Silicon Oxi-Nitride Films Prepared by Pecvd at Low-Temperature, *J Non-Cryst Solids* 90(1-3) (1987) 287-290.
- [4] G. Suran, P. Gerard, Electron-Spin-Resonance Measurements on Amorphous Fenisi Thin-Films in the Ferromagnetic-Spin Glass-Transition Regime, *J Appl Phys* 55(6) (1984) 1682-1684.
- [5] L. Kubler, R. Haug, F. Ringeisen, A. Jaegle, Xps, Electron-Spin-Resonance and Resistivity Measurements on Amorphous-Silicon Oxynitride Films (a-Sioxny) Prepared by Reactive Evaporation of Si in Presence of No2, *J Non-Cryst Solids* 54(1-2) (1983) 27-42.
- [6] D.K. Biegelsen, Electron-Spin Resonance Measurements on Amorphous-Silicon, *Sol Cells* 2(4) (1980) 421-430.
- [7] X.Y. Lu, W. Xu, M. Hanada, S.V. Jermain, R.O. Williams, Y.C. Su, Solid-state NMR analysis of crystalline and amorphous Indomethacin: An experimental protocol for full resonance assignments, *J Pharmaceut Biomed* 165 (2019) 47-55.
- [8] J. Sanz, *Nmr Techniques for the Study of Crystalline and Amorphous Solids*, *Nato Adv Sci Inst Se* 418 (1994) 157-188.
- [9] S.K. Lee, P.J. Eng, H.K. Mao, Probing of Pressure-Induced Bonding Transitions in Crystalline and Amorphous Earth Materials: Insights from X-ray Raman Scattering at High Pressure, *Rev Mineral Geochem* 78 (2014) 139-174.
- [10] A. Boukenter, E. Duval, H.M. Rosenberg, Raman-Scattering in Amorphous and Crystalline Materials - a Study of Epoxy-Resin and Dgeba, *J Phys C Solid State* 21(15) (1988) L541-L547.
- [11] J.S. Lannin, P.J. Carroll, 2nd-Order Raman-Scattering in Non-Crystalline Materials - Amorphous Se, *Philos Mag B* 45(2) (1982) 155-165.
- [12] S.R. Elliott, *Physics of Amorphous Materials*, 1 ed., Longman1984.
- [13] O.M. Yaghi, G.M. Li, H.L. Li, Selective Binding and Removal of Guests in a Microporous Metal-Organic Framework, *Nature* 378(6558) (1995) 703-706.
- [14] U. Nations, *Sustainable Development Goals*, 2015. <https://www.un.org/sustainabledevelopment/sustainable-development-goals/>.
- [15] H. Kim, S. Yang, S.R. Rao, S. Narayanan, E.A. Kapustin, H. Furukawa, A.S. Umans, O.M. Yaghi, E.N. Wang, Water harvesting from air with metal-organic frameworks powered by natural sunlight, *Science* 356(6336) (2017) 430-432.
- [16] H.L. Wang, Q.L. Zhu, R.Q. Zou, Q. Xu, Metal-Organic Frameworks for Energy Applications, *Chem-Us* 2(1) (2017) 52-80.

- [17] P.A. Kobielska, A.J. Howarth, O.K. Farha, S. Nayak, Metal-organic frameworks for heavy metal removal from water, *Coord Chem Rev* 358 (2018) 92-107.
- [18] N.C. Burtch, J. Heinen, T.D. Bennett, D. Dubbeldam, M.D. Allendorf, Mechanical Properties in Metal-Organic Frameworks: Emerging Opportunities and Challenges for Device Functionality and Technological Applications, *Adv Mater* 30(37) (2018).
- [19] T.D. Bennett, A.K. Cheetham, Amorphous Metal-Organic Frameworks, *Accounts Chem Res* 47(5) (2014) 1555-1562.
- [20] Wikipedia, Amorphous Solids, 2019. https://en.wikipedia.org/wiki/Amorphous_solid. (Accessed 10.11 2019).
- [21] J.E. Shelby, Introduction to Glass Science and Technology, Second ed., RSC2005.
- [22] E.G. Ponyatovsky, O.I. Barkalov, Pressure-Induced Amorphous Phases, *Mater Sci Rep* 8(4) (1992) 147-191.
- [23] A.G. Lyapin, V.V. Brazhkin, Pressure-induced lattice instability and solid-state amorphization, *Phys Rev B* 54(17) (1996) 12036-12048.
- [24] S.M. Sharma, S.K. Sikka, Pressure induced amorphization of materials, *Prog Mater Sci* 40(1) (1996) 1-77.
- [25] S.K. Sikka, S.M. Sharma, Close Packing and Pressure-Induced Amorphization, *Curr Sci India* 63(6) (1992) 317-320.
- [26] W.S. Hammack, G.C. Serghiou, R.R. Winters, Reversible Pressure-Induced Amorphizations, *Physics of Non-Crystalline Solids* (1992) 208-212.
- [27] O. Mishima, L.D. Calvert, E. Whalley, Melting Ice-I at 77-K and 10-Kbar - a New Method of Making Amorphous Solids, *Nature* 310(5976) (1984) 393-395.
- [28] G.S. Bordonskii, S.D. Krylov, Amorphization of ice under mechanical stresses, *Tech Phys Lett* 43(11) (2017) 983-986.
- [29] P.K. Nandi, C.J. Burnham, Z. Futera, N.J. English, Ice-Amorphization of Supercooled Water Nanodroplets in No Man's Land, *Acs Earth Space Chem* 1(4) (2017) 187-196.
- [30] M.A. Salim, S.Y. Willow, S. Hirata, Ice Ih anomalies: Thermal contraction, anomalous volume isotope effect, and pressure-induced amorphization, *J Chem Phys* 144(20) (2016).
- [31] J.S. Tse, D.D. Klug, C.A. Tulk, I. Swainson, E.C. Svensson, C.K. Loong, V. Shpakov, V.R. Belosludov, R.V. Belosludov, Y. Kawazoe, The mechanisms for pressure-induced amorphization of ice I-h, *Nature* 400(6745) (1999) 647-649.
- [32] O.V. Stalgorova, E.L. Gromnitskaya, V.V. Brazhkin, Experimental Confirmation of the Instability of the Crystal-Structure of Ih Ice Prior to Amorphization under Pressure, *Jetp Lett* 62(4) (1995) 356-360.
- [33] J.S. Tse, Mechanical Instability in Ice Ih - a Mechanism for Pressure-Induced Amorphization, *J Chem Phys* 96(7) (1992) 5482-5487.
- [34] G. Strazzulla, G.A. Baratta, G. Leto, G. Foti, Ion-Beam Induced Amorphization of Crystalline Water Ice, *Europhys Lett* 18(6) (1992) 517-522.

- [35] J.S. Tse, M.L. Klein, Pressure-Induced Amorphization of Ice I-H, *J Chem Phys* 92(6) (1990) 3992-3994.
- [36] A. Kouchi, T. Kuroda, Amorphization of Cubic Ice by Ultraviolet-Irradiation, *Nature* 344(6262) (1990) 134-135.
- [37] E. Whalley, Amorphization of Ice Ih by Pressure at 77-K, *J Less-Common Met* 140 (1988) 361-373.
- [38] N. Binggeli, J.R. Chelikowsky, Elastic Instability in Alpha-Quartz under Pressure, *Phys Rev Lett* 69(15) (1992) 2220-2223.
- [39] K.J. Kingma, C. Meade, R.J. Hemley, H.K. Mao, D.R. Veblen, Microstructural Observations of Alpha-Quartz Amorphization, *Science* 259(5095) (1993) 666-669.
- [40] K.H. Smith, E. Shero, A. Chizmeshya, G.H. Wolf, The Equation of State of Polyamorphic Germania Glass - a 2-Domain Description of the Viscoelastic Response, *J Chem Phys* 102(17) (1995) 6851-6857.
- [41] V. Domnich, S. Reynaud, R.A. Haber, M. Chhowalla, Boron Carbide: Structure, Properties, and Stability under Stress, *J Am Ceram Soc* 94(11) (2011) 3605-3628.
- [42] R.M. Wentzcovitch, C. da Silva, J.R. Chelikowsky, N. Binggeli, A new phase and pressure induced amorphization in silica, *Phys Rev Lett* 80(10) (1998) 2149-2152.
- [43] R.R. Winters, G.C. Serghiou, W.S. Hammack, Observation and Explanation of the Reversible Pressure-Induced Amorphization of $\text{Ca}(\text{NO}_3)_2/\text{Nano}_3$, *Phys Rev B* 46(5) (1992) 2792-2797.
- [44] W.L. Johnson, Crystal-to-Glass Transformation in Metallic Materials, *Mater Sci Eng* 97 (1988) 1-13.
- [45] W.L. Johnson, Thermodynamic and Kinetic Aspects of the Crystal to Glass Transformation in Metallic Materials, *Prog Mater Sci* 30(2) (1986) 81-134.
- [46] H. Furukawa, K.E. Cordova, M. O'Keeffe, O.M. Yaghi, The Chemistry and Applications of Metal-Organic Frameworks, *Science* 341(6149) (2013) 974-+.
- [47] K.K. Tanabe, S.M. Cohen, Postsynthetic modification of metal-organic frameworks-a progress report, *Chem Soc Rev* 40(2) (2011) 498-519.
- [48] X. Zhao, Y.X. Wang, D.S. Li, X.H. Bu, P.Y. Feng, Metal-Organic Frameworks for Separation, *Adv Mater* 30(37) (2018).
- [49] M.X. Wu, Y.W. Yang, Metal-Organic Framework (MOF)-Based Drug/Cargo Delivery and Cancer Therapy, *Adv Mater* 29(23) (2017).
- [50] Y. Liu, X.Y. Xie, C. Cheng, Z.S. Shao, H.S. Wang, Strategies to fabricate metal-organic framework (MOF)-based luminescent sensing platforms, *J Mater Chem C* 7(35) (2019) 10743-10763.
- [51] A. Dhakshinamoorthy, Z.H. Li, H. Garcia, Catalysis and photocatalysis by metal organic frameworks, *Chem Soc Rev* 47(22) (2018) 8134-8172.
- [52] Y.Q. Ren, G.H. Chia, Z.Q. Gao, Metal-organic frameworks in fuel cell technologies, *Nano Today* 8(6) (2013) 577-597.
- [53] J.P. Zhu, X.H. Wang, X.X. Zuo, The application of metal-organic frameworks in electrode materials for lithium-ion and lithium-sulfur batteries, *Roy Soc Open Sci* 6(7) (2019).

- [54] W.B. Lin, Metal-organic framework materials for solar energy applications, *Abstr Pap Am Chem S* 249 (2015).
- [55] K.T. Butler, S.D. Worrall, C.D. Molloy, C.H. Hendon, M.P. Atfield, R.A.W. Dryfe, A. Walsh, Electronic structure design for nanoporous, electrically conductive zeolitic imidazolate frameworks, *J Mater Chem C* 5(31) (2017) 7726-7731.
- [56] L. Jiao, J.Y.R. Seow, W.S. Skinner, Z.U. Wang, H.L. Jiang, Metal-organic frameworks: Structures and functional applications, *Mater Today* 27 (2019) 43-68.
- [57] G. Ayoub, B. Karadeniz, A.J. Howarth, O.K. Farha, I. Dilovic, L.S. Germann, R.E. Dinnebier, K. Uzarevic, T. Friscic, Rational Synthesis of Mixed-Metal Microporous Metal-Organic Frameworks with Controlled Composition Using Mechanochemistry, *Chem Mater* 31(15) (2019) 5494-5501.
- [58] W. Zhang, J. Maul, D. Vulpe, P.Z. Moghadam, D. Fairen-Jimenez, D.M. Mittleman, J.A. Zeitler, A. Erba, M.T. Ruggiero, Probing the Mechanochemistry of Metal-Organic Frameworks with Low-Frequency Vibrational Spectroscopy, *J Phys Chem C* 122(48) (2018) 27442-27450.
- [59] B. Karadeniz, A.J. Howarth, T. Stolar, T. Islamoglu, I. Dejanovic, M. Tireli, M.C. Wasson, S.Y. Moon, O.K. Farha, T. Friscic, K. Uzarevic, Benign by Design: Green and Scalable Synthesis of Zirconium UiO-Metal-Organic Frameworks by Water-Assisted Mechanochemistry, *Acs Sustain Chem Eng* 6(11) (2018) 15841-15849.
- [60] T. Friscic, Understanding of Metal-Organic Frameworks through Mechanochemistry: From Experiment to Theory, *Acta Crystallogr A* 74 (2018) A422-A422.
- [61] G. Ayoub, K. Uzarevic, A. Howarth, L. Germann, R. Dinnebier, O. Farha, T. Friscic, Mechanochemistry enables a rational, targeted synthesis of mixed-metal microporous metal-organic frameworks, *Abstr Pap Am Chem S* 255 (2018).
- [62] K. Uzarevic, N. Ferdelji, T. Mrla, P.A. Julien, B. Halasz, T. Friscic, I. Halasz, Enthalpy vs. friction: heat flow modelling of unexpected temperature profiles in mechanochemistry of metal-organic frameworks, *Chem Sci* 9(9) (2018) 2525-2532.
- [63] V. Andre, S. Quaresma, J.L.F. da Silva, M.T. Duarte, Exploring mechanochemistry to turn organic bio-relevant molecules into metal-organic frameworks: a short review, *Beilstein J Org Chem* 13 (2017) 2416-2427.
- [64] H. Ali-Moussa, R.N. Amador, J. Martinez, F. Lamaty, M. Carboni, X. Bantreil, Synthesis and post-synthetic modification of UiO-67 type metal-organic frameworks by mechanochemistry, *Mater Lett* 197 (2017) 171-174.
- [65] S. Quaresma, V. Andre, A. Fernandes, M.T. Duarte, Mechanochemistry - A green synthetic methodology leading to metallodrugs, metallopharmaceuticals and bio-inspired metal-organic frameworks, *Inorg Chim Acta* 455 (2017) 309-318.
- [66] T. Friscic, Mechanochemistry: An excellent approach to bulk, clean and high-yielding synthesis of metal-organic frameworks, *Abstr Pap Am Chem S* 250 (2015).

- [67] T. Friscic, I. Halasz, V. Strukil, M. Eckert-Maksic, R.E. Dinnebier, Clean and Efficient Synthesis Using Mechanochemistry: Coordination Polymers, Metal-Organic Frameworks and Metallo-drugs, *Croat Chem Acta* 85(3) (2012) 367-378.
- [68] T. Friscic, Supramolecular concepts and new techniques in mechanochemistry: cocrystals, cages, rotaxanes, open metal-organic frameworks, *Chem Soc Rev* 41(9) (2012) 3493-3510.
- [69] J. Stojakovic, B.S. Farris, L.R. MacGillivray, Vortex grinding for mechanochemistry: application for automated supramolecular catalysis and preparation of a metal-organic framework, *Chem Commun* 48(64) (2012) 7958-7960.
- [70] S. Cao, T.D. Bennett, D.A. Keen, A.L. Goodwin, A.K. Cheetham, Amorphization of the prototypical zeolitic imidazolate framework ZIF-8 by ball-milling, *Chem Commun* 48(63) (2012) 7805-7807.
- [71] A.U. Ortiz, A. Boutin, A.H. Fuchs, F.X. Coudert, Investigating the Pressure-Induced Amorphization of Zeolitic Imidazolate Framework ZIF-8: Mechanical Instability Due to Shear Mode Softening, *J Phys Chem Lett* 4(11) (2013) 1861-1865.
- [72] J.C. Tan, T.D. Bennett, A.K. Cheetham, Chemical structure, network topology, and porosity effects on the mechanical properties of Zeolitic Imidazolate Frameworks, *P Natl Acad Sci USA* 107(22) (2010) 9938-9943.
- [73] T.D. Bennett, P. Simoncic, S.A. Moggach, F. Gozzo, P. Macchi, D.A. Keen, J.C. Tan, A.K. Cheetham, Reversible pressure-induced amorphization of a zeolitic imidazolate framework (ZIF-4), *Chem Commun* 47(28) (2011) 7983-7985.
- [74] T.D. Bennett, T.K. Todorova, E.F. Baxter, D.G. Reid, C. Gervais, B. Bueken, B. Van de Voorde, D. De Vos, D.A. Keen, C. Mellot-Draznieks, Connecting defects and amorphization in UiO-66 and MIL-140 metal-organic frameworks: a combined experimental and computational study, *Phys Chem Chem Phys* 18(3) (2016) 2192-2201.
- [75] T.D. Bennett, P.J. Saines, D.A. Keen, J.C. Tan, A.K. Cheetham, Ball-Milling-Induced Amorphization of Zeolitic Imidazolate Frameworks (ZIFs) for the Irreversible Trapping of Iodine, *Chem-Eur J* 19(22) (2013) 7049-7055.
- [76] C. Orellana-Tavra, E.F. Baxter, T. Tian, T.D. Bennett, N.K.H. Slater, A.K. Cheetham, D. Fairen-Jimenez, Amorphous metal-organic frameworks for drug delivery, *Chem Commun* 51(73) (2015) 13878-13881.
- [77] Y.H. Hu, L. Zhang, Amorphization of metal-organic framework MOF-5 at unusually low applied pressure, *Phys Rev B* 81(17) (2010).
- [78] Z. Su, Y.R. Miao, G.H. Zhang, J.T. Miller, K.S. Suslick, Bond breakage under pressure in a metal organic framework, *Chem Sci* 8(12) (2017) 8004-8011.
- [79] S.A. Moggach, T.D. Bennett, A.K. Cheetham, The Effect of Pressure on ZIF-8: Increasing Pore Size with Pressure and the Formation of a High-Pressure Phase at 1.47 GPa, *Angew Chem Int Edit* 48(38) (2009) 7087-7089.

- [80] K.W. Chapman, G.J. Halder, P.J. Chupas, Pressure-Induced Amorphization and Porosity Modification in a Metal-Organic Framework, *J Am Chem Soc* 131(48) (2009) 17546-17547.
- [81] Y. Hu, H. Kazemian, S. Rohani, Y.N. Huang, Y. Song, In situ high pressure study of ZIF-8 by FTIR spectroscopy, *Chem Commun* 47(47) (2011) 12694-12696.
- [82] A.J. Graham, D.R. Allan, A. Muszkiewicz, C.A. Morrison, S.A. Moggach, The Effect of High Pressure on MOF-5: Guest-Induced Modification of Pore Size and Content at High Pressure, *Angew Chem Int Edit* 50(47) (2011) 11138-11141.
- [83] K.W. Chapman, D.F. Sava, G.J. Halder, P.J. Chupas, T.M. Nenoff, Trapping Guests within a Nanoporous Metal-Organic Framework through Pressure-Induced Amorphization, *J Am Chem Soc* 133(46) (2011) 18583-18585.
- [84] K.J. Gagnon, C.M. Beavers, A. Clearfield, MOFs Under Pressure: The Reversible Compression of a Single Crystal, *J Am Chem Soc* 135(4) (2013) 1252-1255.
- [85] Z. Su, Y.R. Miao, S.M. Mao, G.H. Zhang, S. Dillon, J.T. Miller, K.S. Suslick, Compression-Induced Deformation of Individual Metal-Organic Framework Microcrystals, *J Am Chem Soc* 137(5) (2015) 1750-1753.
- [86] T.D. Bennett, S. Cao, J.C. Tan, D.A. Keen, E.G. Bithell, P.J. Beldon, T. Friscic, A.K. Cheetham, Facile Mechanochemistry of Amorphous Zeolitic Imidazolate Frameworks, *J Am Chem Soc* 133(37) (2011) 14546-14549.
- [87] P. Zhao, T.D. Bennett, N.P.M. Casati, G.I. Lampronti, S.A. Moggach, S.A.T. Redfern, Pressure-induced oversaturation and phase transition in zeolitic imidazolate frameworks with remarkable mechanical stability, *Dalton T* 44(10) (2015) 4498-4503.
- [88] R.N. Widmer, G.I. Lampronti, S. Anzellini, R. Gaillac, S. Farsang, C. Zhou, A.M. Belenger, C.W. Wilson, H. Palmer, A.K. Kleppe, M.T. Wharmby, X. Yu, S.M. Cohen, S.G. Telfer, S.A.T. Redfern, F.X. Coudert, S.G. MacLeod, T.D. Bennett, Pressure promoted low-temperature melting of metal-organic frameworks, *Nat Mater* 18(4) (2019) 370-+.
- [89] P. Davies, *The New Physics*, First ed., Cambridge University Press 1989.
- [90] A. Zangwill, A half century of density functional theory, *Phys Today* 68(7) (2015) 34-39.
- [91] E.J. Baerends, Perspective on "Self-consistent equations including exchange and correlation effects" - Kohn W, Sham LJ (1965) *Phys Rev A* 140 : 133-1138, *Theor Chem Acc* 103(3-4) (2000) 265-269.
- [92] W. Kohn, L.J. Sham, Self-Consistent Equations Including Exchange and Correlation Effects, *Physical Review* 140(4A) (1965) A1133-A1138.
- [93] J.P. Perdew, K. Schmidt, Jacob's ladder of density functional approximations for the exchange-correlation energy, *Density Functional Theory and Its Application to Materials* 577 (2001) 1-20.
- [94] A.D. Becke, A New Mixing of Hartree-Fock and Local Density-Functional Theories, *J Chem Phys* 98(2) (1993) 1372-1377.

- [95] J.P. Perdew, M. Ernzerhof, K. Burke, Rationale for mixing exact exchange with density functional approximations, *J Chem Phys* 105(22) (1996) 9982-9985.
- [96] J.P. Perdew, K. Burke, M. Ernzerhof, Generalized gradient approximation made simple, *Phys Rev Lett* 77(18) (1996) 3865-3868.
- [97] R. Car, M. Parrinello, Unified Approach for Molecular-Dynamics and Density-Functional Theory, *Phys Rev Lett* 55(22) (1985) 2471-2474.
- [98] D. Sholl, Steckel J. , *Density functional Theory: a practical approach*, Wiley 2009.
- [99] M. Parrinello, A. Rahman, Polymorphic Transitions in Single-Crystals - a New Molecular-Dynamics Method, *J Appl Phys* 52(12) (1981) 7182-7190.
- [100] J.M. Soler, E. Artacho, J.D. Gale, A. Garcia, J. Junquera, P. Ordejon, D. Sanchez-Portal, The SIESTA method for ab initio order-N materials simulation, *J Phys-Condens Mat* 14(11) (2002) 2745-2779.
- [101] N. Troullier, J.L. Martins, Efficient Pseudopotentials for Plane-Wave Calculations, *Phys Rev B* 43(3) (1991) 1993-2006.
- [102] I. Stephanov, *Modelling of Fluid Fragmentation by Molecular Dynamics*, Mater Sci Eng, University of Sheffield, 2013.
- [103] S. Le Roux, V. Petkov, ISAACS - interactive structure analysis of amorphous and crystalline systems, *J Appl Crystallogr* 43 (2010) 181-185.
- [104] N.L. Rosi, J. Eckert, M. Eddaoudi, D.T. Vodak, J. Kim, M. O'Keeffe, O.M. Yaghi, Hydrogen storage in microporous metal-organic frameworks, *Science* 300(5622) (2003) 1127-1129.
- [105] H. Li, M. Eddaoudi, M. O'Keeffe, O.M. Yaghi, Design and synthesis of an exceptionally stable and highly porous metal-organic framework, *Nature* 402(6759) (1999) 276-279.
- [106] B. Civalleri, F. Napoli, Y. Noel, C. Roetti, R. Dovesi, Ab-initio prediction of materials properties with CRYSTAL: MOF-5 as a case study, *Crystengcomm* 8(5) (2006) 364-371.
- [107] R. Warmbier, A. Quandt, G. Seifert, Dielectric Properties of Selected Metal-Organic Frameworks, *J Phys Chem C* 118(22) (2014) 11799-11805.
- [108] L.M. Yang, G.Y. Fang, J. Ma, E. Ganz, S.S. Han, Band Gap Engineering of Paradigm MOF-5, *Cryst Growth Des* 14(5) (2014) 2532-2541.
- [109] L.M. Yang, P. Vajeeston, P. Ravindran, H. Fjellvag, M. Tilset, Theoretical Investigations on the Chemical Bonding, Electronic Structure, And Optical Properties of the Metal-Organic Framework MOF-5, *Inorg Chem* 49(22) (2010) 10283-10290.
- [110] L.M. Yang, G.Y. Fang, J. Ma, R. Pushpa, E. Ganz, Halogenated MOF-5 variants show new configuration, tunable band gaps and enhanced optical response in the visible and near infrared, *Phys Chem Chem Phys* 18(47) (2016) 32319-32330.
- [111] M. Mattesini, J.M. Soler, F. Yndurain, Ab initio study of metal-organic framework-5 Zn₄O(1,4-benzenedicarboxylate)(3): An assessment of mechanical and spectroscopic properties, *Phys Rev B* 73(9) (2006).
- [112] D.F. Bahr, J.A. Reid, W.M. Mook, C.A. Bauer, R. Stumpf, A.J. Skulan, N.R. Moody, B.A. Simmons, M.M. Shindel, M.D. Allendorf, *Mechanical*

properties of cubic zinc carboxylate IRMOF-1 metal-organic framework crystals, *Phys Rev B* 76(18) (2007).

[113] K. Banlusan, E. Antillon, A. Strachan, Mechanisms of Plastic Deformation of Metal-Organic Framework-5, *J Phys Chem C* 119(46) (2015) 25845-25852.

[114] S. Bordiga, C. Lamberti, G. Ricchiardi, L. Regli, F. Bonino, A. Damin, K.P. Lillerud, M. Bjorgen, A. Zecchina, Electronic and vibrational properties of a MOF-5 metal-organic framework: ZnO quantum dot behaviour, *Chem Commun* (20) (2004) 2300-2301.

[115] N.A. Rodriguez, R. Parra, M.A. Grela, Structural characterization, optical properties and photocatalytic activity of MOF-5 and its hydrolysis products: implications on their excitation mechanism, *Rsc Adv* 5(89) (2015) 73112-73118.

[116] C.G. Silva, A. Corma, H. Garcia, Metal-organic frameworks as semiconductors, *J Mater Chem* 20(16) (2010) 3141-3156.

[117] R. Diaz, M.G. Orcajo, J.A. Botas, G. Calleja, J. Palma, Co8-MOF-5 as electrode for supercapacitors, *Mater Lett* 68 (2012) 126-128.

[118] I.A. Khan, Y.H. Qian, A. Badshah, M.A. Nadeem, D. Zhao, Highly Porous Carbon Derived from MOF-5 as a Support of ORR Electrocatalysts for Fuel Cells, *Acs Appl Mater Inter* 8(27) (2016) 17268-17275.

[119] W. Tang, E. Sanville, G. Henkelman, A grid-based Bader analysis algorithm without lattice bias, *J Phys-Condens Mat* 21(8) (2009).

[120] K. Momma, F. Izumi, VESTA 3 for three-dimensional visualization of crystal, volumetric and morphology data, *J Appl Crystallogr* 44 (2011) 1272-1276.

[121] L.H. He, F. Liu, G. Hautier, M.J.T. Oliveira, M.A.L. Marques, F.D. Vila, J.J. Rehr, G.M. Rignanese, A.H. Zhou, Accuracy of generalized gradient approximation functionals for density-functional perturbation theory calculations, *Phys Rev B* 89(6) (2014).

[122] R. Hundt, J.C. Schon, A. Hannemann, M. Jansen, Determination of symmetries and idealized cell parameters for simulated structures, *J Appl Crystallogr* 32 (1999) 413-416.

[123] T.D. Bennett, A.L. Goodwin, M.T. Dove, D.A. Keen, M.G. Tucker, E.R. Barney, A.K. Soper, E.G. Bithell, J.C. Tan, A.K. Cheetham, Structure and Properties of an Amorphous Metal-Organic Framework, *Phys Rev Lett* 104(11) (2010).

[124] J. Gascon, M.D. Hernandez-Alonso, A.R. Almeida, G.P.M. van Klink, F. Kapteijn, G. Mul, Isoreticular MOFs as Efficient Photocatalysts with Tunable Band Gap: An Operando FTIR Study of the Photoinduced Oxidation of Propylene, *Chemsuschem* 1(12) (2008) 981-983.

[125] H. Khajavi, J. Gascon, J.M. Schins, L.D.A. Siebbeles, F. Kapteijn, Unraveling the Optoelectronic and Photochemical Behavior of Zn4O-Based Metal Organic Frameworks, *J Phys Chem C* 115(25) (2011) 12487-12493.

[126] K.B. Wiberg, P.R. Rablen, Comparison of Atomic Charges Derived Via Different Procedures, *J Comput Chem* 14(12) (1993) 1504-1518.

- [127] F. De Proft, C. Van Alsenoy, A. Peeters, W. Langenaeker, P. Geerlings, Atomic charges, dipole moments, and Fukui functions using the Hirshfeld partitioning of the electron density, *J Comput Chem* 23(12) (2002) 1198-1209.
- [128] M. Wu, J.S. Tse, S.Y. Wang, C.Z. Wang, J.Z. Jiang, Origin of pressure-induced crystallization of Ce₇₅Al₂₅ metallic glass, *Nat Commun* 6 (2015).
- [129] M. Wu, H.B. Lou, J.S. Tse, H.Y. Liu, Y.M. Pan, K. Takahama, T. Matsuoka, K. Shimizu, J.H. Jiang, Pressure-induced polyamorphism in a main-group metallic glass, *Phys Rev B* 94(5) (2016).
- [130] K.S. Park, Z. Ni, A.P. Cote, J.Y. Choi, R.D. Huang, F.J. Uribe-Romo, H.K. Chae, M. O'Keeffe, O.M. Yaghi, Exceptional chemical and thermal stability of zeolitic imidazolate frameworks, *P Natl Acad Sci USA* 103(27) (2006) 10186-10191.
- [131] R. Banerjee, A. Phan, B. Wang, C. Knobler, H. Furukawa, M. O'Keeffe, O.M. Yaghi, High-throughput synthesis of zeolitic imidazolate frameworks and application to CO₂ capture, *Science* 319(5865) (2008) 939-943.
- [132] L. Mu, B. Liu, H. Liu, Y.T. Yang, C.Y. Sun, G.J. Chen, A novel method to improve the gas storage capacity of ZIF-8, *J Mater Chem* 22(24) (2012) 12246-12252.
- [133] D.K. Panchariya, R.K. Rai, E.A. Kumar, S.K. Singh, Core-Shell Zeolitic Imidazolate Frameworks for Enhanced Hydrogen Storage, *Acs Omega* 3(1) (2018) 167-175.
- [134] Y.B. Huang, Y.H. Zhang, X.X. Chen, D.S. Wu, Z.G. Yi, R. Cao, Bimetallic alloy nanocrystals encapsulated in ZIF-8 for synergistic catalysis of ethylene oxidative degradation, *Chem Commun* 50(70) (2014) 10115-10117.
- [135] A. Schejn, A. Aboulaich, L. Balan, V. Falk, J. Lalevee, G. Medjahdi, L. Aranda, K. Mozet, R. Schneider, Cu²⁺-doped zeolitic imidazolate frameworks (ZIF-8): efficient and stable catalysts for cycloadditions and condensation reactions, *Catal Sci Technol* 5(3) (2015) 1829-1839.
- [136] C.L. Whitford, C.J. Stephenson, D.A. Gomez-Gualdrón, J.T. Hupp, O.K. Farha, R.Q. Snurr, P.C. Stair, Elucidating the Nanoparticle Metal Organic Framework Interface of Pt@ZIF-8 Catalysts, *J Phys Chem C* 121(45) (2017) 25079-25091.
- [137] W.J. Ma, Q. Jiang, P. Yu, L.F. Yang, L.Q. Mao, Zeolitic Imidazolate Framework-Based Electrochemical Biosensor for in Vivo Electrochemical Measurements, *Anal Chem* 85(15) (2013) 7550-7557.
- [138] M. Erkartal, H. Usta, M. Citir, U. Sen, Proton conducting poly(vinyl alcohol) (PVA)/poly (2-acrylamido-2-methylpropane sulfonic acid) (PAMPS)/zeolitic imidazolate framework (ZIF) ternary composite membrane, *J Membrane Sci* 499 (2016) 156-163.
- [139] Y.L. Wang, P.F. Hou, Z. Wang, P. Kang, Zinc Imidazolate Metal-Organic Frameworks (ZIF-8) for Electrochemical Reduction of CO₂ to CO, *Chemphyschem* 18(22) (2017) 3142-3147.
- [140] K.S. Park, Z. Ni, A.P. Côté, J.Y. Choi, R. Huang, F.J. Uribe-Romo, H.K. Chae, M. O'Keeffe, O.M. Yaghi, Exceptional chemical and thermal stability of zeolitic imidazolate frameworks, *Proceedings of the National Academy of Sciences* 103(27) (2006) 10186-10191.

- [141] S.C. McKellar, S.A. Moggach, Structural studies of metal-organic frameworks under high pressure, *Acta Crystallogr B* 71 (2015) 587-607.
- [142] H. Tanaka, S. Ohsaki, S. Hiraide, D. Yamamoto, S. Watanabe, M.T. Miyahara, Adsorption-Induced Structural Transition of ZIF-8: A Combined Experimental and Simulation Study, *J Phys Chem C* 118(16) (2014) 8445-8454.
- [143] S. Tanaka, K. Fujita, Y. Miyake, M. Miyamoto, Y. Hasegawa, T. Makino, S. Van der Perre, J.C. Saint Remi, T. Van Assche, G.V. Baron, J.F.M. Denayer, Adsorption and Diffusion Phenomena in Crystal Size Engineered ZIF-8 MOF, *J Phys Chem C* 119(51) (2015) 28430-28439.
- [144] F.X. Coudert, Molecular Mechanism of Swing Effect in Zeolitic Imidazolate Framework ZIF-8: Continuous Deformation upon Adsorption, *Chemphyschem* 18(19) (2017) 2732-2738.
- [145] C.L. Hobday, C.H. Woodall, M.J. Lennox, M. Frost, K. Kamenev, T. Duren, C.A. Morrison, S.A. Moggach, Understanding the adsorption process in ZIF-8 using high pressure crystallography and computational modelling, *Nat Commun* 9 (2018).
- [146] J.C. Tan, B. Civalleri, C.C. Lin, L. Valenzano, R. Galvelis, P.F. Chen, T.D. Bennett, C. Mellot-Draznieks, C.M. Zicovich-Wilson, A.K. Cheetham, Exceptionally Low Shear Modulus in a Prototypical Imidazole-Based Metal-Organic Framework, *Phys Rev Lett* 108(9) (2012).
- [147] I. Peral, J. Iniguez, Amorphization induced by pressure: Results for zeolites and general implications, *Phys Rev Lett* 97(22) (2006).
- [148] J. Maul, M.R. Ryder, M.T. Ruggiero, A. Erba, Pressure-driven mechanical anisotropy and destabilization in zeolitic imidazolate frameworks, *Phys Rev B* 99(1) (2019).
- [149] P. Ravindran, L. Fast, P.A. Korzhavyi, B. Johansson, J. Wills, O. Eriksson, Density functional theory for calculation of elastic properties of orthorhombic crystals: Application to TiSi₂, *J Appl Phys* 84(9) (1998) 4891-4904.
- [150] S.Q. Wang, H.Q. Ye, Ab initio elastic constants for the lonsdaleite phases of C, Si and Ge, *J Phys-Condens Mat* 15(30) (2003) 5307-5314.
- [151] C.A. Ponce, R.A. Casali, M.A. Caravaca, Ab initio study of mechanical and thermo-acoustic properties of tough ceramics: applications to HfO₂ in its cubic and orthorhombic phase, *J Phys-Condens Mat* 20(4) (2008).
- [152] M.M. Barak, J.D. Currey, S. Weiner, R. Shahar, Are tensile and compressive Young's moduli of compact bone different?, *J Mech Behav Biomed* 2(1) (2009) 51-60.
- [153] M. Erkartal, M. Durandurdu, Pressure-Induced Amorphization of MOF-5: A First Principles Study, *Chemistryselect* 3(28) (2018) 8056-8063.
- [154] C. Zhou, L. Longley, A. Krajnc, G.J. Smales, A. Qiao, I. Erucar, C.M. Doherty, A.W. Thornton, A.J. Hill, C.W. Ashling, O.T. Qazvini, S.J. Lee, P.A. Chater, N.J. Terrill, A.J. Smith, Y.Z. Yue, G. Mali, D.A. Keen, S.G. Telfer, T.D. Bennett, Metal-organic framework glasses with permanent accessible porosity, *Nat Commun* 9 (2018).

- [155] A.W. Thornton, K.E. Jelfs, K. Konstas, C.M. Doherty, A.J. Hill, A.K. Cheetham, T.D. Bennett, Porosity in metal-organic framework glasses, *Chem Commun* 52(19) (2016) 3750-3753.
- [156] T.D. Bennett, Y.Z. Yue, P. Li, A. Qiao, H.Z. Tao, N.G. Greaves, T. Richards, G.I. Lampronti, S.A.T. Redfern, F. Blanc, O.K. Farha, J.T. Hupp, A.K. Cheetham, D.A. Keen, Melt-Quenched Glasses of Metal-Organic Frameworks, *J Am Chem Soc* 138(10) (2016) 3484-3492.
- [157] M. Gao, A.J. Misquitta, L.H.N. Rimmer, M.T. Dove, Molecular dynamics simulation study of various zeolitic imidazolate framework structures, *Dalton T* 45(10) (2016) 4289-4302.
- [158] J.C. Tan, B. Civalleri, A. Erba, E. Albanese, Quantum mechanical predictions to elucidate the anisotropic elastic properties of zeolitic imidazolate frameworks: ZIF-4 vs. ZIF-zni, *Crystengcomm* 17(2) (2015) 375-382.
- [159] S. Grimme, Semiempirical GGA-type density functional constructed with a long-range dispersion correction, *J Comput Chem* 27(15) (2006) 1787-1799.
- [160] F. Nestola, A. Artac, T. Pippinger, R. Miletich, L. Secco, S. Milani, G.J. Redhammer, First evidence of P2(1)/n to P2(1)/c structural transformation in pyroxene-type LiAlGe₂O₆ under high-pressure conditions, *J Solid State Chem* 228 (2015) 250-257.
- [161] J. Heyd, G.E. Scuseria, M. Ernzerhof, Hybrid functionals based on a screened Coulomb potential, *J Chem Phys* 118(18) (2003) 8207-8215.